ADVANCED CONTROL OF POWER CONVERTERS FOR MICROGRIDS WITH RENEWABLE ENERGY RESOURCES AND VARIABLE LOADS

SHAN YINGHAO

PhD

The Hong Kong Polytechnic University

2020

The Hong Kong Polytechnic University

Department of Electrical Engineering

Advanced Control of Power Converters for Microgrids with Renewable Energy Resources and Variable Loads

SHAN Yinghao

A thesis submitted in partial fulfillment of the
requirements for the degree of Doctor of Philosophy

March 2020

CERTIFICATE OF ORIGINALITY

I hereby declare that this thesis is my own work and that, to the best of my knowledge and belief, it reproduces no material previously published or written, nor material that has been accepted for the award of any other degree or diploma, except where due acknowledgement has been made in the text.

______________________ (Signed)

__SHAN Yinghao________ (Name of Student)

Abstract

For the last several decades, cascaded linear control (CLC) has been widely used in the field of power electronics. However, it presents several major problems. First, for the control structure, it suffers from "more loops, more complicated". Second, in order to drive the switching unit, pulse-width modulation (PWM) is necessary to be adopted, which results in a slow dynamic response. Third, proportional-integral-differential (PID) controllers are normally embedded in these CLC control loops, which results in a tedious work of repeatedly tuning the parameters and thus the implementation is restricted.

Early in this century, the concept of microgrid (MG) was proposed to meet the proliferated green energies. And now it is suggested to be one of the future dominating forms of power supply. An MG can form an independent controllable unit with an integration of renewable energy sources (RESs), storages, loads and control systems. As a key component to interface RESs into the MG, the power electronic converter needs to be well regulated for the MG. The droop control method is typically used for these converters to deal with parallel-connected RESs by proportionally sharing their powers. Traditionally, voltage and current double loops are attached to the droop control method to produce driving signals for the switching units. However, subject to the limitations of these CLC double loops, the advantages of droop function may be compromised. In addition, for existing research about MGs, ideal and steady DC power sources are usually adopted to simulate a variety of RESs. However, in practice, this is deficient and incomplete since the intermittent nature of such energy

resources is overlooked. Consequently, traditional CLC control may no longer be the best choice for MG control, and this results in the urgent requirement to develop advanced control methods to ensure a better control performance rather than using the CLC method.

In these years, model predictive control (MPC), as a distinctly different technique from CLC control, has been introduced to effectively control these converters. MPC is based on the knowledge of system topology and the prediction of system behavior. Finite control set model predictive control (FCS-MPC) is an important branch of the MPC family. For FCS-MPC, the optimal switching state of power converters is determined according to a prespecified cost function. By taking into account current system states, cost function can be solved over some future certain intervals. As reported in existing literature, compared with CLC, MPC can be utilized to achieve a better performance such as a faster dynamic response, an easier way to include nonlinear constraints and a better robustness, etc. Although MPC is advantageous, it is seldom reported about its application in the coordination control of multiple converters in MGs.

In this thesis, various power converters controlled by MPC have been investigated and developed, which involves bidirectional DC-DC buck-boost converters and AC-DC interlinking converters. They are controlled through analyzing the systemic dynamic behaviors (especially for inductors and capacitors used in the circuit). Then predictive model is built, cost function is defined, and optimization process is computed repeatedly. In this way, traditional CLC control loops have been replaced, and further, the coordinated control of these converters applied in various MG types has also been researched. Comprehensive cases related to the MG operation have also been studied such as islanded operation, grid-connected operation, islanding process, and grid synchronization. Besides, in order to address the aforementioned issues about simulating a more realistic DC power source, photovoltaic (PV) systems and/or wind turbines (WTs) as well as energy storage systems (ESSs) are combined to provide a DC common bus serving as a practical DC source. In this context, the intermittent nature of RESs influenced by natural environmental factors (like solar irradiation, ambient temperature, wind speed, etc) is considered.

For the standard operation of an MG, the hierarchical control structure with three levels is universally accepted. In the first and basic level, the well-known droop control method serves as the primary control. Since droop control method will cause frequency and voltage deviations, secondary control is necessary to be adopted. In general, centralized secondary control is often used, which works via central PI controllers making adjustment signals based on the measurements from common buses. However, this centralized way suffers from a single point of failure and the potential breakdown of the whole system. Therefore, a washout filter based method which is a distributed secondary control using only localized measurements with higher flexibility and reliability is developed here, meanwhile, the power sharing belonging to the primary control domain is also achieved.

In this thesis, a series of control schemes based on MPC principles has been developed for different MGs with various properties. Specifically, in an MG system, for DC-side control, MPC-based schemes are applied on bidirectional DC-DC converters to form a stable and robust DC bus; while for AC-side control, MPC-based schemes are applied on VSC-based interlinking converters to ensure a stable and high-quality AC voltage supply. Besides, the fluctuating power resulted from intermittent RESs has

been respected and investigated. Moreover, a system-level energy management scheme (EMS), an auxiliary voltage support functionality, and a washout filter based power sharing method with voltage compensation are also developed for various MG applications. The proposed various MPC-based schemes have been validated by Matlab/Simulink case studies and controller-hardware-in-the-loop (CHIL) tests.

Acknowledgements

I would like to thank all of those persons who helped, assisted, and inspired me throughout my PhD program at the Hong Kong Polytechnic University.

First of all, I am very thankful to my chief supervisor, Dr. Ka Wing Chan, for his generous help in providing excellent research condition and environment. Besides, Dr. Chan patiently helps me solve so many problems. His courtesy and generosity really impress me.

Also, I am indebted to my co-supervisor, Dr. Jiefeng Hu, who has influenced me most in my research since I first came here and started my research work. Besides, Dr. Hu is always very generous with his time and knowledge.

In addition, I owe special thanks to Prof. Ka Wai Cheng and Dr. Ka Chung Wong for their kind help in my teaching-assistant work.

I wish to thank all my friends and members in our lab for giving me a vigorous academic atmosphere and a collaborative research journey. I will cherish the memory forever.

I also extend my gratitude to the staff in the general office of EE department and the research office of PolyU for their patience and cooperation.

Last but not least, I am forever grateful to my parents for their unflagging support and steadfast encouragement. My gratitude also extends to my elder sister for her help and advice.

Table of Contents

Lists of Figures, Tables, Abbreviations, and Symbols

List of Figures

List of Tables

List of Abbreviations

AC	Alternating current
AFE	Active-front-end
CHIL	Controller-hardware-in-the-loop
CLC	Cascaded linear control
CSC	Current source converter
DC	Direct current
DG	Distributed generation
DSP	Digital signal processor
EMS	Energy management scheme
ESS	Energy storage system
FCS-MPC	Finite control set model predictive control
HV	High voltage
KCL	Kirchhoff's current law
KVL	Kirchhoff's voltage law
LV	Low voltage
MG	Microgrid
MGCC	MG central controller
MPC	Model predictive control
MPCPC	Model predictive current and power control
MPPC	Model predictive power control
MPPT	Maximum power point tracking
MPVC	Model predictive voltage control
MPVPC	Model predictive voltage and power control
PCC	Point of common coupling
PI	Proportional-integral
PID	Proportional-integral-differential
PLL	Phase-locked loop
PMSG	Permanent-magnet synchronous generator
PV	Photovoltaic
PWM	Pulse-width modulation
RES	Renewable energy source

ROM	The rest of the MG
SOC	State of charge
SOGI	Second-order general-integrator
STS	Static transfer switch
THD	Total harmonic distortion
UPS	Uninterruptible power supply
VSC	Voltage source converter
WT	Wind turbine

List of Symbols

ΔE	Allowable voltage magnitude deviation
Δf	Allowable frequency deviation
A	Swept area of blades
a, b	Cost function weighting factors
A_e, B_e	Exponential voltage and exponential capacity
A_m, B_m	Coefficient matrices
C_1	DC-DC input capacitance
C_2	DC-DC output capacitance
C_f	Capacitive component of the filter
C_p	The coefficient in WT control
D	Duty ratio
dv	Coefficient of washout filter
E	Voltage magnitude
E^*	Voltage magnitude reference
E_0	Constant voltage
f	Frequency
f^*	Frequency reference
f_c, E_c	Frequency and voltage compensations of secondary control
f_l	Lowpass filter cut-off frequency
f_{sw}	Switching frequency (average value for the comparison)
$G_P(s)$, $G_Q(s)$	Droop functions in the S domain
$i(t)$	Battery current
i^*	Current reference or low frequency current
I_{bat}	Battery current
I_{bat_rated}	Battery rated current
I_C	The capacitor C_2 current
I_D	Diode reverse saturation current
I_d	Discharging current of the battery
I_{DC}	The current from ESS to DC bus
I_{dc}	The current from VSC to DC bus
$\boldsymbol{I}_f$	Inductor current of the filter

I_g	Exchanging current from/to the main grid
I_{grms}	The RMS value of I_g
I_{in}	The current absorbed by the ESS
I_L	DC-DC inductor current
I_L^*	DC-DC inductor current reference
$\boldsymbol{I}_o$	Load current or output current
I_{out}	Output current
I_{ph}	One single solar cell photocurrent
I_{RES}	Output current from the RES
I_{ROM}	The current flowing to the ROM
$i_{sd,q}$	Stator current in the d-q coordinate plane
it	Extracted capacity
J	Inertia of the motor/generator
J_I	Cost function considering current
J_P	Cost function considering power
J_{PQ}	Cost function considering both active power and reactive power
J_V	Cost function considering voltage
J_{VD}	Cost function considering voltage changing trend
K	Polarization constant
k_i	Integral coefficient of PI controller
k_{if}, k_{iE}	Integral coefficients for secondary control
k_{iP}, k_{iQ}	Integral coefficients for tertiary control
k_p	Proportional coefficient of PI controller
k_{pf}, k_{pE}	Proportional coefficients for secondary control
k_{pP}, k_{pQ}	Proportional coefficients for tertiary control
L	DC-DC inductance
L_{bf}	Battery-side inductance
$L_{d,q}$	Stator inductance in the d-q coordinate plane
L_f	Inductive component of the filter
m, n	Droop coefficients
m_{Var}	The coefficient of Q in voltage support
m_W	The coefficient of P in voltage support
N	Prediction horizon
P	Active power
p	Pole-pair number

P^*	Active power reference
P_{acL}	AC load power
P_{bat}	Battery power
P_{dcL}	DC loads power
P_e	Active power across the impedance
P_{ESS}^*	The ESS power reference
P_{ESS_max}	The rated ESS power
P_g	The power exchanged with the main grid
P_L	Active power of the load
P_{loss}	Power loss
P_{max}	Allowable maximal active power
P_{net}	Net power
P_{out}^*	Output power reference
P_{PCC}	Active power from the PCC
P_{pv}	PV output power
P_{PV_mpp}	The output maximum power of the PV system
P_w	WT output power
Q	Reactive power
Q^*	Reactive power reference
Q_0	Battery capacity
Q_{0max}	Maximum battery capacity
Q_e	Reactive power across the impedance
Q_L	Reactive power of the load
Q_{max}	Allowable maximal reactive power
Q_{PCC}	Reactive power from the PCC
R	Turbine radius or resistance
R_f	Resistive component of the filter
R_s	Series resistance or stator winding resistance
R_{sh}	Shunt resistance
S_1-S_6	Switches
$S_{a,b,c}$	Switching states
T	Temperature
T_e^*	Torque reference
T_s	Sampling interval
u_a, u_b, u_c	Three-phase voltages

U_o	Outout voltage
V_{ac}	AC-bus voltage
V_{acrms}	The RMS value of V_{ac}
$\boldsymbol{V}_c$	Capacitor voltage of the LC filter
V_{dc}	DC-bus voltage
V_{dc}^*	DC-bus voltage reference
$\boldsymbol{V}_g$	The main grid voltage
V_{HV}	HV port voltage
$\boldsymbol{V}_i$	Converter voltage vector (i = 0,1,2…7)
V_{LV}	LV port voltage
V_{PCC}	The PCC voltage magnitude
$v_{sd,q}$	Stator voltage in the d-q coordinate plane
V_T	Thermal voltage
v_w	Wind speed
X	Reactance
$x(k)$	The value of variable x at k instant
$x(k+1)$	The value of variable x at k+1 instant
$\mathbf{x}$, $\mathbf{u}$	State variables
$X_{d,q}$	Variable X in the d-q coordinate plane
$X_{\alpha,\beta}$	Variable X in the α-β coordinate plane
Z	Impedance
β	Pitch angle
η	Diode ideality factor
λ	Tip-speed ratio
ρ	Air density
φ	The ratio of local electric power supply rule
ω	The frequency in radian
ω_m	Rotor rotational speed
Φ_v	Magnetic flux linkage

Chapter 1 Introduction

This chapter gives a brief review of the microgrids (MGs) and their general control methods, including cascaded linear control (CLC) methods, model predictive control (MPC) methods, and the control methods for parallel operation of distributed generations (DGs). Besides, their advantages and disadvantages are respectively discussed. Next, the hierarchical control architecture of MGs is introduced. Finally, the major contributions and features of this thesis are summarized.

1.1 MGs

Nowadays, environmental protection has been a serious and continuing issue for most countries in the world. In order to reduce the carbon footprint and deal with the greenhouse effect, more and more renewable energy resources (RESs) have been developed and installed[1,2]. RESs are mainly based on natural energies, such as solar, wind, geothermal, ocean, and biomass resources[3,4]. Early in this century, the concept of MGs has been proposed to address the numerous problems brought by the large-scale integration of RESs[5-7]. The DG system utilizes one type of RESs or energy storage systems (ESSs) to generate electricity, serving as an individual power supply. Among them, photovoltaic (PV) and wind turbine (WT) systems are the most usual DG types. When these multiple DGs are connected locally to form a cluster, and necessary power electronic devices are equipped for the power control and measurement, as well as various loads are supplied, a general MG is established. An MG can be distinguished as alternating current (AC), direct current (DC) or hybrid (both having AC and DC) MG in correspondence with the voltage type of its internal common bus[8,9].

Fig.1-1 depicts a typical structure of the MG. It can be seen that, here, the DGs are PV, WT, and ESS systems; the loads are divided into critical and non-critical forms. The ESS is often set up to store the surplus power from the PV or WT, meanwhile to release the power for the loads when the PV and WT are powerless, thus playing a peak-load shifting role in the system. Due to the effect of various power converters (including DC-DC, DC-AC and AC-DC), a common bus can be provided and maintained by the converter-interfaced DGs[10]. The common bus also can be called the point of common coupling (PCC). The loads can be supplied by the common bus. Critical loads are powered with a higher priority than non-critical loads. In addition, non-critical loads can be shed according to the command sent from the MG central controller (MGCC) in the case of electricity shortage or routine maintenance. The MGCC has an essential role for an automatic and satisfactory operation of MGs to coordinate, protect and stabilize DGs, loads and the main grid.

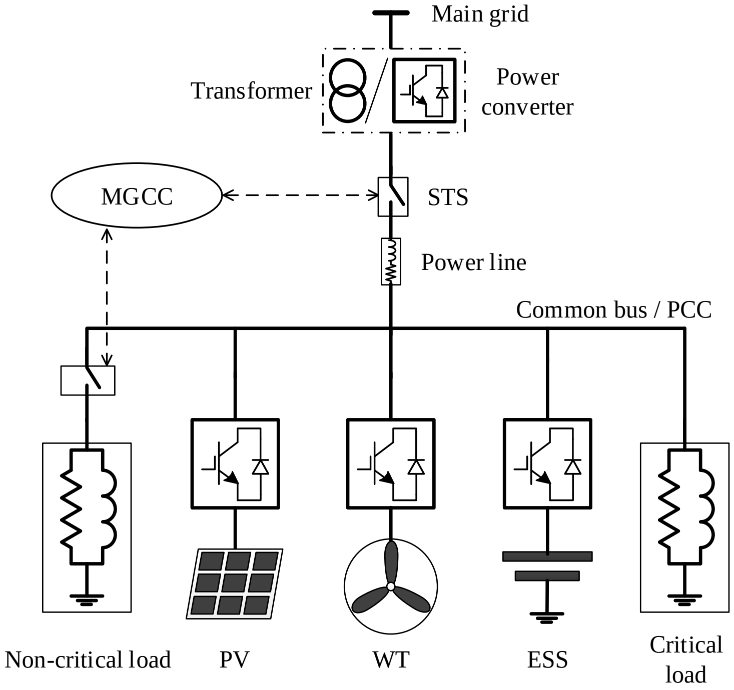

Fig.1-1 A typical structure of MGs

In these years, the MG control tends to be in a decentralized manner, which is usually based on multi-agent techniques. This can be regarded as the functionality of the MPCC is dispersed to various discrete agents. If these agents want to realize a centralized effect like the MPCC, a cooperative mechanism of them is needed[11,12].

In the steady state, a typical MG generally has two operation modes, i.e. islanded mode and grid-connected mode. The operation modes will change with the states of the static transfer switch (STS) which locates between the MG system and the main grid. The MGCC makes the decision of STS states according to either a regular schedule or a sudden event. When the STS opens, the MG works in the islanded mode; while the STS closes, the MG turns in the grid-connected mode. In islanded mode, the MGCC can decide whether to detach or reattach the non-critical load, thus to guarantee a continuous supply to the critical load. Once the STS is closed, the MG exchanges power with the main grid through the power converters, such as a transformer for an AC common bus or an AC-DC interlinking converter for a DC common bus.

In recent years, more and more MGs have been built in the world due to the outstanding benefits of constructing MGs[13,14], such as:

1) The MG can be built in a remote area where the connection to the main grid is too expensive or too time-consuming;

2) Local energies can be fully explored to produce not only electricity, but also heat, steam, cold, etc;

3) The system reliability is increased especially for the critical loads (e.g. communication facilities and emergency rescue devices) under extreme circumstances (e.g. earthquake, tsunami, and hurricane);

4) The penetration of clean, green and renewable energies is increased and a friendly integrated utility for the main grid can be formed.

Except for those benefits, however, the configuration of MGs has the following challenges:

1) As the basic elements of MGs, the RESs are strongly associated with the natural environment, so the produced power generation will be random and uncertain, which results in a challenging power regulation inside the MG;

2) It is a continuous work to make the MGCC more intelligent to better decide when and how the MG should take to provide a stable and robust system;

3) It is still an issue of how to maintain a high-quality transient performance of MGs when their operation mode changes;

4) The presence of various power electronic devices makes the MG system complicated, which brings about the problems of cooperation, control and stability.

Taking into account the above benefits and challenges, it is so important to develop advanced control schemes for MGs, at the same time, effectively maximizing the benefits and addressing the challenges.

1.2 CLC Methods

For the last decades, in the field of power electronics, the CLC methods have been widely adopted for various types of control (like the voltage, current, power, frequency, etc)[15-17]. This is owing to the fact that, as one of the most representative features, the CLC does not need the exact model of the control target.

The schematic of the common CLC structure is presented in Fig.1-2, which is often used to produce signals to drive converters[18]. It is shown that there are two small loops inside the large CLC loop[19,20]. The two small loops consist of an inner current loop that generates the voltage reference V_{ref} for the pulse-width modulation (PWM) modulator and an outer voltage loop that not only tracks the given voltage reference V^* but also provides the current reference I^* for the inner current loop.

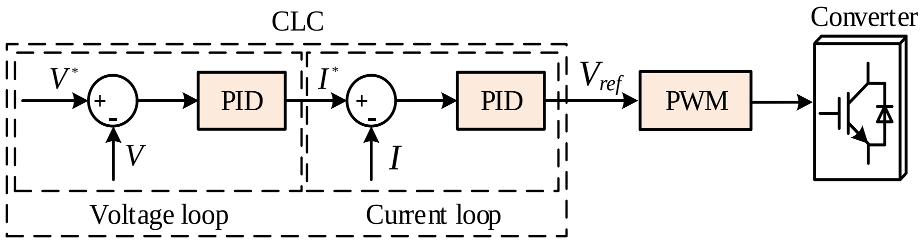

Fig.1-2 Schematic of the common CLC control

Although the CLC technique has been widely used to control power converters, it has some major drawbacks[21-23], like:

1) Proportional-integral-differential (PID) modules are generally adopted for CLC control. However, in order to achieve a satisfactory control performance, the tuning procedure of PID parameters is needed, which is based on extensive trial-and-error tests, leading to a time-consuming and difficult implementation;

2) The control architecture becomes complicated when using multiple feedback loops. Besides, in order to produce PWM signals, the combination of those feedback loops and the additional PWM generator results in a slow dynamic response of the system;

3) In a real MG system that contains diverse RESs with unavoidable fluctuant power generations, if there are no rapid and active control reactions, the system oscillation is largely to be made. In this sense, traditional CLC methods with a slow dynamic response may no longer be competent to meet the new requirements.

Regarding the CLC methods applied to the MGs, many studies that attempt to improve system performance have been conducted in these years. Such as, just to list a few of them, by introducing power derivative-integral terms into the traditional droop control, a faster transient response of power sharing was achieved in [24]. Reactive power sharing performance of nonlinear loads was improved by using adaptive virtual impedance in [25]. A modified angle droop control was described in [26] to remove the dependence of real power sharing on the output inductance with lower but stable droop coefficients. As reported in [27], an enhanced proportional power sharing method based on adaptive virtual impedance was presented to prevent the power coupling in MG control. The voltage-shifting and load current feedforward control methods were proposed in [28] to eliminate the voltage deviation due to the droop control and improve voltage control dynamics. A new droop control method based on the TS fuzzy and sliding modes was proposed in [29] to improve the current sharing performance and the robustness against the network delays. A novel consensus-based cooperative droop control was introduced in [30] to adaptively adjust the droop coefficients to improve the reactive power sharing accuracy. A control scheme that involves the islanded, grid-connected and transient controls was proposed in [31] to eliminate the steady-state voltage bias in islanded mode, and to restrain the harmonic current injected to the main grid in grid-connected mode, as well as to achieve a smooth mode transfer during transients.

1.3 MPC Methods

The MPC originated in around the 1970s, and since then it has drawn more and more attention[32,33]. The first introduction of MPC into the control of power converters appeared in the 1980s[34]. As an entirely different control structure and principle, MPC is based on the knowledge of the system topology and the prediction of the system behavior. MPC itself is not strictly limited to one specific control method[35]. In contrast, generally speaking, those control methods that involve the model of a process or a system with the predictive action can all be described as the MPC.

In the MPC control family, finite control set model predictive control (FCS-MPC) is an important branch, which uses the discrete-time properties of the control objectives[36-38]. In recent years, FCS-MPC has been extensively applied to the field of power converter control. For an FCS-MPC controlled converter, the predictive model is built based on the system states and the converter switching states, then the optimal switching state is determined according to a prespecified cost function. Commonly, the cost function involves the process to find out the minimum solutions based on the difference between the predicted values and their expected references. The cost function can be solved over some future intervals. Generally, the schematic of the FCS-MPC applied to converters can be described as shown in Fig.1-3[39-41].

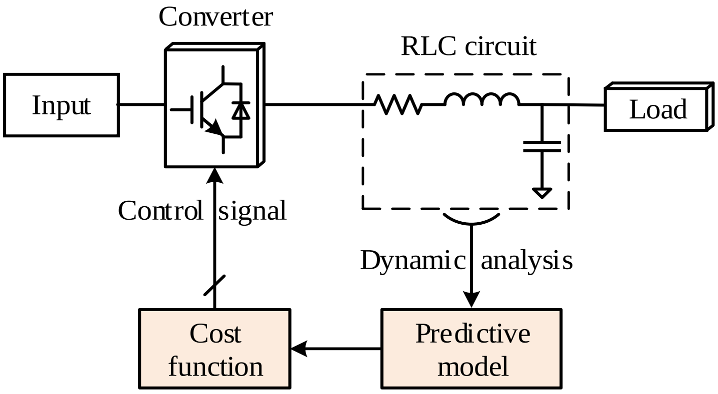

Fig.1-3 Schematic of the FCS-MPC applied to converters

It can be seen that predictive model and cost function are the two important ingredients for FCS-MPC controlled converters. Predictive model is built based on the dynamic analysis of the RLC circuit, then through a discretization process that facilitates the implementation in processors, the future variables can be obtained by computing state formulas at current time. Cost function, as an evaluation criterion or an expected control effect, is where the optimization problem is repeatedly and periodically solved, resulting in the selected control signals produced and then sent to the switching devices of converters. In addition, the multiple objectives can be included in the cost function[37,42].

Owing to the control principle and structure of the MPC, the following attractive characteristics can be summarized:

1) As a control objective, the cost function of MPC can be designed in a very explicit and intuitive way;

2) Multiple constraints that are derived either from the control demand or the object-oriented limitation can be easily involved;

3) Dynamic performance is good and the controlled system is robust;

4) For MPC used in power converters, control signals can be directly produced from the controller, eliminating the additional signal modulator.

In many regards, although MPC has so many advantages over the CLC, it has these major disadvantages:

1) MPC depends on the predictive model of the target system to perform predictive control, but sometimes the predictive model is hard to develop and the accuracy is hard to guarantee;

2) Since there involves both mathematical modeling and online solution running in the processor, sometimes the computational burden is heavy and cannot be underestimated in practice;

3) For FCS-MPC, sometimes the switching frequency is not fixed and keeps changing, which makes the filter parameter difficult to design.

1.4 Parallel Operation of DGs

The cooperative operation of parallel DGs in an MG system is a common phenomenon, as shown in Fig.1-1. Without access to the main grid and loss of the support from the main grid, islanded operation of the MG system is considered to be a primary and key step for the successful MG construction. Thus, a variety of MG control methods has been developed aiming to realize an active control of the MGs[43-45]. Among them, in general, centralized method and decentralized method are two main categories. Typically, to be specific, master-slave control as one of the centralized methods and droop control as one of the decentralized methods are compared here[12,46].

Since master-slave control has a central processor to access all DGs' data, it is good at planning or scheduling in a systemic manner, so it has a strong controllability and observability[47]. However, it also suffers from the following several drawbacks:

1) A single point of failure or the whole breakdown of the system will be caused once the central processor shuts down;

2) Its scalability is low; It is hard to expand the system without affecting existing operating DGs;

3) Since most of the commands are issued via the central processor, so the communication requirement and computational cost will be high.

By contrast, the droop control method characterized by distributed or wireless properties has the following advantages over centralized master-slave control:

1) It has simple architectures, no or few interactive communication links are necessary between DGs;

2) It is highly reliable. The parallel system can normally work even when one or more DGs have been broken down or disconnected during a large disturbance or system failure;

3) It has a high extensibility, more DGs can be switched in without the necessity of interrupting or halting any existing operating DGs.

Furthermore, in most existing references about the parallel operation of DGs, in order to mimic the various RESs, especially for those interfaced with DC power sources like PV systems, an ideal DC power source is mostly used[24,48]. Although this mimicry can expedite the design cycle, when it comes to the practical situation, it becomes defective and incomplete because the intermittent nature of the RESs is overlooked. In this thesis, a real DC power source formed by RESs and ESSs is built for a more precise DC-side simulation and to provide a solid foundation for the control design on the AC side.

1.5 Hierarchical Control

Nominally, hierarchical control or multilayer control is a common and effective way to govern a complex system, this is also true for the MGs that have multiple parallel converter-interfaced DGs, different bus types and diverse operation modes. Typically, a three-level control structure including primary, secondary, and tertiary control is utilized for MGs[5,49,50]. These three levels are separated by different transmission rates where the upper control level has a slower transmission speed, as depicted in Fig.1-4.

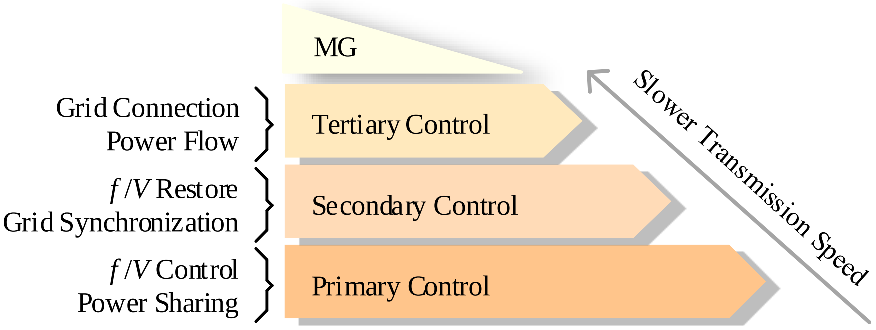

Fig.1-4 Hierarchical control structure of MGs

Primary control, as the name suggests, is the underlying level that stabilizes the whole system within the acceptable frequency f and voltage V ranges, while at the same time, shares systemic loads with the fastest response. Under the circumstances that the droop control method is used in the primary control, secondary control which compensates the frequency/voltage deviations caused by the primary control becomes a necessity. In the steady state, secondary control can restore the deviated frequency/voltage to their rated values and perform the grid synchronization. In a general way, secondary control can be divided into two categories: centralized way and decentralized way. Upon the MG meets the synchronization requirement, it can connect to the main grid and tertiary control appears. Tertiary control focuses on regulating the power flow between the MG and the main grid. Moreover, associated economic optimization and cost estimation, as well as power planning are all included in the tertiary control regime.

So far, many studies have been conducted for the hierarchical control of MGs.

For primary control, a droop modification was made to use adaptive virtual output impedance to achieve effective reactive power sharing in [51]. The virtual impedance was implemented in [52] by a second-order general-integrator (SOGI) to reduce the sensitivity to the output current noise, to achieve a better output-voltage total harmonic distortion (THD), and to enhance the sharing of nonlinear loads. A new flux droop method was developed in [53] to achieve accurate active and reactive power sharing with a reduced frequency deviation than the traditional voltage droop method. A wireless reactive power sharing method using feeder current sensing and adaptive virtual impedance control was proposed in [54] to improve the reactive power sharing accuracy. An adaptive droop control method was proposed in [55] where the droop coefficients are adjusted by calculating the MG impedance thus to achieve a power sharing with reduced power losses based on local measurements. In [56], the cross circulating current and zero-sequence circulating current were considered and added to the traditional droop plus virtual impedance control to suppress both cross and zero-sequence circulating currents. The f-P/Q droop control was proposed in [57] to autonomously achieve the power balance under both resistive-inductive and resistive-capacitive loads. For low-voltage resistive MGs, a V-I droop method was adopted in [58] to alleviate traditional droop control shortcomings for the primary control. A novel voltage stabilization and power sharing method based on the virtual complex impedance was studied in [59] to improve the voltage quality and achieve accurate power sharing without the impact of hardware parameters variations.

For secondary control, a central secondary control was designed in [60] to compensate the voltage unbalance at the PCC by sending proper control signals to the local controllers in DGs. A secondary distributed cooperative voltage control based on only its own and some neighbors' information was developed in [61] to improve the system reliability. A distributed secondary control was proposed not only to restore frequency and voltage but also to ensure reactive power sharing in [62]. A new cooperative distributed secondary controller was designed in [63], only using localized and nearest-neighbor communication without the knowledge of the MG topology, impedances, or loads. In [64], a dynamic load equalization secondary control method was adopted to converge droop coefficients within reasonable values in DC MGs. A secondary controller was used to realize the THD compensation of sensitive load buses and to make DGs distribute their compensating efforts based on their rated capacity in [65]. A distributed secondary control method was proposed in [66] based on the integral output values shared by the CAN buses, thus to achieve a better dynamic power sharing performance.

While for tertiary control, an optimization method was implemented in [67] to adjust the DG compensating efforts based on the voltage unbalance limits of local buses and DG terminals. A scenario-based two-stage stochastic programming model was presented in [68] as the tertiary control taking into account some RES uncertainties and uncertain energy deviation prices. A distributed two-level tertiary control was proposed in [69] to adjust the voltage setpoints and to balance the loading among all sources, thus avoiding the single point of failure. An interior-point optimization based tertiary control was developed in [70] to coordinate the voltage source converter (VSC) and the energy hub to minimize the voltage deviations by generating desired references. A tertiary control using the receding horizon method was presented in [71] to provide the optimal power schedule based on the economic and environmental criteria.

In these years, some system-level MPC methods have been used in the MG hierarchical control, which is mostly reported in the secondary and tertiary control levels.

For the secondary control, in [72], the secondary frequency restoration was realized by using the MPC method, it was proved that the MPC had a better robustness than the traditional PI-based method. A distributed MPC-based secondary control for both frequency and voltage was developed in [73], only local and neighboring information were required, results showed that the MPC was more robust to disturbances. Using MPC to regulate the frequency of multiple MGs was presented in [74], it was shown that the MPC was better at addressing various disturbances and communication delays than the traditional PI method.

For the tertiary control, MPC was utilized for the power flow optimization in a grid-connected MG in [75], various factors were considered like electricity prices, fuel consumption cost and generator start-up cost, etc. A distributed MPC for MG power management involving economic models and pollution models was built in [76]. A distributed MPC was developed in [77] to achieve an economic optimization by taking into account the costs/benefits of energy sources, power imbalances, power exchanges, and batteries. A distributed MPC was proposed in [78] to maximize the economic benefit of MGs and minimize the degradation of storage systems under various constraints. MPC was used to minimize the total cost and to maintain the supply-demand balance under various uncertainties in [79]. In [80], a two-layer distributed MPC scheme was presented for an islanded DC MG, specifically, the upper MPC coordinates parallel converters while the lower MPC controls wind generators. A new convex MPC was proposed in [81] for an AC islanded MG to control power flows between ESSs, allowing power line losses, voltage constraints, and converter current constraints to be solved.

1.6 Thesis Main Contributions and Features

This thesis aims to fill the aforementioned gaps and address the aforementioned issues that exist in the current MG system control. The major contributions and features of this thesis are summarized as follows:

1) In existing research and industrial communities, apart from those system-level MPC methods used to optimize MG systemic cost or benefit, device-level MPC methods are infrequent to be reported in the coordinated control over various power converters in MGs. While in this thesis, multiple-DG-based MGs have been investigated, where various power converters are regulated by MPC strategies instead of traditional CLC methods and thus the whole MG can be controlled even without any PID controllers. In addition, improved overall system performance has been summarized and compared.

2) Currently, in most existing literature, various RESs especially those including DC power sources like PV systems are regularly simulated as an ideal DC power source. To some extent, although this assumption can facilitate the design process, when applied in practice, it becomes disadvantageous and incomplete to formulate the intermittent nature of RESs. In this thesis, a practical DC power source formed by the combination of RES and ESS is built for a more precise DC power simulation and to provide a solid support for the design of MPC methods. Besides, in order to simulate a

real character of RES (PV and/or WT system) and to better test the proposed control scheme, a real-world RES generation dataset including solar irradiation, ambient temperature, and/or wind speed, attached with a maximum power point tracking (MPPT) algorithm are utilized.

3) A series of MPC control schemes has been developed for multiple converters under various circumstances:

In a PV-WT-ESS MG, a model predictive current and power control (MPCPC) scheme is proposed for the bidirectional DC-DC converter equipped with ESS in the MG DC side. Using this MPCPC, the fluctuant output power from the RES has been strongly smoothed, maintaining a stable and robust DC-bus voltage supply. A model predictive voltage and power control (MPVPC) scheme for the AC-DC interlinking converter is proposed for ensuring a stable AC voltage supply and an appropriate power flow between the MG and the main grid.

In a grid-connected PV-ESS MG, a model predictive power control (MPPC) scheme for both DC-DC converter and AC-DC interlinking converter is proposed, by this, a voltage support capability can be provided for the main grid.

In a PV-ESS MG, an MPPC scheme for the DC-DC converter and a model predictive voltage control (MPVC) scheme considering the voltage changing trend for the inverter are proposed, through them, the output AC voltage is remarkably improved.

4) As for a hybrid MG with both DC and AC buses, a system-level energy management scheme (EMS) is a necessity to manage the whole giant complex system. In this thesis, an EMS is developed taking into account fluctuant power generation from RESs, battery state of charge (SOC) of ESSs, variable load demands, and electricity market price to ensure a balanced and reliable operation under various operation modes.

5) In a hierarchical structure, the droop control method is incorporated with the MPC method to serve as the primary control to share the power proportionally and accurately. A washout filter that combines primary and secondary control properties is adopted for achieving proper power sharing while restoring deviations caused by the primary control. The washout filter also compensates the voltage deviations and enables plug-and-play capability, which is investigated with the MPVC scheme in the MG system.

1.7 Thesis Outline

The outline of the rest of the thesis is as follows: Chapter 2 presents MPC-controlled power converters and hierarchical control of MGs. Chapter 3 investigates the MPC for PV-WT-ESS MGs. Chapter 4 describes the MPC for PV-ESS MGs with voltage support capability. Chapter 5 introduces the MPC for PV-ESS MGs with secondary restoration capability and improved voltage supply. Finally, the concluding remarks and future work of the thesis are given in Chapter 6.

1.8 List of Publications

Journal Papers:

1) **Y. Shan**, J. Hu and J. M. Guerrero, "A Model Predictive Power Control Method for PV and Energy Storage Systems with Voltage Support Capability," **IEEE Transactions on Smart Grid**. Published, vol. 11, no. 2, pp. 1018-1029, Mar. 2020, *doi: 10.1109/TSG.2019.2929751*
2) **Y. Shan**, J. Hu, M. Liu, J. Zhu and J. M. Guerrero, "Model Predictive Voltage and Power Control of Islanded PV-Battery Microgrids with Washout Filter Based Power Sharing Strategy,"

IEEE Transactions on Power Electronics. Published, vol. 35, no. 2, pp. 1227-1238, Feb. 2020, *doi: 10.1109/TPEL.2019.2930182*

3) **Y. Shan**, J. Hu, Z. Li and J. M. Guerrero, "A Model Predictive Control for Renewable Energy Based AC Microgrids Without Any PID Regulators," **IEEE Transactions on Power Electronics**, Published, vol. 33, no. 11, pp. 9122-9126, Nov. 2018. *doi: 10.1109/TPEL.2018.2822314*
4) **Y. Shan**, J. Hu, K. W. Chan, Q. Fu and J. M. Guerrero, "Model Predictive Control of Bidirectional DC-DC Converters and AC/DC Interlinking Converters – A New Control Method for PV-Wind-Battery Microgrids," **IEEE Transactions on Sustainable Energy**. Published, vol. 10, no. 4, pp. 1823-1833, Oct. 2019. *doi: 10.1109/TSTE.2018.2873390*
5) J. Hu, **Y. Shan**, Y. Xu and J. M. Guerrero. "A Coordinated Control of Hybrid AC/DC Microgrids with PV-Wind-Battery under Variable Generation and Load Conditions," **International Journal of Electrical Power & Energy Systems**, Published, vol. 104, pp. 583-592, Jan. 2019. *doi.org/10.1016/j.ijepes.2018.07.037*
6) J. Hu, **Y. Shan**, J. M. Guerrero, A. Ioinovici, K. W. Chan and J. Rodriguez. "Model Predictive Control of Microgrids – An Overview," submitted to **Renewable and Sustainable Energy Reviews**, Mar. 2020, under review
7) **Y. Shan**, K. W. Chan and J. Hu. "A Unified Model Predictive Voltage and Current Control for Microgrids with Distributed Fuzzy Cooperative Secondary Control," submitted to **IEEE Transactions on Industrial Informatics**, Jul. 2020, under review

Conference Papers:

1) **Y. Shan**, J. Hu, K. W. Cheng and M. Liu, "A Universal Model

Predictive Control for Practical AC Microgrids with PVs and Battery Energy Storage Systems,” **2018 IEEE Energy Conversion Congress and Exposition (ECCE)**, Published, Portland, OR, 2018, pp. 6257-6262. *doi: 10.1109/ECCE.2018.8557588*

2) **Y. Shan**, J. Hu and K. W. Chan, “Power Sharing and V/f Restoration of Standalone AC Microgrids Using Model Predictive Control,” **The 11th IET International Conference on Advances in Power System Control, Operation and Management (APSCOM 2018)**, Published, Hong Kong, 2018, 5 pp. *doi: 10.1049/cp.2018.1763*

Chapter 2 MPC-controlled Power Converters and Hierarchical Control of MGs

Bidirectional DC-DC converter and AC-DC interlinking converter are pivotal elements for the power conversion in MG systems. In this chapter, using common MPC methods to control bidirectional DC-DC converters is firstly illustrated. Then, MPC-controlled AC-DC interlinking converter is described. In addition, the configuration and modeling of various DGs (PV, WT, and ESS systems) used in this thesis are described. Lastly, in order to address the control issues of the parallel operation of DGs, the hierarchical control of MGs is presented.

2.1 MPC-controlled Bidirectional DC-DC Converter

2.1.1 Topology and Working Principle

In MGs, the ESS system is often connected to RES systems to form a balanced power unit. For example, in a PV-ESS system, if PV output power exceeds the load demand, the surplus power can be stored in the ESS to minimize the power loss; otherwise, the ESS can release the stored energy to feed the deficit load demand that PV cannot solely meet. In this case, a bidirectional power flow must be ensured between the ESS and the PV, since DC is their port type, the bidirectional DC-DC converter which can work in boost mode or buck mode to charge or discharge the battery becomes a necessity.

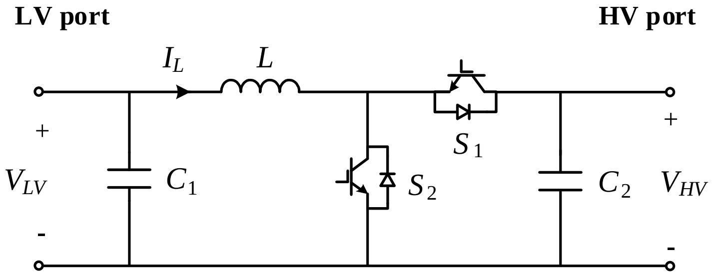

Fig.2-1 Schematic of the bidirectional DC-DC converter

Fig.2-1 draws the bidirectional DC-DC converter schematic where two ports, namely low voltage (LV) port and high voltage (HV) port, are indicated. Let us assume LV port connects the battery while HV port connects the DC bus which also links the PV output terminals. LV port has a parallel capacitor C_1, while HV port has a parallel capacitor C_2.

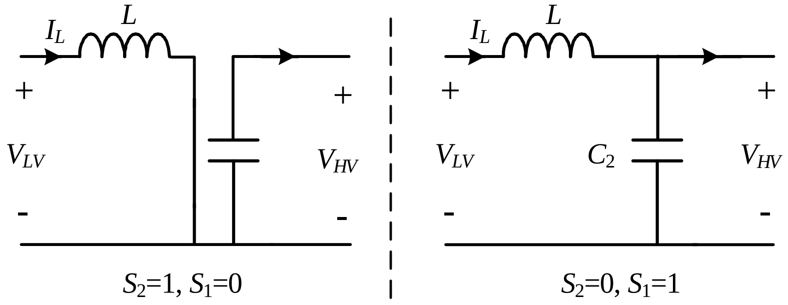

(a) Boost mode

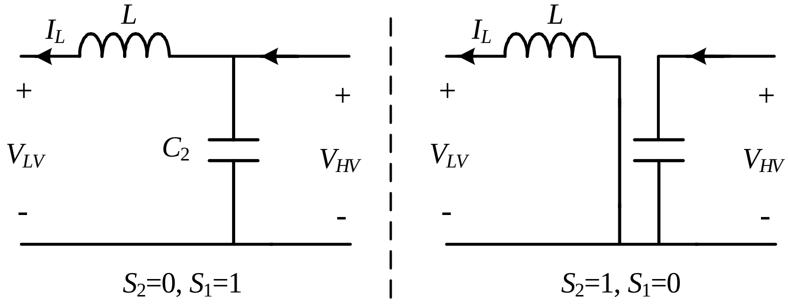

(b) Buck mode

Fig.2-2 Different working modes

The capacitors are used to stabilize and support the port voltage. The inductor L is used to smooth out the current distortions, providing a steady current flow. The switches S_1 and S_2 are the key components (usually semiconductor switches) for the power conversion, which are driven complementarily with a short dead-time compensation in a practical implementation.

Since a bidirectional power flow is enabled, Fig.2-2 shows the two different working modes: (a) the boost mode from LV to HV, (b) the buck mode from HV to LV. These two modes are changed according to the switches S_1 and S_2 ON/OFF states (1 denotes ON, 0 denotes OFF). The detailed current flow for each mode is also elaborated in Fig.2-2 (a) and (b).

2.1.2 MPC under Islanded Mode

MPC can be applied to the bidirectional DC-DC converter. As aforementioned, predictive model and cost function are the two important parts of MPC methods. In order to build the predictive model, Kirchhoff's voltage law (KVL) is used and the analysis of the working modes in Fig.2-2 is conducted. Here, the flowing direction of the current under boost mode is defined as positive.

It should be noted that the models are built under continuous current mode. However, the switching actions may be different when the system works under discontinuous current mode, and this can be another issue related to the MPC switching states optimization. Here, since we would like to compare with the basic PID-based CLC method, the fundamental continuous current mode cases of MPC are also focused.

In boost mode, the circuit model is expressed as

$$\begin{cases} S_2 = 1, S_1 = 0: \ L\dfrac{dI_L}{dt} = V_{LV} \\ S_2 = 0, S_1 = 1: \ L\dfrac{dI_L}{dt} = V_{LV} - V_{HV} \end{cases} \tag{2-1}$$

While in buck mode, it is expressed as

$$\begin{cases} S_2 = 1, S_1 = 0: \ L\dfrac{dI_L}{dt} = -V_{LV} \\ S_2 = 0, S_1 = 1: \ L\dfrac{dI_L}{dt} = V_{HV} - V_{LV} \end{cases} \tag{2-2}$$

Taking into account the current flowing direction, i.e. I_L in boost mode is the positive I_L, while I_L in buck mode is the negative I_L, (2-1) and (2-2) will be equivalent.

Euler's forward difference method is often used for the discretization of the MPC[82], which is

$$\frac{dx}{dt} = \frac{x(k+1) - x(k)}{T_s} \tag{2-3}$$

where $x(k+1)$ and $x(k)$ mean the value of x at $k+1$ instant and k instant, respectively. T_s is the sampling interval.

According to (2-3), the circuit model of (2-1) can be discretized as

$$\begin{cases} S_2 = 1, S_1 = 0: \ I_L(k+1) = \dfrac{T_s}{L}V_{LV}(k) + I_L(k) \\ S_2 = 0, S_1 = 1: \ I_L(k+1) = \dfrac{T_s}{L}(V_{LV}(k) - V_{HV}(k)) + I_L(k) \end{cases} \tag{2-4}$$

Thus, as shown in (2-4), the predictive model of the bidirectional DC-DC converter is obtained.

The next step is to design the cost function for the MPC method, however, this design will vary with different working modes. Here, the MPC for islanded mode is first designed, while the MPC for grid-connected mode will be given in the next subsection.

In islanded mode, since there is no strong support from the main grid, the primary task of an RES-ESS system will be sharing the internal power flow accurately and evenly. Therefore, the consideration of the power balance can be included for the cost function design.

Here, the two-side input/output powers and their power balance are expressed as

$$\begin{aligned} J_P &= (P_{bat} - P_{out}^*)^2 \\ &= (V_{LV} * I_L(k+1) - V_{HV} * I_{out})^2 \end{aligned} \tag{2-5}$$

where I_{out} is the output current flowing to the HV port as shown in Fig.2-3. Neglecting the switch losses, this cost function aims to keep an equilibrium power internally.

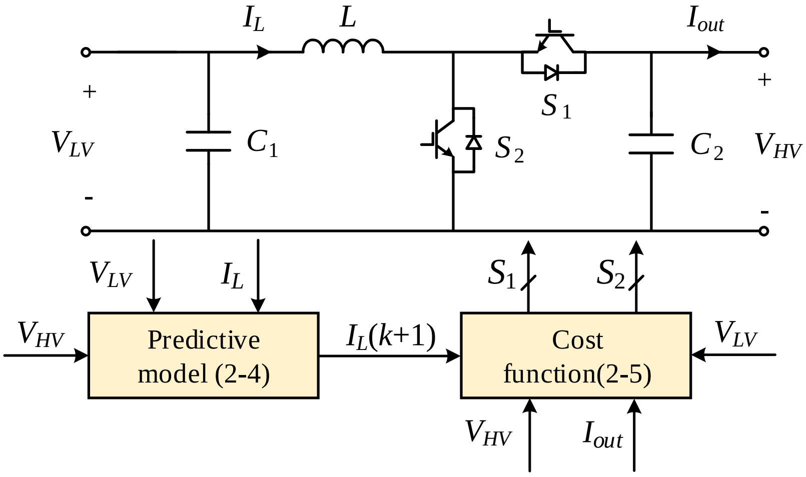

Fig.2-3 Control diagram of the MPC for bidirectional DC-DC converter under islanded mode

In Fig.2-3, the control diagram of the MPC for bidirectional DC-DC converter under islanded mode is plotted, where predictive model and cost function are clarified. By using (2-4), the predicted I_L at the next k+1 instant $I_L(k+1)$ is obtained, then it is sent to (2-5) for the predictive power calculation and the cost function minimization. This process runs on the basis of the variables measured at each sampling time, once the minimal result of (2-5) is available, its corresponding switch state will be produced and delivered to the switches S_1 and S_2 to realize the power conversion.

2.1.3 MPC under Grid-connected Mode

In a grid-connected MG, the DC bus can be maintained by the rectifier with the support from the main grid, under this circumstance, the battery does not normally focus on the dc bus control, conversely it can be directly managed by setting the flowing direction and quantity of the battery current. With this procedure, the cost function for a bidirectional DC-DC converter can be designed as

$$J_I = (I_L^* - I_L(k+1))^2 \tag{2-6}$$

where the superscript * indicates the reference which is assumed to be constant at two consecutive instants e.g. k and k+1 instants. The reference I_L^* can be given as a constant number, whether positive or negative, and it is presumed to be identical to the output current from the battery when the system is in a steady state.

The control diagram of the MPC for bidirectional DC-DC converter under grid-connected mode is depicted in Fig.2-4. As aforementioned, the charging or discharging current of the battery can be adjusted by adjusting the current reference I_L^*. That is, assume that the I_L in Fig.2-4 is positive, then when I_L^* is also set to positive values, which means the battery will be discharged with the current value of $\left|I_L^*\right|$, on the contrary, when I_L^* is set to negative values, the battery will be charged with the current value of $\left|I_L^*\right|$.

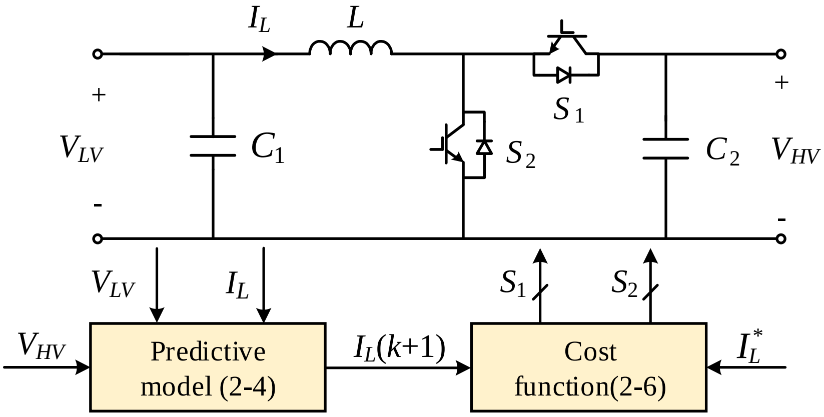

Fig.2-4 Control diagram of the MPC for bidirectional DC-DC converter under grid-connected mode

Similar to the process described in Fig.2-3, in Fig.2-4, when the current reference I_L^* is given and predicted $I_L(k+1)$ is available, the cost function (2-6) will be solved to generate the smallest solution, then relevant switch control signals are sent to derive the switches S_1 and S_2 to form one power conversion process.

2.2 MPC-controlled AC-DC Interlinking Converter

2.2.1 Topology and Working Principle

In hybrid MGs where exist both AC and DC buses, the AC-DC interlinking converter acts as a bidirectional gateway between the two buses. This means AC-DC interlinking converter plays as an inverter when the power flows from DC to AC, while as a rectifier when the power reversely flows from AC to DC. Generally, a two-level three-phase VSC as shown in Fig.2-5 can do this interlinking job. It can be seen that the VSC has two sides, the left-hand side is the DC voltage while the right-hand side is the AC voltage. The power flow can be in a two-way direction, presenting an interlinking property. There are six switches numbered from S_1 to S_6 to form the AC-side three phases, upper and lower switches in one phase cannot conduct simultaneously thus to avoid the short circuit.

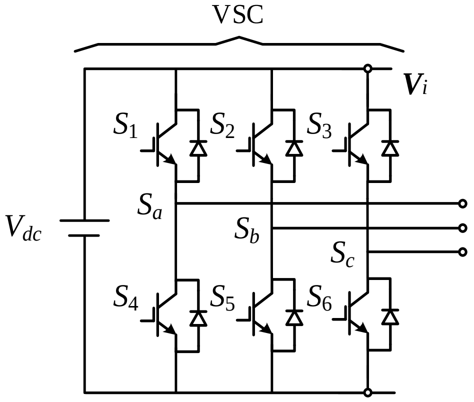

Fig.2-5 Circuit of the two-level three-phase VSC

There is a total of eight voltage vectors for a VSC, except two zero vectors other six vectors are equally distributed in the *α*-*β* coordinate, as shown in Fig.2-6. These vectors have their values represented in a complex form as

$$\boldsymbol{V}_i = \begin{cases} \frac{2}{3} V_{dc}^* e^{j(i-1)\frac{\pi}{3}} & (i=1,2,\cdots,6) \\ 0 & (i=0,7) \end{cases} \tag{2-7}$$

where V_{dc}^* is the DC-side voltage reference.

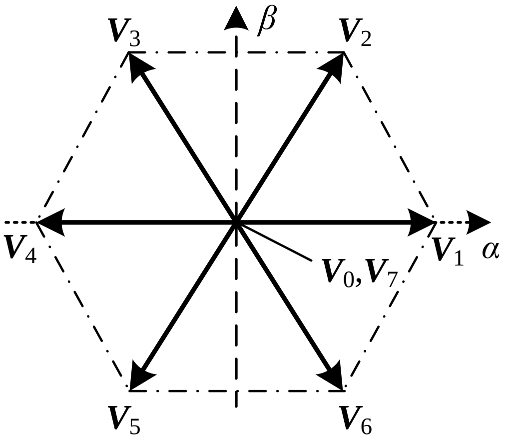

Fig.2-6 VSC voltage vectors

These voltage vectors are essentially generated based on the different switching states from the configuration of the VSC’s six switches. Switching states S_a, S_b and S_c are specified as a series of the combination of three binary variables. These combinations and corresponding switching states are summarized in Table 2-1. In this table, switching states are formed by the three switching bridge arms, the voltage vectors are given in both complex and exponential numbers.

Take $(S_a,S_b,S_c)=(1,0,0)$ for example, $S_a=1$ implies S_1 is ON and S_4 is OFF; $S_b=0$ means S_2 is OFF and S_5 is ON; while $S_c=0$ refers to S_3 is OFF and S_6 is ON. In this case, $\boldsymbol{V}_i$ equals to $\boldsymbol{V}_1$. Reversely, when $\boldsymbol{V}_i=\boldsymbol{V}_1$, the controller needs to produce a command of (1,0,0) for (S_a,S_b,S_c) to trigger the switches.

MPC can be used to control AC-DC interlinking converters, different operation modes should also be considered in the next subsection.

Table 2-1 Voltage vectors and corresponding switching states

Switching states			Voltage vector (V_i)
S_a	S_b	S_c	
0	0	0	$\boldsymbol{V}_0 = 0$
1	0	0	$\boldsymbol{V}_1 = (2/3)V_{dc}^*$
1	1	0	$\boldsymbol{V}_2 = (1/3)V_{dc}^* + j(\sqrt{3}/3)V_{dc}^*$ or $\boldsymbol{V}_2 = (2/3)V_{dc}^* e^{j(\pi/3)}$
0	1	0	$\boldsymbol{V}_3 = (-1/3)V_{dc}^* + j(\sqrt{3}/3)V_{dc}^*$ or $\boldsymbol{V}_3 = (2/3)V_{dc}^* e^{j(2\pi/3)}$
0	1	1	$\boldsymbol{V}_4 = (-2/3)V_{dc}^*$ or $\boldsymbol{V}_4 = (2/3)V_{dc}^* e^{j\pi}$
0	0	1	$\boldsymbol{V}_5 = (-1/3)V_{dc}^* + j(-\sqrt{3}/3)V_{dc}^*$ or $\boldsymbol{V}_5 = (2/3)V_{dc}^* e^{j(4\pi/3)}$
1	0	1	$\boldsymbol{V}_6 = (1/3)V_{dc}^* + j(-\sqrt{3}/3)V_{dc}^*$ or $\boldsymbol{V}_6 = (2/3)V_{dc}^* e^{j(5\pi/3)}$
1	1	1	$\boldsymbol{V}_7 = 0$

2.2.2 MPC under Islanded Mode

In islanded mode, in order to provide an AC supply for the AC loads, an LC filter which both smoothes the AC output current and stabilizes the AC output voltage is often attached to the VSC, as shown in Fig.2-7. Here, R_f, L_f, and C_f are the resistive, inductive, and capacitive component of the LC filter, respectively, $\boldsymbol{I}_f$ is the inductor current, $\boldsymbol{V}_c$ is the capacitor voltage, and $\boldsymbol{I}_o$ is the load current.

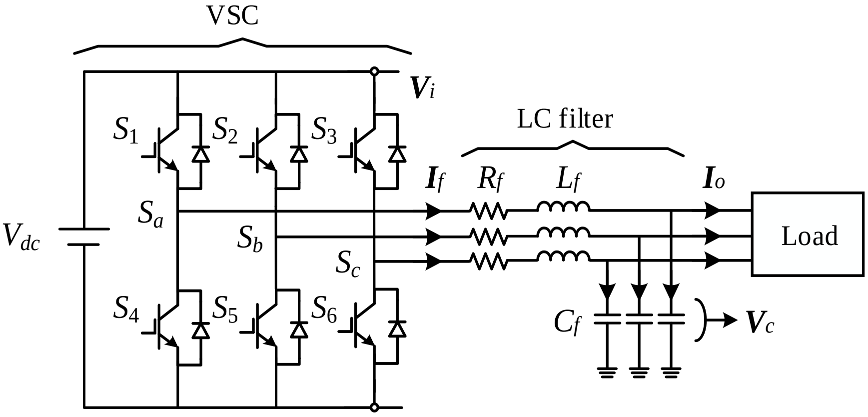

Fig.2-7 The VSC with LC filter under islanded mode

Applying Kirchhoff's current law (KCL) and recalling KVL, we have the following expressions

$$\boldsymbol{V}_i = \boldsymbol{I}_f R_f + L_f \frac{d\boldsymbol{I}_f}{dt} + \boldsymbol{V}_c \tag{2-8}$$

$$C_f \frac{d\boldsymbol{V}_c}{dt} = \boldsymbol{I}_f - \boldsymbol{I}_o \tag{2-9}$$

The above (2-8) and (2-9) can be integrated into the state-space form as

$$\frac{d\boldsymbol{x}}{dt} = A\boldsymbol{x} + B\boldsymbol{y} \tag{2-10}$$

where

$$\boldsymbol{x} = \begin{bmatrix} \boldsymbol{V}_c \\ \boldsymbol{I}_f \end{bmatrix},\ \boldsymbol{y} = \begin{bmatrix} \boldsymbol{V}_i \\ \boldsymbol{I}_o \end{bmatrix},\ A = \begin{bmatrix} 0 & 1/C_f \\ -1/L_f & -R_f/L_f \end{bmatrix},\ B = \begin{bmatrix} 0 & -1/C_f \\ 1/L_f & 0 \end{bmatrix}$$

In order for a better implementation on a practical processor, according to[83], (2-10) can be written into a discrete state-space model

$$\boldsymbol{x}(k+1)=e^{T_sA}\boldsymbol{x}(k)+\int_0^{T_s}e^{(T_s-t)A}Bdt\boldsymbol{y}(k) \tag{2-11}$$

Further, we have

$$\boldsymbol{x}(k+1)=e^{T_sA}\boldsymbol{x}(k)+A^{-1}(e^{T_sA}-\boldsymbol{I}_{2\times 2})B\boldsymbol{y}(k) \tag{2-12}$$

which is also the predictive model of the MPC for AC-DC interlinking converters under islanded mode.

Commonly, in order to provide a stable AC voltage supply for the AC loads under islanded mode using only DC power source available locally, the capacitor voltage $\boldsymbol{V}_c$ is needed to be tightly controlled. Therefore, the cost function in this instance is formulated as

$$J_V=(V_{c\alpha}^*-V_{c\alpha}(k+1))^2+(V_{c\beta}^*-V_{c\beta}(k+1))^2 \tag{2-13}$$

where the subscripts α,β mean the variables are located in the α-β coordinate plane, the superscript * stands for the reference which is considered as constant in the two consecutive intervals.

Keeping this cost function in mind, the voltage vector that makes J_V the minimum during one-cycle calculation will be delivered to the converter in the next sampling interval. Hence, through regulating the VSC switches, a stable AC voltage will be created.

The control diagram of the MPC for AC-DC interlinking converter under islanded mode is shown in Fig.2-8. The voltages and currents are measured for the predictive model (2-12), then the computed capacitor voltage V_c at k+1 instant is produced and used in the cost function (2-13). Once the best solution is figured out, the switch states and control signals are achievable to be sent to the VSC to realize a one-step conversion.

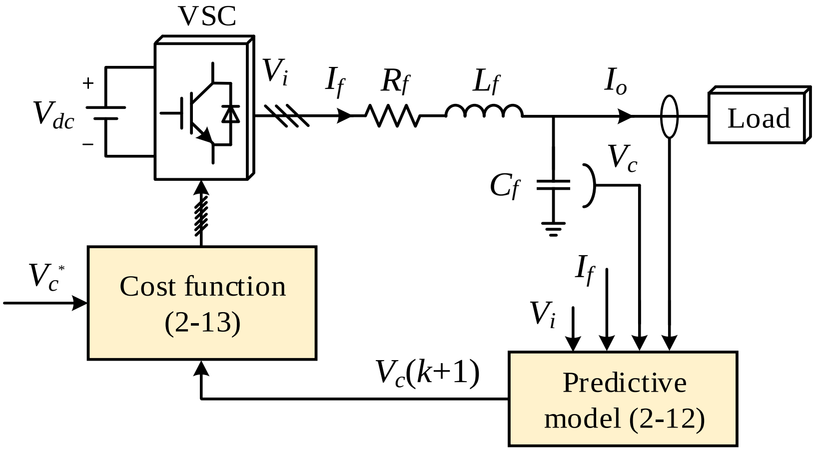

Fig.2-8 Control diagram of the MPC for AC-DC interlinking converter under islanded mode

2.2.3 MPC under Grid-connected Mode

In grid-connected mode, since the main grid with an infinite capacity can provide strong voltage support for the VSC, so only an L filter is usually equipped with the VSC, as shown in Fig.2-9.

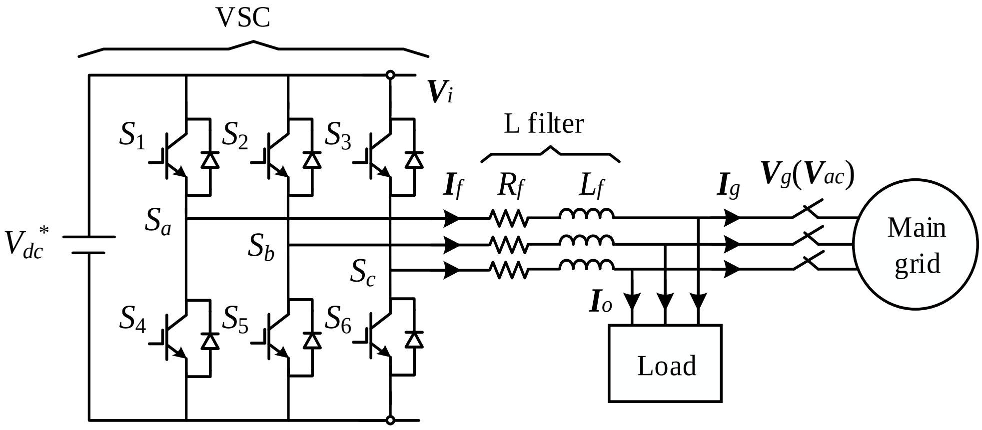

Fig.2-9 The VSC with L filter under grid-connected mode

Once more, applying KVL on the circuit drawn in Fig.2-9, the mathematical model in state-space form is obtained

$$\boldsymbol{V}_i = \boldsymbol{I}_f R_f + L_f \frac{d\boldsymbol{I}_f}{dt} + \boldsymbol{V}_g \tag{2-14}$$

where $\boldsymbol{V}_g$ is the voltage vector of the main grid.

For the VSC, the output active power P and reactive power Q flowing from the VSC into the main grid can be determined in the α-β coordinate plane by

$$P = \frac{3}{2}\left(V_{g\alpha} I_{f\alpha} + V_{g\beta} I_{f\beta}\right) \tag{2-15}$$

$$Q = \frac{3}{2}\left(V_{g\beta} I_{f\alpha} - V_{g\alpha} I_{f\beta}\right) \tag{2-16}$$

Make a derivative of the above two equations and according to $\boldsymbol{V}_g = V_{g\alpha} + jV_{g\beta} = \left|V_g\right|\cos(\omega t) + j\left|V_g\right|\sin(\omega t)$ and (2-14), one can get

$$\frac{d\boldsymbol{x}}{dt} = A\boldsymbol{x} + \frac{3}{2L_f}[B_1 \quad -B_2]\boldsymbol{y} \tag{2-17}$$

where

$$\boldsymbol{x} = \begin{bmatrix} P \\ Q \end{bmatrix},\ \boldsymbol{y} = \begin{bmatrix} \boldsymbol{V}_i \\ \boldsymbol{V}_g \end{bmatrix},\ A = \begin{bmatrix} -R_f / L_f & -\omega \\ \omega & -R_f / L_f \end{bmatrix},\ B_1 = \begin{bmatrix} V_{g\alpha} & V_{g\beta} \\ V_{g\beta} & -V_{g\alpha} \end{bmatrix},$$

$B_2 = \begin{bmatrix} V_{g\alpha} & V_{g\beta} \\ 0 & 0 \end{bmatrix}$, ω is the frequency in radians.

Applying (2-3), the discrete-time model of (2-17) can be expressed as

$$\boldsymbol{x}(k+1) = T_s A\boldsymbol{x}(k) + \frac{3T_s}{2L_f}[B_1(k) \quad -B_2(k)]\boldsymbol{y}(k) \tag{2-18}$$

Equation (2-18) is exactly the predictive model of MPC-controlled AC-DC interlinking converter under grid-connected mode.

With the solid and continuing support from the main grid, P and Q flows should be the control targets involved in the cost function as[84]

$$J_{PQ} = (P^* - P(k+1))^2 + (Q^* - Q(k+1))^2 \tag{2-19}$$

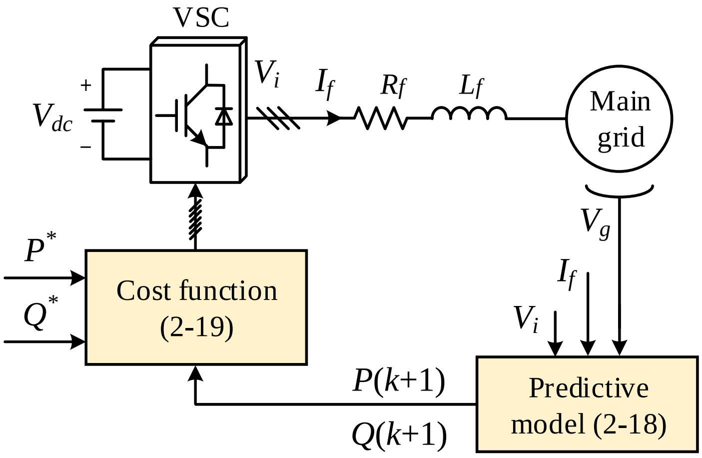

Fig.2-10 Control diagram of the MPC for AC-DC interlinking converter under grid-connected mode

The control diagram of the MPC for AC-DC interlinking converter under grid-connected mode is depicted in Fig.2-10. The predicted powers $P(k+1)$, $Q(k+1)$ can be generated via (2-18), then passing through (2-19) together with the given power references P^*, Q^*, the switching signals can be produced to drive the VSC.

2.3 DG Configuration and Modeling

Different kinds of DGs are the building blocks of MG systems. They either provide power generation on the basis of converting renewable energy or exchange power to charge/discharge the energy storage. Among them, some are highly susceptible to environmental factors like PV systems and WT systems; some have the ability to regulate bidirectional power flow like ESS systems. It is essential to analyse their characteristics before designing local power conversion and managing global power flow. In this section, the configuration and modeling of various DGs (e.g. PV, WT, and ESS systems) are introduced and discussed.

2.3.1 PV System

The PV system converts infinite and clean solar energy into electricity. In terms of the PV installed capacity and power generation, China has become the largest country since 2015, and it is supposed that China will increase its PV share of RESs from 20% to 35% by 2030[85]. Since PV generates DC current directly, a DC-DC converter is usually attached to the PV panel. This DC-DC converter is unidirectional, so a buck or boost DC-DC circuit is adopted. By this, not only the voltage is stepped down or up, but also the maximum power point tracking (MPPT) technique is enabled[86].

A PV system is built of several panels, while the panel is built of several solar cells connected in series or parallel thus to provide the desired output power. The most used PV solar cell model is drawn in Fig.2-11[87]. I_{ph} is the photocurrent of one single solar cell, I_D is the reverse saturation current of the diode, R_s is the series resistance, R_{sh} is the shunt resistance, I_o is the output current, and U_o is the output voltage.

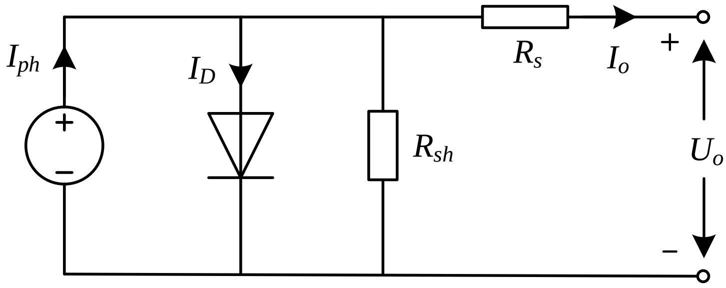

Fig.2-11 PV solar cell model

The value of the I_o is calculated by[88]

$$I_o = I_{ph} - I_D\left[\exp\left(\frac{U_o + R_s I_o}{V_T \eta}\right) - 1\right] - \frac{U_o + R_s I_o}{R_{sh}} \tag{2-20}$$

where V_T is the thermal voltage, η is the diode ideality factor.

Here, we use the basic and most-used PV model but have taken into account the fluctuant solar irradiation and ambient temperature to simulate the fluctuant power generation of renewable energies.

It is true that the power generation of PV system subjects to the environmental factors, like solar irradiation and ambient temperature. Different environment results in different output power. For instance, for a certain capacity PV panel (here, it is 350W), under the standard temperature 25℃, the curves of output power versus open-circuit voltage with different solar irradiations are plotted in Fig.2-12. It can be observed that different irradiations bring about different output powers with minor changes of open-circuit voltages. In reality, the power generation of the PV panel is sensitive to weather, cloud cover, and illuminance, etc. Moreover, in order to make the most of natural resources, it is needed to track the maximum power output to reduce the power loss, which is indeed the reason for performing MPPT[89,90].

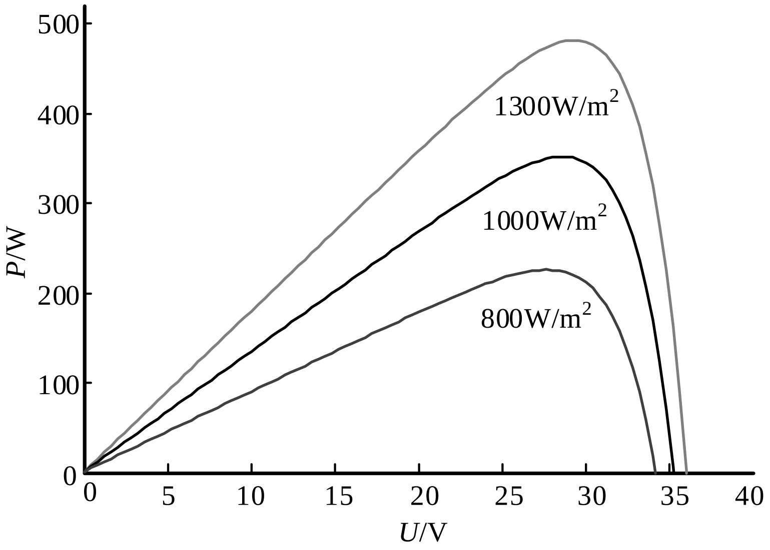

Fig.2-12 Output power versus open-circuit voltage with different solar irradiations

The realization of MPPT is relied on the DC-DC buck or boost circuit. Fig.2-13 shows the control diagram of the DC-DC boost converter with

MPPT. The voltage V and current I of PV panel are collected in an MPPT controller, then a duty ratio D is produced, when compared to a fixed-frequency carrier, the control signals are produced.

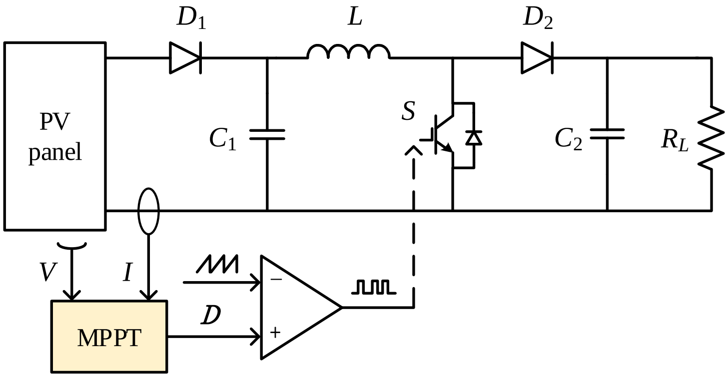

Fig.2-13 Control diagram of the DC-DC boost converter with MPPT

There are so many MPPT algorithms, the interested reader can refer to [86]. In this thesis, an incremental conductance method is adopted[91]. For a detailed control description, one can refer to [92]. In order to achieve the system power balance and according to the battery SOC, the DC-DC boost converter can operate either in on-MPPT or off-MPPT. This will be discussed further below.

2.3.2 WT System

It is reported that, by 2016, global installed WT capacity had accounted for around 53% of the total RES capacity, except conventional hydropower[93]. In 2018, China’s national wind power generation accounts for 6.1% of its total power generation[94]. From these reports, one can obviously see an important role and a promising future the WT system plays and exhibits. Fig.2-14 shows the configuration of the WT system based on a permanent-magnet synchronous generator (PMSG), where a rectifier is attached to provide a DC voltage output.

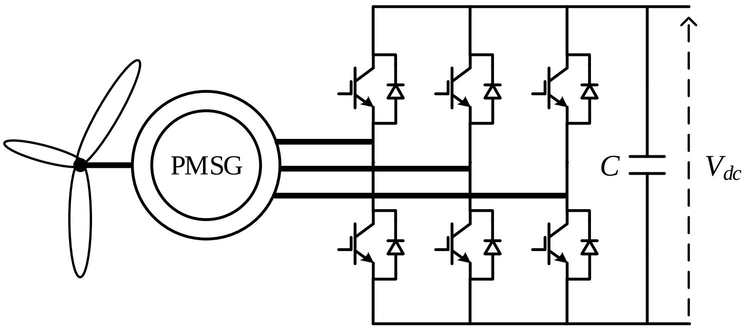

Fig.2-14 Configuration of the WT system based on the PMSG

The power driven by the wind and delivered by the rotor is expressed as[95]

$$P_m = 0.5\rho A C_p(\lambda,\beta) v_w^3 = 0.5\rho A C_p(\omega_m R / \lambda)^3 \qquad (2\text{-}21)$$

where ρ is the air density(kg/m^3), A is the swept area of blades(m^2), C_p is the coefficient which is determined by tip-speed ratio λ and pitch angle β (one can refer to [96]), v_w is the wind speed(m/s), R is the turbine radius(m), ω_m is the rotor rotational speed(rad/s), λ is given as $\omega_m R / v_w$.

Similar to the PV system and subjected to the environmental constraints, the WT system is also needed to be equipped with the MPPT technique, i.e. on-MPPT for the external power demand is required, off-MPPT for the power generation is surplus[97,98]. The curves of wind power versus turbine rotor speed with different wind speeds are drawn in Fig.2-15.

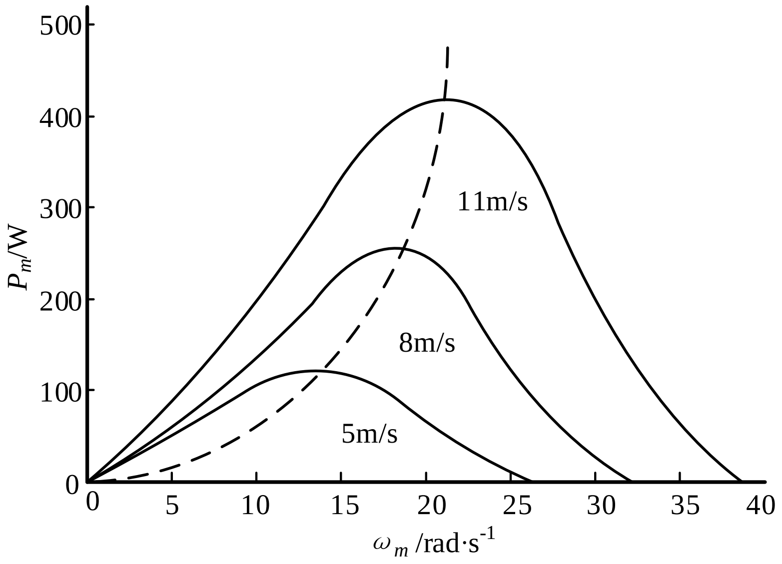

Fig.2-15 Wind power versus turbine rotor speed with different wind speeds

The model of the three-phase PMSG in the *d*-*q* reference frame is expressed as[96]

$$\begin{cases} \dfrac{di_{sd}}{dt} = -\dfrac{R_s}{L_d} i_{sd} + \dfrac{L_q}{L_d} p\omega_r i_{sq} + \dfrac{v_{sd}}{L_d} \\ \dfrac{di_{sq}}{dt} = -\dfrac{R_s}{L_q} i_{sq} - \dfrac{L_d}{L_q} p\omega_r i_{sd} - \dfrac{1}{L_q} p\omega_r \Phi_v + \dfrac{v_{sq}}{L_q} \end{cases} \tag{2-22}$$

where v_{sd} and v_{sq}, i_{sd} and i_{sq}, L_d and L_q are the *d*- and *q*- component of the stator voltage, stator current, stator inductance, respectively, R_s is the stator winding resistance, Φ_v is the magnetic flux linkage, *p* is the pole-pair number.

The detailed control strategy of the WT system is described in [91]. The torque reference T_e^* is obtained from the MPPT. Based on the inertia *J*, pole-pair number *p* and magnetic flux linkage Φ_v, the *q*- component of the stator current i_{sq}^* is computed. Then, by using the PI controller and coordinate transformation, the stator voltage reference $v_{sa,b,c}$ for the rectifier is obtained according to (2-22).

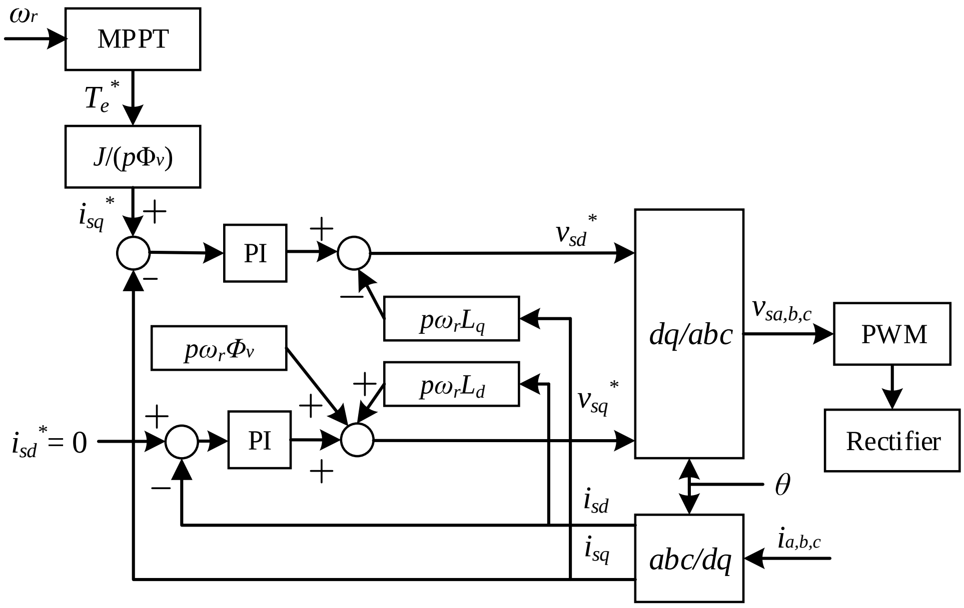

Fig.2-16 Control diagram of the WT system

The error between the turbine torque and generator torque will determine whether to accelerate or decelerate the generator. For example, if the generator speed is less than the MPPT provided optimal speed, the turbine torque should become larger than the generator torque so to accelerate the generator. In contrast, the generator will be decelerated.

2.3.3 ESS System

In an MG system, equipping the ESS system is a feasible and valid way to stabilize and smooth the fluctuation and disturbance caused by the RES and load change. The ESS system is usually used to attach the RES on the DC side to jointly provide a DC supply. The battery (e.g. Li-ion, supercapacitor, lead-acid, etc) and DC-DC converter (e.g. buck, boost, buck-boost, etc) are the two main components of the ESS[99,100]. The details of the ESS with a bidirectional DC-DC buck-boost converter are given in Fig.2-17, where the battery is simulated as a DC power source connected to the LV port.

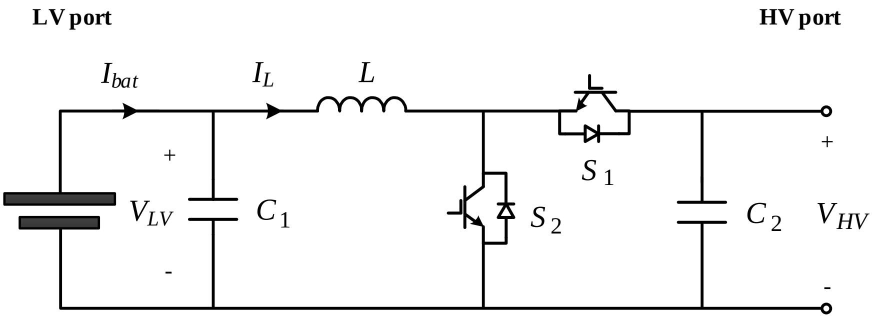

Fig.2-17 Configuration of the ESS system

The SOC of the battery is a key parameter reflecting the battery performance especially about the residual capacity of the battery. The SOC is calculated as

$$\mathrm{SOC}(t) = 100\% \cdot \left(1 - \frac{\int_0^t I_d(t)dt}{Q_0}\right) \tag{2-23}$$

where SOC value is between 0 (for an empty battery) and 100% (for a fully charged battery). I_d is the discharging current, Q_0 is the battery capacity.

In this thesis, by default, in grid-connected operation, the battery works in constant current control while in islanded it is mainly in constant voltage control. Also, the range of SOC is set as 10%~90% to avoid battery over charge/discharge.

The diagram of the battery model is depicted in the following Fig.2-18[101,102].

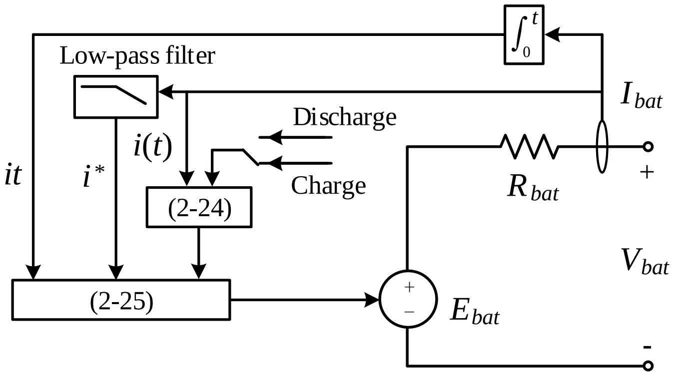

Fig.2-18 Diagram of the battery model

The discharge and charge of the battery result in different state variable, which is presented in the S domain as

$$\frac{Exp(s)}{Sel(s)}=\frac{A_e}{1/(B_e\cdot i(t))s+1} \tag{2-24}$$

where A_e is the exponential voltage, B_e is the exponential capacity, $i(t)$ is the battery current.

The terminal voltage expression of the battery varies with the battery types, for Li-ion battery, it is[103]

$$\begin{cases} E_{bat,\text{discharge}}=E_0-K\dfrac{Q_{0max}}{Q_{0max}-it}i^*-K\dfrac{Q_{0max}}{Q_{0max}-it}it+A_e\exp(-B_e\cdot it) \\ E_{bat,\text{charge}}=E_0-K\dfrac{Q_{0max}}{it+0.1Q_{0max}}i^*-K\dfrac{Q_{0max}}{Q_{0max}-it}it+A_e\exp(-B_e\cdot it) \end{cases} \tag{2-25}$$

where E_0 is the constant voltage, K is the polarization constant, Q_{0max} is maximum battery capacity, it is the extracted capacity, i^* is the low-frequency current dynamics.

The charging or discharging action of the battery is determined on the basis of the gap between the power generation and power consumption, aiming at maintaining a power-balanced system. This will be elaborated later.

2.4 Hierarchical Control of MGs

In reality, hierarchical control is frequently used in complex control systems and networks, like large electric power systems[104], process industries[105] and discrete event systems[106], etc. To mimic the hierarchical control of large electric power systems that typically has three levels, MGs also build up its own three-level hierarchical control architecture namely primary control, secondary control, and tertiary control. Each control level with the different targets and functions will be elaborated in the following subsections.

2.4.1 Primary Control

The parallel operation of various DG-interfaced converters is the common feature of MGs, where the active power *P* and reactive power *Q* should be accurately and proportionally shared. As aforementioned in Subsection 1.4, the droop control method is a useful and convenient method for the control of parallel converters in islanded MGs.

The principle of the frequently-used droop control method, for inductive line impedance, is to decrease the frequency *f* when *P* increases, while to decrease the VSC output voltage magnitude *E* when *Q* increases. This process is also called *P-f* and *Q-E* droop control, which can be expressed as[5,24]

$$f = f^* - G_P(s) \cdot P \tag{2-26}$$

$$E = E^* - G_Q(s) \cdot Q \tag{2-27}$$

where f^* and E^* are the frequency and voltage references, $G_P(s)$ and $G_Q(s)$ are the control gains in the *S* domain, respectively. Usually, in islanded mode, in order for a proportional power sharing among loads, the two control gains are set to pure proportional gains, i.e. $G_P(s) = m$ and $G_Q(s) = n$, and in this case, they are defined by

$$m = \Delta f \,/\, P_{\max} \tag{2-28}$$

$$n = \Delta E \,/\, Q_{\max} \tag{2-29}$$

where Δf and ΔE are the allowable *f* and *E* maximum deviations, $P_{\max}$ and $Q_{\max}$ are the maximum *P* and *Q* delivered by the VSC. Fig.2-19 shows the *P-f* and *Q-E* droop curves. It can be seen that when positive *P* is required, the *f* is lower than the reference f^*, this process is the same for the *Q* curve.

The VSC and current source converter (CSC) are two frequently-used power electronics converters[17,107]. In order to control the VSC which is mainly used to stabilize the output voltage, both an outer voltage loop and an inner current loop are conventionally needed. While for the CSC, only a current loop is sufficient to provide a continuous current supply. In contrast with CSCs which are normally used in grid-connected mode, VSCs can work in both grid-connected mode (serving as CSCs) and islanded mode, providing a more flexibility for the MG application. In order to drive the converter switches, except the voltage/current loop, a PWM generator is also a necessity for the VSCs. For example, in islanded mode, the outer voltage loop of the VSC control will send a voltage reference to the PWM generator to generate the control signals.

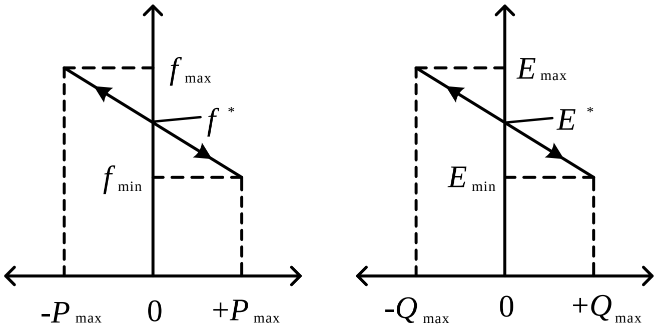

Fig.2-19 *P*-*f* and *Q*-*E* droop curves

In sharp contrast with the above-mentioned voltage/current loop (belonging to the CLC), MPC does not need the additional PWM generator to generate control signals. Also, as aforementioned in Subsection 1.3, the conventional voltage/current loop is replaced by the predictive model and cost function[108,109]. Fig.2-20 compares the primary control diagram using CLC and MPC.

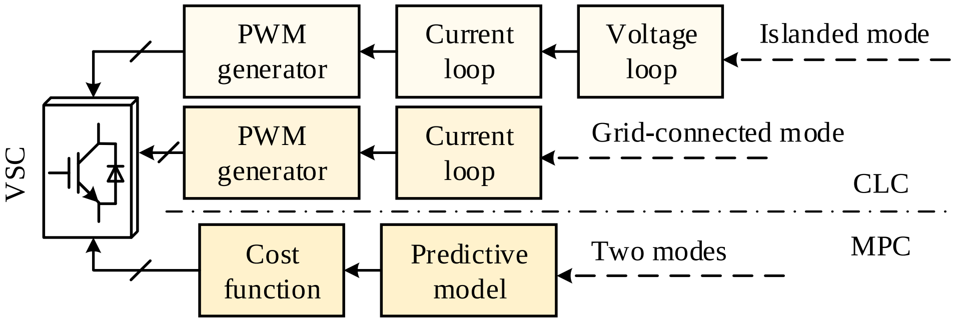

Fig.2-20 Primary control diagram

As for the change of operation modes, the predictive model or cost function can be redesigned for the MPC to well realize the control target change, while keeping the MPC control form unchanged. The difference between MPC and CLC is that the former MPC can easily involve constraints, like the battery SOC, flowing power limits, current/voltage magnitude limit, etc. In addition, MPC will be more advantageous than CLC since the circuit model is more precisely simulated and considered. The comparisons in several certain scenarios will be elaborated further in later chapters.

2.4.2 Secondary Control

As shown in Fig.2-19, when loads increase, the system operating point presents a drooping tendency, resulting in the *f* and *E* deviations from their respective references. This is unavoidable due to the intrinsic property of droop control[5,49]. The deficiency brought by primary control may damage the appliances since they are working in the under-frequency and under-voltage situations.

In view of the above problems, the secondary control can be introduced to compensate the *f* and *E* deviations. The secondary control can correct or pull the deviated curves back to the rated values and within the allowable band range, e.g. ±2% of 50Hz frequency and ±6% of 220V voltage in Hong Kong[110]. The classical secondary control is to shift the droop curve upward to a certain degree so that the system can reach the references, as shown in Fig.2-21. Correspondingly, the formulas of the secondary control are expressed as

$$f = f^* - G_P(s) \cdot P + \Delta f \tag{2-30}$$

$$E = E^* - G_Q(s) \cdot Q + \Delta E \tag{2-31}$$

where Δf and ΔE are the compensated frequency and voltage values within the allowable band range.

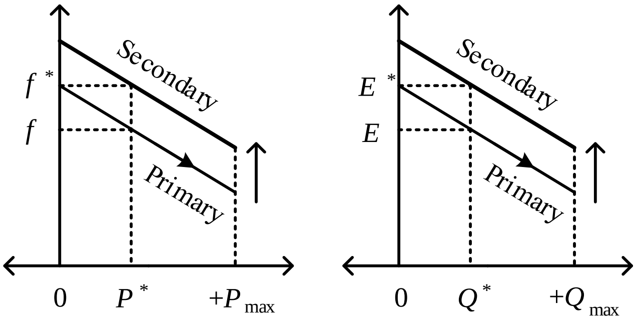

Fig.2-21 Droop curves with secondary control

To realize the secondary control, the common method is to employ a proportional-integral (PI) controller in a centralized manner. This controller is able to eliminate oscillations and achieve zero steady-state errors[111]. These PI-controlled formulas are written as

$$\Delta f = k_{pf}(f^* - f) + k_{if}\int(f^* - f)dt = f_c \tag{2-32}$$

$$\Delta E = k_{pE}(E^* - E) + k_{iE}\int(E^* - E)dt = E_c \tag{2-33}$$

The control process is demonstrated in Fig.2-22. In order to restore the deviated AC bus and maintain a stable supply, the measurements f and E from the AC bus or the PCC should be measured by the phase-locked loop (PLL) and the voltage probe. The PLL consists of a frequency or phase feedback control loop which generates the frequency or phase difference between inputs and outputs. With these measurements, the secondary control can compensate the deviated errors, then interface with the primary control.

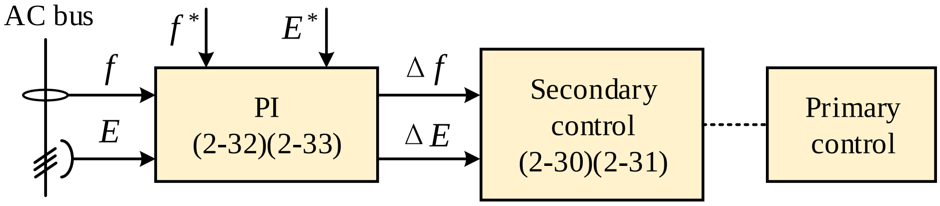

Fig.2-22 Secondary control diagram

2.4.3 Tertiary Control

Tertiary control is mainly associated with the grid-connected MGs where the power exchange between the MG and the main grid is focused. Besides, based on the power exchange, economic optimization, cost estimation, and power planning can all be considered in the tertiary control regime. Since tertiary control is not the emphasis of this thesis, so here only the power exchange is investigated.

Next, as for the power regulation, tertiary control using CLC and MPC are respectively presented. For CLC, the tertiary control needs another loop, aiming at regulating exchange powers, to produce the frequency and voltage references for the secondary control. Similar to the secondary control using CLC, the power loop in tertiary control using CLC is also based on the PI controller, which can be defined as[5]

$$f^* = k_{pP}(P^* - P) + k_{iP}\int (P^* - P)dt \tag{2-34}$$

$$E^* = k_{pQ}(Q^* - Q) + k_{iQ}\int (Q^* - Q)dt \tag{2-35}$$

where k_{pP}, k_{pQ} are proportional coefficients, k_{iP}, k_{iQ} are integral coefficients.

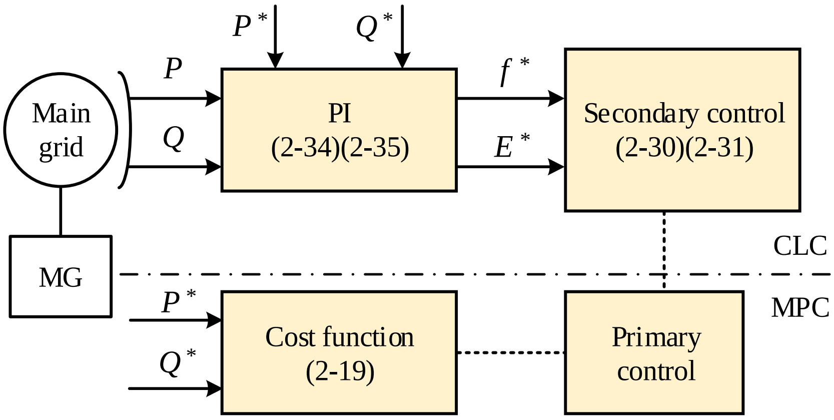

Fig.2-23 Tertiary control diagram

While for MPC, the power regulation can be done in the cost function, as given in (2-19), just simply setting the power references. Tertiary control methods using CLC and MPC are compared in Fig.2-23.

As for the time frames in MG's hierarchy, normally, the primary is at tens of milliseconds, secondary is hundreds of milliseconds while tertiary can be several seconds or longer. So far there have been no standard time frames for each control level because it is determined by many reasons, like the filter, control parameters, operating points, etc.

In this thesis, since various MPC schemes will be developed, one concern comes to how to coordinate different types of DGs, some use CLC control while others use MPC control. In fact, this can be solved in the hierarchical control architecture. In islanded mode, the primary droop control will coordinate DGs for their power sharing, then the CLC or MPC controller will stabilize *f/V* via the VSC. In grid-connected mode, since the microgrid is strongly supported by the stiff grid, then each DG can only use CLC or MPC to manage their own power flows. In other words, MPC methods can coexist with CLC methods.

2.5 Summary

In this chapter, the common MPC-controlled bidirectional DC-DC converter and AC-DC interlinking converter are respectively illustrated. Besides, the MPC methods under islanded mode and grid-connected mode are both involved for each kind of converters, along with specifically designed cost functions and different functional capabilities. These MPC methods will be applied and discussed in different MG scenarios in the following chapters. Next, different kinds of DGs, especially those sensitive to environmental aspects like PV and WT systems as well as the device to smooth the error between generation and consumption like the ESS system, are modeled and analysed. The parallel operation of DGs results in several inherent limitations like the frequency and voltage deviations, so the hierarchical control with three different levels to address different issues is presented.

Chapter 3 MPC for PV-WT-ESS MGs

In this chapter, the aforementioned various MPC control methods for the power converters working under different operation modes are applied to a PV-WT-ESS MG system. For a better MG application, the MPC control methods will be further designed or incorporated.

3.1 Background and System Configuration

According to the previous statement about the drawbacks of the CLC method in Subsection 1.2, the oscillations of the DC-bus voltage caused by fluctuating RESs may further deteriorate AC-side power quality. In addition, the effectiveness of droop control method may also be deteriorated by combining the CLC method. Another concern comes from the necessity to replace the ideal DC power sources which are usually used to simulate a variety of RESs in existing researches by a practical DC bus, where the intermittent nature of such RESs is involved. Therefore, in this section, the above concerns have been investigated and addressed.

The configuration of the PV-WT-ESS MG investigated in this chapter is displayed in Fig.3-1. Here, a PV system and a WT system, as typical examples of RESs, are adopted. Also, an ESS system as another typical DG is used to interconnect with PV and WT systems. PV, WT and ESS systems are set up according to Subsection 2.3. For the entire system setup, there are two parts: DC-side subgrid with DC loads and AC-side subgrid with AC loads. Through a bidirectional DC-DC converter, the ESS is linked to the DC bus. While through a bidirectional AC-DC interlinking converter, the DC bus is interconnected with the AC bus.

There is an STS switch located between the MG and the main grid as plotted in Fig.3-1. This results in the multiple operation modes of the MG system: islanded mode, grid-connected mode, grid synchronization, and islanding transition. There are two-type links, i.e. electric power link and communication link in Fig.3-1. The electric power link constructs the physical architecture of the MG system, while the communication link exchanges command or measurement data inside the system. Loads 1 and 2 are DC loads, while Loads 3 and 4 are AC loads. The load status may alter due to the scheduled or modified user requirement.

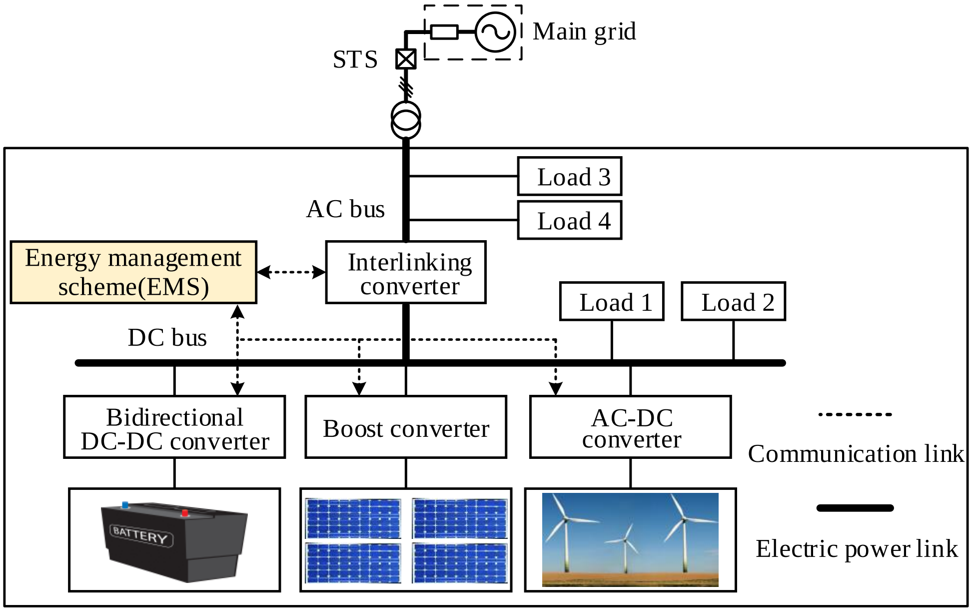

Fig.3-1 Configuration of the PV-WT-ESS MG

3.2 MPC Control Schemes

In order to better regulate the power conversion and manage the power flow of the PV-WT-ESS MG, an MPCPC scheme for the bidirectional DC-DC converter and an MPVPC scheme for the AC-DC interlinking converter are proposed here. By these schemes, DC-side and AC-side subgrids are well controlled in multiple operation modes, providing a sound and robust MG system.

3.2.1 MPCPC Scheme

Similar to Fig.2-17, the configuration of the bidirectional DC-DC converter used here is shown in Fig.3-2. L_{bf} is the battery-side filter to reduce the current ripple, which is less than inductor L. The battery side is the low voltage V_{LV}, while the DC-bus side is the high voltage $V_{dc}(V_{HV})$.

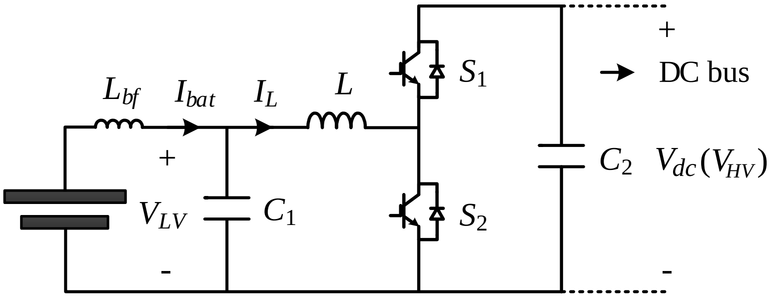

Fig.3-2 ESS system configuration

In the DC-side subgrid, when the MG is connected to the main grid, the MPC control of the bidirectional DC-DC converter will be simple with only the battery currents taken into account. This results in the following cost function to charge or discharge the battery

$$\begin{aligned} &J_I = \left| I_L^* - I_L(k+1) \right| \\ &s.t.\ \mathrm{SOC}_{\min} \le \mathrm{SOC} \le \mathrm{SOC}_{\max},\ I_L \le \left| I_{bat\_rated} \right| \end{aligned} \tag{3-1}$$

where I_L^* is the battery current reference which can be determined as per the time-of-use electricity price. In this thesis, the references are considered to be unchanged during k and k+1 instants, so for the references, the notes of k are omitted, except where specified. $I_L(k+1)$ can be obtained from the predictive model as expressed in (2-4), here the inductor current I_L is thought to be identical to the battery current I_{bat} in the steady state. To solve the cost function, at the same time, consider the battery performance, the constraints of the SOC and I_{bat} are involved.

When the MG turns in an autonomous operation, in order to keep a power balance between the generation and consumption, the ESS should be managed properly. Fig.3-3 shows the internal current flow of the MG, where currents flow among the RES, ESS and the rest of the MG (ROM).

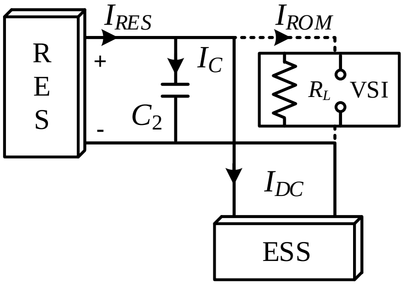

Charging

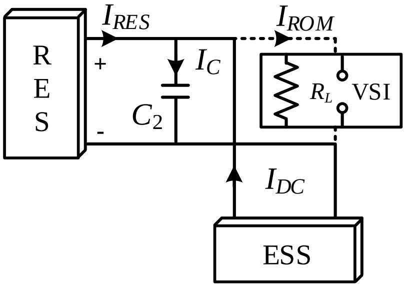

Discharging

Fig.3-3 Internal current flow of the MG

Applying KCL, we have the current relationship from Fig.3-3, which is expressed as

$$I_{DC} = I_{RES} - I_C - I_{ROM} \tag{3-2}$$

where I_{DC} is the current flowing through DC bus, I_{RES} is the output current from RES, I_C is the current of capacitor C_2, I_{ROM} is the current flowing to the ROM.

Our goal is to control the ESS charge or discharge, thus to keep the power balance, which results in the required power reference at k+1 instant should be defined as

$$P_{ESS}^{*}(k+1) = \left| I_{DC}(k+1) \cdot V_{dc}^{*} \right| \tag{3-3}$$

where V_{dc}^{*} is the DC-bus voltage reference.

The DC-side capacitor C_2 directly affects DC-side voltage V_{dc}. By analysing capacitor dynamics, we get the capacitor current $I_C = C_2 dV_{dc}/dt$. This means we can change V_{dc} to get the desired I_C. With the aim of keeping V_{dc} around V_{dc}^*, here, we assume that the transition from V_{dc} to V_{dc}^* presents a linear change over a short period, as illustrated in Fig.3-4. Here, N is the prediction horizon (an integer coefficient) used to restrict the value of the capacitor current I_C that is not to be randomly large. Besides, N also means $V_{dc}(k)$ will reach the value of V_{dc}^* in N steps[112].

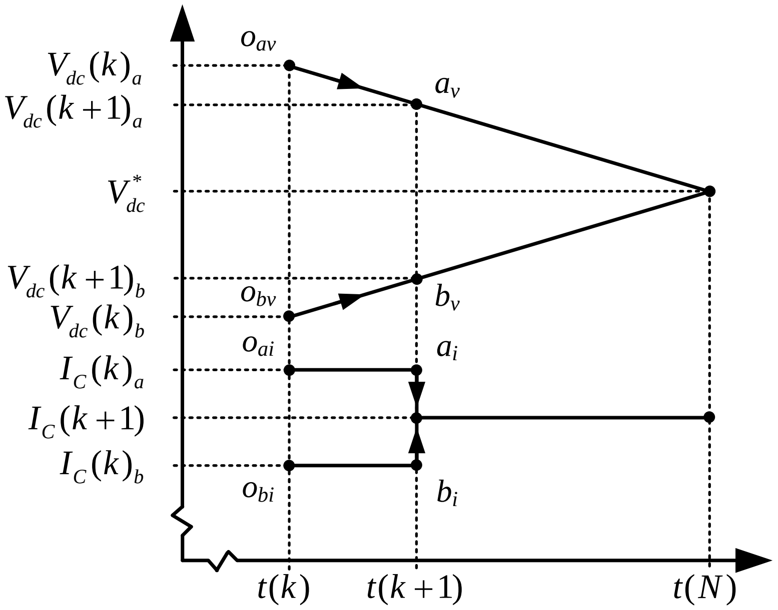

Fig.3-4 Linear relationship of I_c and V_{dc}

In Fig.3-4, at k instant, as for the rated DC voltage V_{dc}^*, $V_{dc}(k)_a$ needs to be decreased from point o_{av} to a_v or $V_{dc}(k)_b$ needs to be increased from point o_{bv} to b_v, thus to approximate the final desired value V_{dc}^*. Correspondingly, these actions result in $I_C(k)_a$ should step down or $I_C(k)_b$ should step up. According to the linear relation in Fig.3-4, we have

$$\frac{V_{dc}(k)-V_{dc}(k+1)}{1}=\frac{V_{dc}(k)-V_{dc}^{*}}{N} \tag{3-4}$$

Then

$$V_{dc}(k+1)=V_{dc}(k)+\frac{1}{N}(V_{dc}{}^{*}-V_{dc}(k)) \tag{3-5}$$

Applying (2-3) to the equation $I_C = C_2 dV_{dc}/dt$ and using (3-5), it has

$$I_C(k+1)=\frac{C_2}{T_s}(V_{dc}(k+1)-V_{dc}(k))=\frac{C_2}{NT_s}(V_{dc}{}^{*}-V_{dc}(k)) \tag{3-6}$$

Next, it is supposed that capacitor C_2 influences the ESS dynamics more than others[113]. So, we get

$$I_{DC}(k+1)=I_{RES}(k)-I_{\mathrm{C}}(k+1)-I_{ROM}(k) \tag{3-7}$$

This means, based on (3-7), one can calculate I_{DC} value at k+1 instant and then (3-3) is solved.

Considering the battery voltage V_{LV} has a relatively slower change rate, so we assume $V_{LV}(k)=V_{LV}(k+1)$, and the actual output power of the battery is given as

$$P_{bat}(k+1)=\left|I_L(k+1)\cdot V_{LV}(k)\right| \tag{3-8}$$

Under the islanded autonomous operation, the aim is to keep the power balance inside the MG, so the following cost function should be minimized

$$\begin{aligned}&J_P=\left|P_{ESS}^{*}(k+1)-P_{bat}(k+1)\right|\\&s.t.\ \mathrm{SOC}_{\min}\le \mathrm{SOC}\le \mathrm{SOC}_{\max},\ I_L\le\left|I_{bat\_rated}\right|\end{aligned} \tag{3-9}$$

The proposed MPCPC strategy is illustrated in Fig.3-5. When grid-connected mode works, the battery voltage V_{LV}, and the inductor current I_L, as well as the DC-bus voltage V_{dc}, will be used to predict the battery current $I_L(k+1)$ according to (2-4), thus the charging or discharging current of the battery can be predicted. Utilizing the cost function (3-1) as a criterion, the control target will be realized by solving it. In islanded mode, the ESS is intended to construct a constant-voltage DC bus. The RES output current I_{RES}, the current flowing to DC loads and the AC-side inverter I_{ROM}, DC-bus voltage V_{dc} and its reference $V_{dc}{}^{*}$ are all taken into account to calculate the required predicted ESS power $P_{ESS}{}^{*}(k+1)$ according to the equation combination (3-6), (3-7) and (3-3). Meanwhile, the predictive model (2-4) together with the battery voltage V_{LV}, are used to obtain the value of $P_{bat}(k+1)$ as per (3-8). Then, the switching actions are generated based on the minimal result from (3-9).

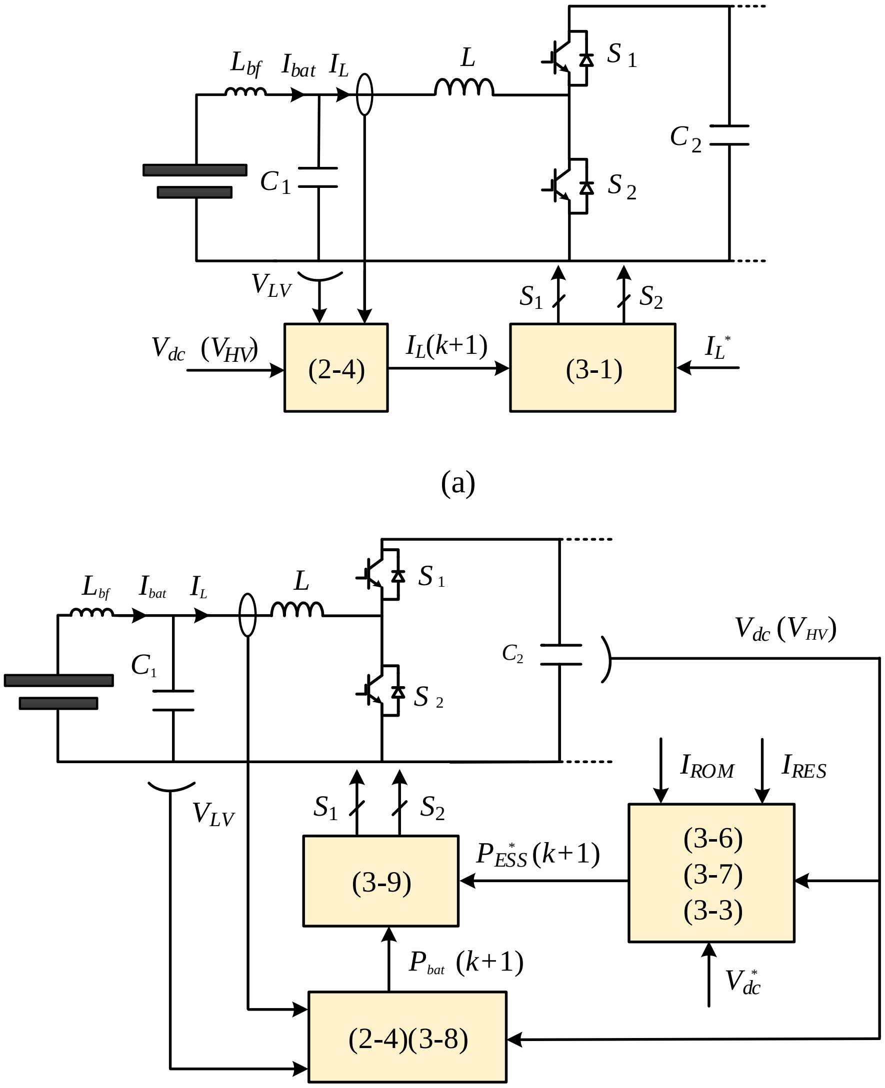

(a)

(b)

Fig.3-5 Control diagram of the MPCPC scheme. (a) grid-connected operation, (b) islanded operation.

By minimizing the cost function, selected optimal switching signals are produced and applied to the switching devices S_1 and S_2. Thus, a stable DC bus can be maintained as a common DC source for DGs and AC-DC interlinking inverters.

3.2.2 MPVPC Scheme

The configuration of the AC-DC interlinking converter (based on the VSC) investigated here is shown in Fig.3-6. When the MG system is operating in islanded mode, the primary thing is to provide a stable AC voltage supply. With this aim, the AC-DC interlinking converter which acts as an uninterruptible power supply (UPS) can be used to provide a stable AC voltage for AC loads. This leads to the necessity of taking filter capacitor voltages into the cost function, as expressed in (2-13). As for the predictive model, which is housed in (2-12).

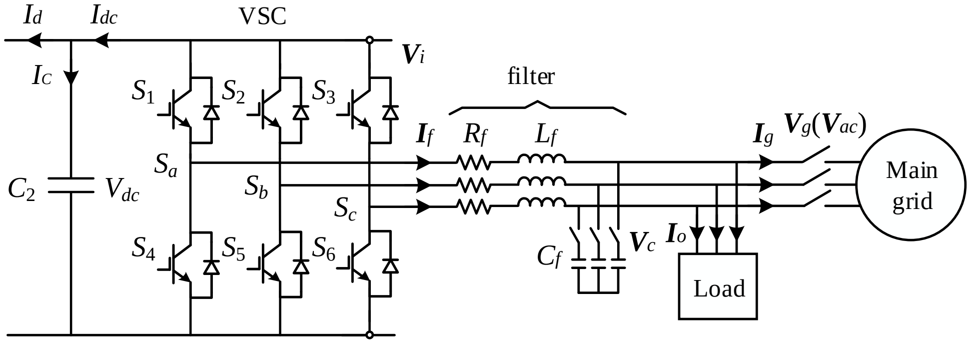

Fig.3-6 AC-DC interlinking converter in the PV-WT-ESS MG

In grid-connected mode, the DC bus is needed to be maintained stable by the AC-DC interlinking converter to supply the DC loads from the AC source. Besides, the power between the MG and the main grid should also be exchanged bidirectionally. In this case, the cost function can be designed as expressed in (2-19), while the predictive model can be used with (2-18).

Generally, Q^* is set to 0Var, aiming to track a desired zero Q and a unity power factor. With this setting, the only remaining thing is to determine the active power reference P^*.

Apply KCL at the DC side of the VSC shown in Fig.3-6, and assume the capacitor C_2 responds faster, one can obtain[112,113]

$$I_{dc}(k+1)=I_C(k+1)+I_d(k) \tag{3-10}$$

Then, the DC-side predictive power is computed by

$$P_{dc}(k+1)=V_{dc}(k+1)I_{dc}(k+1) \tag{3-11}$$

The power delivered between the DC side and AC side should be identical, regardless of the power loss. However, in practice, the power line loss between the VSC and the main grid should be respected. Here, define AC-side predicted power as $P_{ac}(k+1)$, we have the following relationship

$$P_{ac}(k+1)-\frac{2R_f}{3}\left(\frac{P_{ac}(k+1)}{V_{ac}}\right)^2=P_{dc}(k+1) \tag{3-12}$$

where V_{ac} indicates the AC-side voltage.

By solving (3-12), the following equation can be obtained, which is also the active power reference P^*

$$P^*=\frac{3V_{ac}^2}{4R}\left(1-\sqrt{1-\frac{8R}{3V_{ac}^2}P_{dc}(k+1)}\right)=P_{ac}(k+1) \tag{3-13}$$

Once P^* is obtained, the grid-connected MPC design process is completed. Together with (2-12) and (2-13), the complete MPVPC scheme is obtained.

Fig.3-7 shows the control diagram of the MPVPC scheme. Similar to the process shown in Fig.3-5. The system models (2-12) and (2-18) are utilized to predict the actual system variables at the next sampling instant. The cost functions (2-13) and (2-19) are designed as the criteria to produce and deliver the selected optimum voltage vector to the VSC. Then by inputting the references, i.e. the voltage reference (V_C^*) for islanded mode and the power references (P^* and Q^*) for grid-connected mode, the cost function is activated. In Fig.3-7(a), a grid synchronization procedure is also included for the MG transferring from islanded mode to grid-connected mode. Besides, the grid synchronization can also provide the grid voltage reference for the cost function.

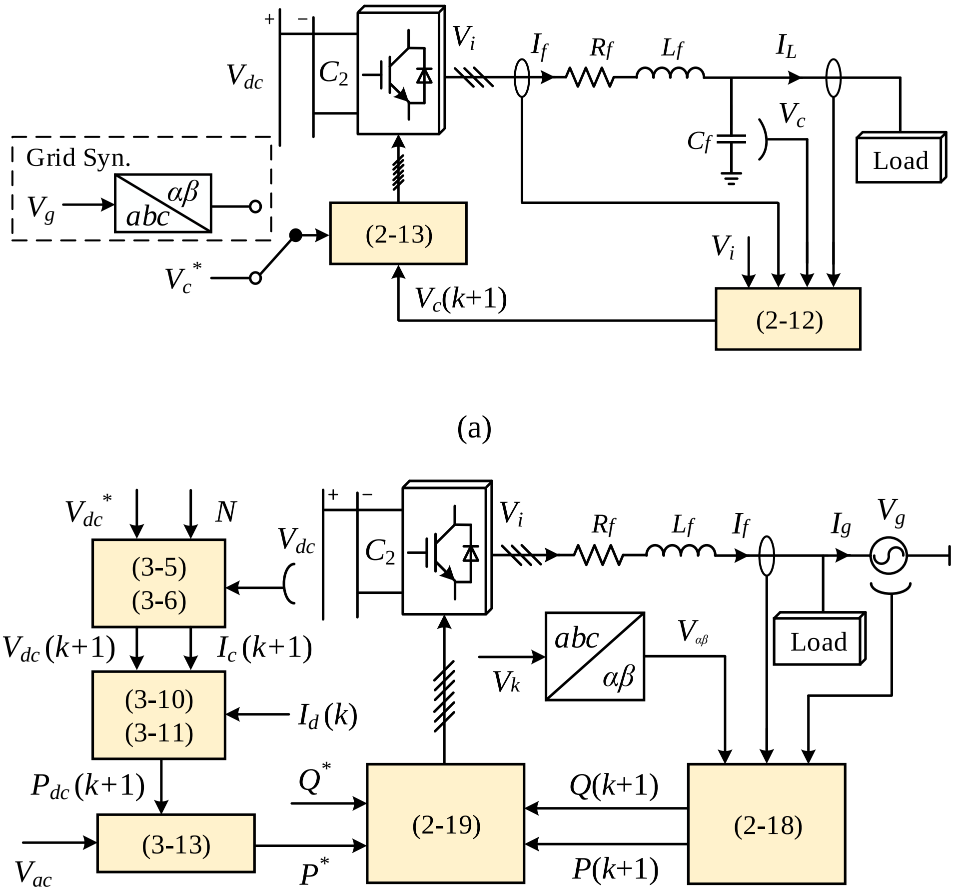

(a)

(b)

Fig.3-7 Control diagram of the MPVPC scheme. (a) islanded operation, (b) grid-connected operation.

3.3 System-level EMS

As for a complicated MG system, a system-level EMS is necessary for the MG’s successful operation[114,115]. The EMS should comprehensively take into account the power flow inside the whole system, i.e. the power balance between generation and consumption, this is expressed as

$$\begin{cases} P_{pv}+P_w+P_{bat}+P_g-P_{loss}=P_{acL}+P_{dcL} \\ P_{net}=P_{pv}+P_w-P_{acL}-P_{dcL}-P_{loss} \end{cases} \tag{3-14}$$

where P_{pv} is the PV output power, P_w is the WT output power, P_{bat} is the battery power, P_g is the power exchanged with the main grid, P_{loss} is the total power loss, P_{acL} represents the AC load power consumption, P_{dcL} represents the DC load power consumption. The net power P_{net} is defined as the summation of P_{pv} and P_w subtracted by P_{acL}, P_{dcL}, and P_{loss}. Positive P_{bat} means the battery is discharging while negative means reversely charging. Positive P_g means absorbing power from the main grid while negative means reversely releasing the power to the main grid.

The overall system-level EMS is illustrated in Fig.3-8. It starts with collecting the measurements from the meters dispersed through the MG system. Then the need for whether connected to the main grid should be determined, i.e. to decide whether to work in grid-connected mode or islanded mode.

1) When the MG is in grid-connected mode, MPCPC with (3-1) and MPVPC with (2-19) are used based on the actual price of the power grid ($/kWhr). When the price is high, in order to achieve an economic operation, the battery should discharge in the case of the SOC is not the minimal, otherwise, the battery should be set idle to prevent excessive discharge. While when the price is low, the battery should charge in the case of the SOC is not the maximal, otherwise, the battery should be in idle state. Here, a deadband with upper and lower limits is also adopted for the battery to be in idle state.

2) When the MG is in islanded mode, MPCPC with (3-9) and MPVPC with (2-13) are used. In this context, the estimation of the net power will be a criterion to set the battery states. When there is no redundant power inside the MG, in the case of the battery SOC is not the minimal, if P_{bat} reaches the maximum, MPPT, load shedding and battery discharging at rated power rate are all necessary; if P_{bat} is not the maximum, both MPPT and battery discharging are needed. Otherwise, when net power is still available, and if the SOC is maximal, off-MPPT and battery idle are activated; if the SOC is not maximal, both MPPT and battery charging should be maintained.

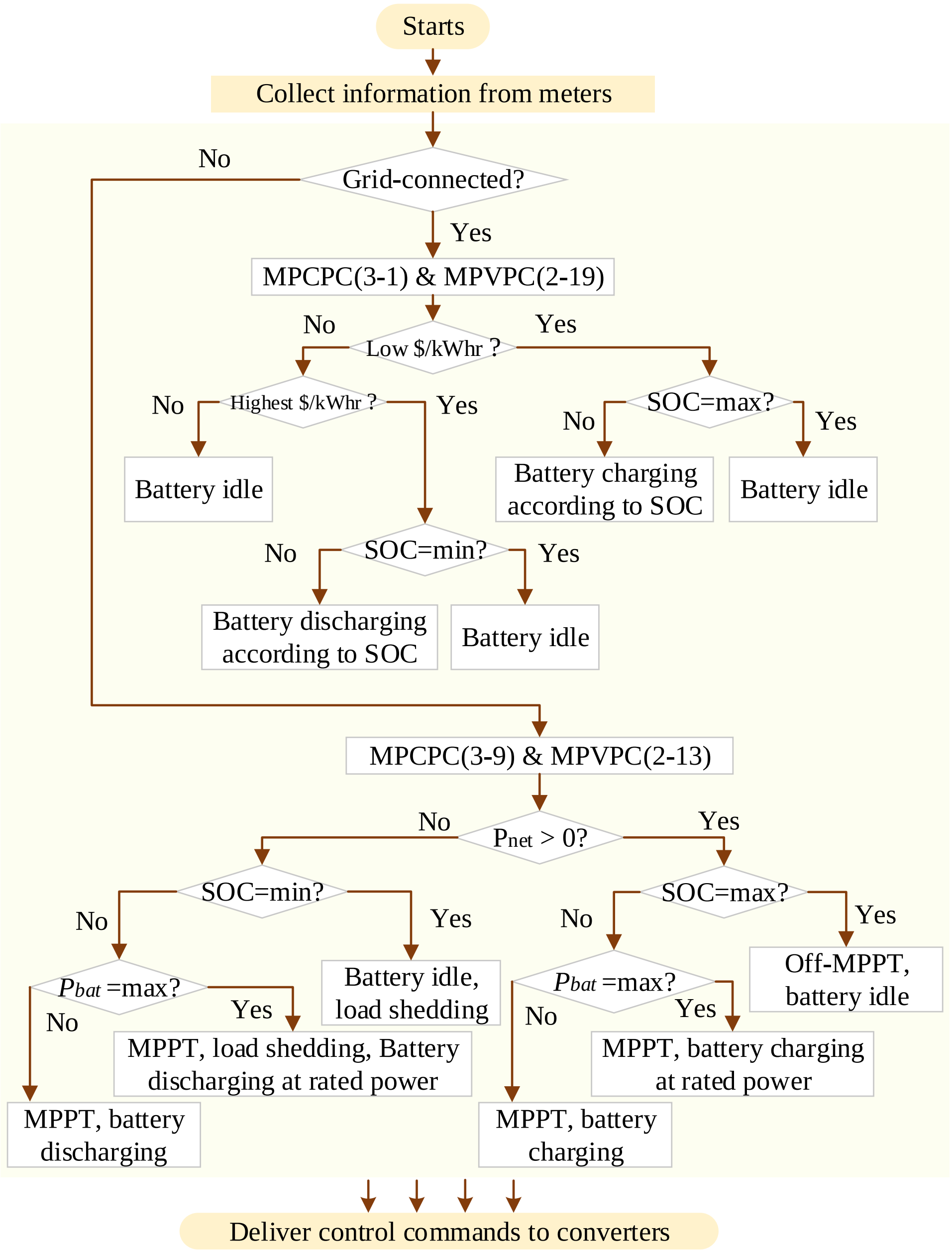

Fig.3-8 System-level EMS

Fig.3-9 depicts the system-level control scheme, which is consistent with the EMS expressed in Fig.3-8, here it will not be repeated.

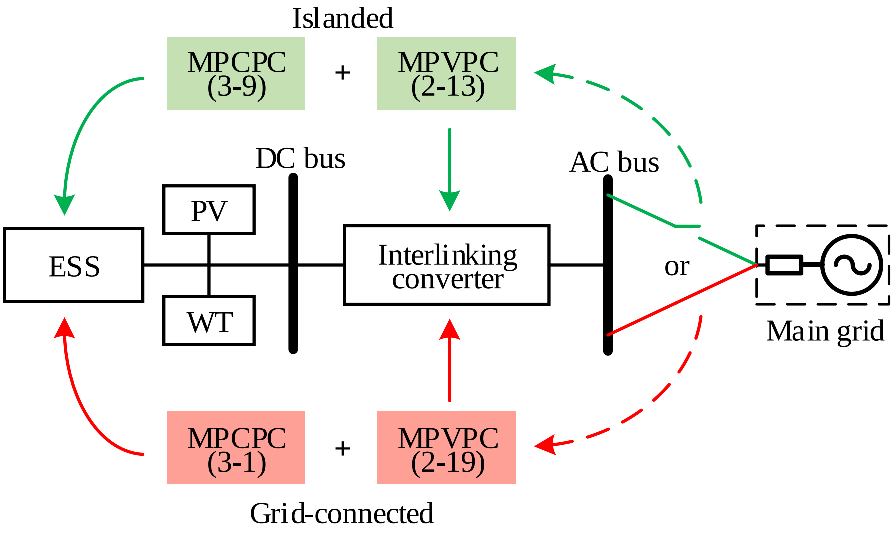

Fig.3-9 System-level control scheme

3.4 Verification

The PV-WT-ESS MG shown in Fig.3-1 is modeled in the Matlab/Simulink platform and various studies are investigated here. Table 3-1 lists the system parameters. Loads 1 and 2 are linear loads while Loads 3 and 4 are nonlinear loads, they are divided into critical and non-critical types. The proposed control schemes (MPCPC&MPVPC) are compared with traditional control schemes where the outer voltage and inner current feedback loops with PI regulators are used. For a fair comparison, the converters' average switching frequencies are kept almost the same. That is, for MPCPC, the switching frequency is around 2kHz in both modes, while for MPVPC, the switching frequency is around 10kHz in grid-connected mode and around 3kHz in islanded mode, respectively.

Table 3-1 System Parameters

Description	**Value**
Solar PV	SunPower Spr-305E-WHT-D, 2.8 MW
WT	Base wind speed 12m/s, R=31m, C_p=0.47
PMSG	1.5 MW, $L_d = L_q$ = 0.3mH, Φ_V = 1.48Wb, p = 48
ESS	Lithium-Ion battery, 1 MW, 300V, 1.3 kA·h, L_{bf} = 50μH
DC-bus voltage	1.2 kV
DC-bus capacitor	20 mF
AC-bus voltage	25 kV / 0.69 kV 60Hz
AC-bus LC filter	L_f = 0.6mH, C_f =1338μF, R_f =1.9mΩ
Linear loads	Critical Load 1 – 1MW, non-critical Load 2 – 0.5MW
Non-linear loads	Critical Load 3 – 1MW, non-critical Load 4 – 0.5MW
PI gains of traditional method	
ESS grid-connected	Current loop: k_p =1.5, k_i =1 (f_{sw} = 2kHz)
ESS islanded	Outer voltage loop: k_p =10, k_i =50 Inner current loop: k_p =5, k_i =2 (f_{sw} = 2kHz)
Interlinking converter grid-connected	Outer voltage loop: k_p =5, k_i =600 Inner current loop: k_p =4, k_i =20 (f_{sw} = 10kHz)
Interlinking converter islanded	Outer voltage loop: k_p =46, k_i =0 Inner current loop: k_p =7, k_i =0 (f_{sw} = 3kHz)

3.4.1 Grid-connected Mode

In this mode, the connected AC distribution network will automatically balance the surplus or deficit power within the MG system. The AC-DC interlinking converter with the MPVPC scheme is used to form a constant-voltage DC bus, delivering the power between DC subgrid and AC subgrid. Since connected to the main grid, the MG system can provide power feeding service, PV and WT systems can provide as much power as possible for the MG and the grid. In addition, the ESS with the MPCPC scheme can be regulated to charge or discharge according to the actual electricity price without the need to shed loads. Generally, if the electricity price is lower than the specified lower limit, the ESS should be charged to store more energy thus to reduce the economic cost. On the contrary, if the electricity price is higher than the specified upper limit, the ESS should discharge to compensate for the system, avoiding extra payment of the expensive electricity bill. Moreover, the charging/discharging rate or the battery current reference is set to be varied with the SOC in a linear relationship located in a band with upper and lower limits, thus to avoid overcharge or overdischarge[116]. For example, a bigger SOC leads to a slower charging rate. Moreover, when the SOC increases to the maximum value, the battery current turns to zero.

As mentioned in Subsection 3.3, the PV and the WT systems both operate with MPPT in grid-connected operation to continuously supply the power to the main grid. The battery is controlled by the actual electricity price, and according to the charging/discharging rate determined by the SOC. Table 3-2 lists a series of events to better demonstrate the effectiveness of the proposed control scheme. The MG starts with Load 1 connected. The solar irradiation is maintained at 600W/m^2, producing about 1.6MW power. The wind speed starts at 12m/s, then steps down to 8m/s at 5s and finally steps up to 10m/s at 15s.

Table 3-2 Events during grid-connected operation

Events	**Operations**	**Time (s)**
1	Wind speed step down	5
2	Load 3 switched in	8
3	Load 2 switched in	11
4	Load 4 switched in	13
5	Wind speed step up	15
6	Load 1 switched off	17

Fig.3-10 shows the performance of using the proposed scheme in the grid-connected mode under different events. I_g is the exchanging current from/to the main grid, I_{grms} is the RMS value of I_g. Before Event 2 happens, except the energy stored in the ESS, excess power is fed to the grid. When Load 3 is switched in (Event 2), the MG begins to absorb power from the grid because the power generated from PV and WT systems is slightly less than the load demand and the ESS capacity. Afterward, when Loads 2 and 4 are all switched in, the MG draws more power from the gird. The AC-side voltage is fixed by the grid, while the DC-side voltage (see Fig.3-10 (i)) is maintained by the AC-DC interlinking converter using the MPVPC scheme. As for the power flow, specifically, the power flows can be bidirectional in grid-connected (see Fig.3-10 (h)), while in islanded operation, the power flows mainly from DC to AC.

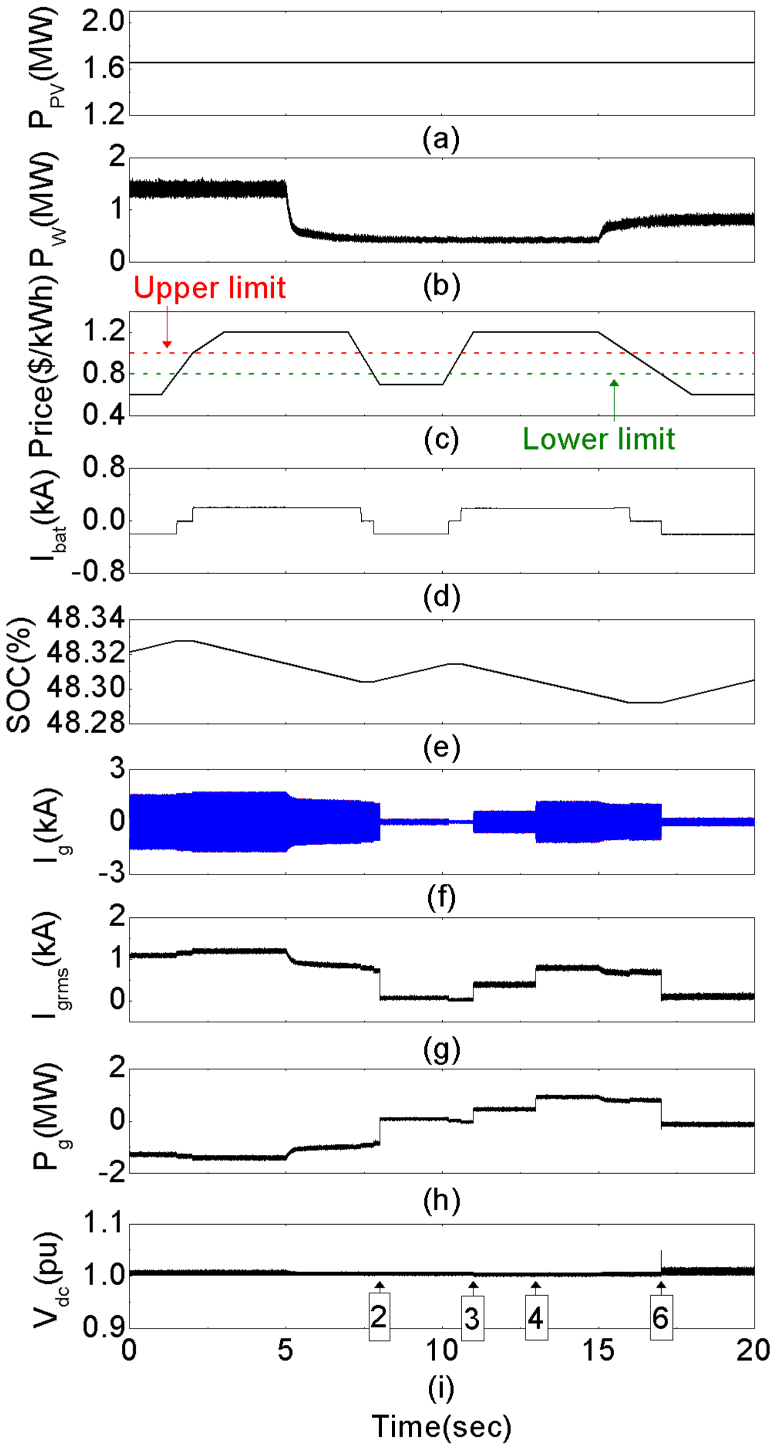

Fig.3-10 Performance of using the proposed scheme in grid-connected mode. (a) PV power, (b) WT power, (c) electricity price, (d) battery current, (e) SOC, (f) the current flowing between the main grid and PV-ESS system, (g) the RMS of I_g, (h) the power flow from/to the main grid, (i) DC-bus voltage.

Fig.3-11 compares the DC-bus voltages using different control schemes. It has shown that, in comparison with the traditional control scheme, the proposed scheme has a stronger controllability of stabilizing the DC voltage in the case of variable generation and consumption.

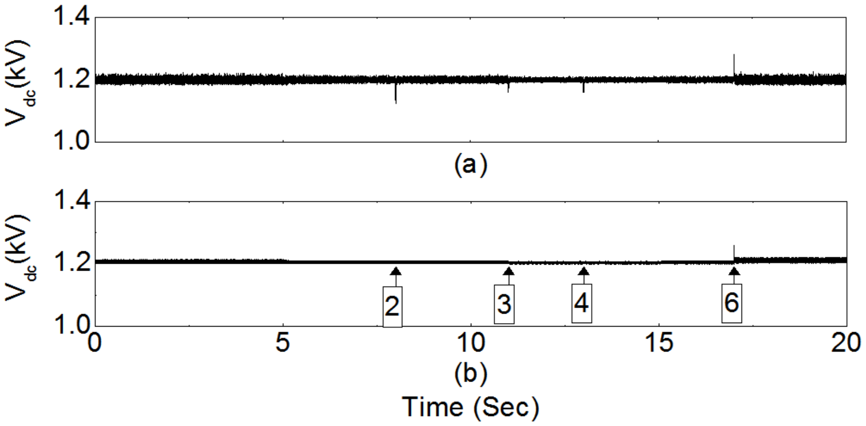

Fig.3-11 Comparison of DC-bus voltages in grid-connected mode.

(a) traditional control scheme, (b) proposed scheme.

3.4.2 Islanded Mode

As for an islanded MG system, its internal power flows need to be balanced, where the DC-bus voltage is maintained by the ESS with the MPCPC scheme rather than by the main grid. Besides, using the MPVPC scheme, the AC-bus voltage is established by the AC-DC interlinking converter. The followings are the two specific situations that need to be respected for this kind of operation.

1) Low wind, low irradiation but heavy load

Low wind and low irradiation result in a low power generation of the RESs, under this situation, the load demand cannot be met. Thus, the PV and WT systems should operate in MPPT, at the same time, the ESS compensates the deficit power by discharging the battery. In order to guarantee a safe power supply to critical loads, load shedding is a necessity if the SOC decreases below the minimum value or the output power rating of the battery is insufficient. For instance, once upon the SOC reaches SOC_{min}, non-critical loads will be switched out firstly. If the SOC still maintains at SOC_{min}, then critical loads will be switched out subsequently. This process also reflects the reason why SOC is included in (3-1) and (3-9).

2) High wind, high irradiation but light load

At this time, due to the high wind and high irradiation but the light load, the generation from RESs will be more than the load demand. Excessive powers can be absorbed by the ESS, however, if they exceed the battery capacity or the SOC is maximal, off-MPPT should be activated on the RESs, like the PV and WT systems.

By comparison, the islanded mode is more challenging than the grid-connected mode, since the bulky main grid is unavailable. By using the proposed MPC-based schemes and according to the designed EMS, stable operation and high-quality power supply are both achieved. In the following test, the wind speed keeps at 10m/s, while the solar irradiation is varied. Similarly, a series of events is set here, as listed in Table 3-3. Load 3 (1MW non-linear load) is connected to the AC bus initially.

Table 3-3 Events during islanded operation

Events	**Operations**	**Time (s)**
1	Solar irradiation ramps up	5
2	Load 1 switched in	9
3	Solar irradiation ramps down	11
4	Load 2 and 4 switched in	11
5	Load 4 switched out (load shedding)	12

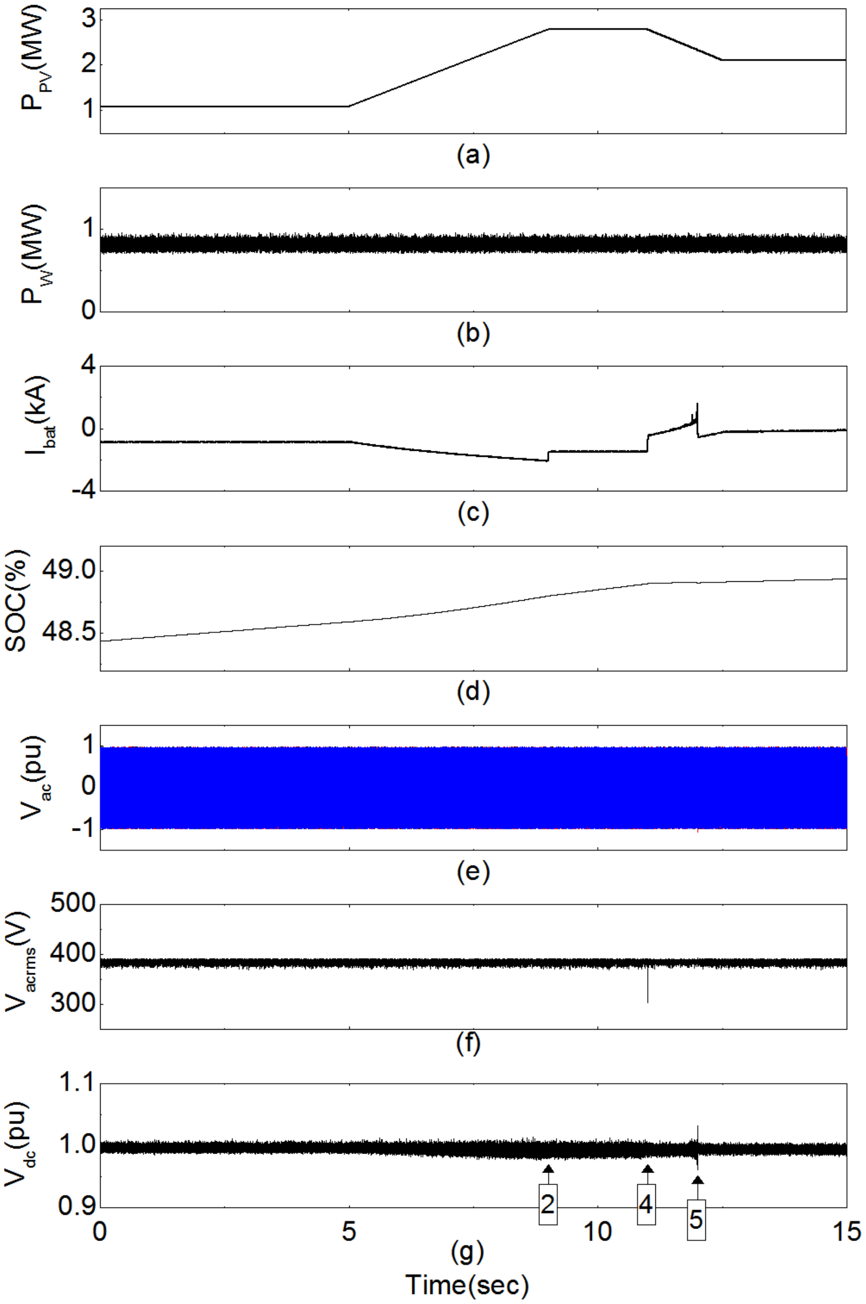

Fig.3-12 Islanded performance under variable PV power and load demand condition using the proposed scheme. (a) PV power, (b) WT power, (c) battery current, (d) SOC, (e) AC bus voltage, (f) the RMS of V_{ac}, (g) DC-bus voltage.

Fig.3-12 shows the islanded performance under variable PV power and load demand conditions using the proposed scheme. V_{acrms} is the RMS value of the AC bus voltage V_{ac}. Before Events 3 and 4, the generation from RESs can meet the load demand adequately. Whereas, at 11s, Loads 2 and 4 are suddenly switched in and the PV output drops simultaneously, leading to a discharging process of the ESS to compensate the energy gap. PV output power gradually decreases, while the ESS output accordingly increases until it approximates to the rated current at around 12s. In due course, the load shedding is activated to switch out the non-critical Load 4.

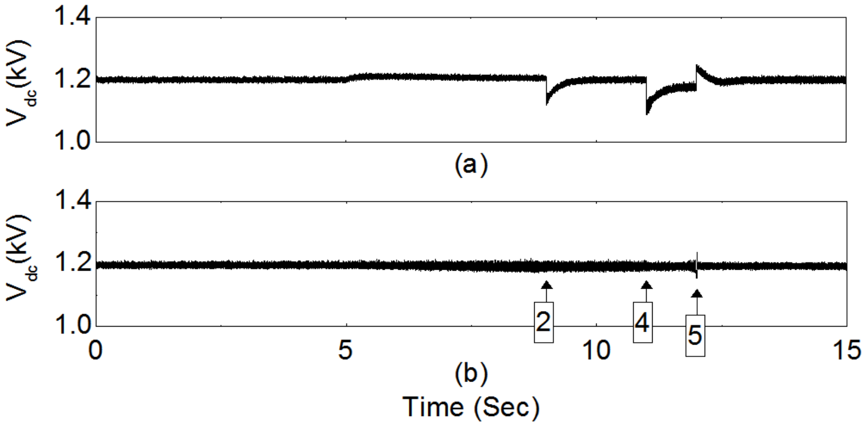

Fig.3-13 Comparison of DC-bus voltages in islanded mode. (a) traditional control scheme, (b) proposed scheme

As for the islanded mode, the quality of DC and AC voltage supply is an important index to evaluate the control performance. Enlarged waveforms of DC bus and AC bus voltage using the proposed schemes are plotted in Fig.3-13(b) and Fig.3-14(b) respectively. The comparison test is also performed, the results are presented in Fig.3-13(a) and Fig.3-14(a), it can be seen that the DC-bus voltage under traditional PI control scheme presents obvious oscillations when load changes, however, the proposed scheme presents a better controllability over the DC-bus voltage where the oscillations are well suppressed. On the AC side, the proposed scheme also exhibits better voltage quality. As shown in Fig.3-14(b), with the proposed scheme, the AC voltage is more sinusoidal with only 1.05% THD, while it is 3.20% with the traditional PI control scheme (see Fig.3-14(a)).

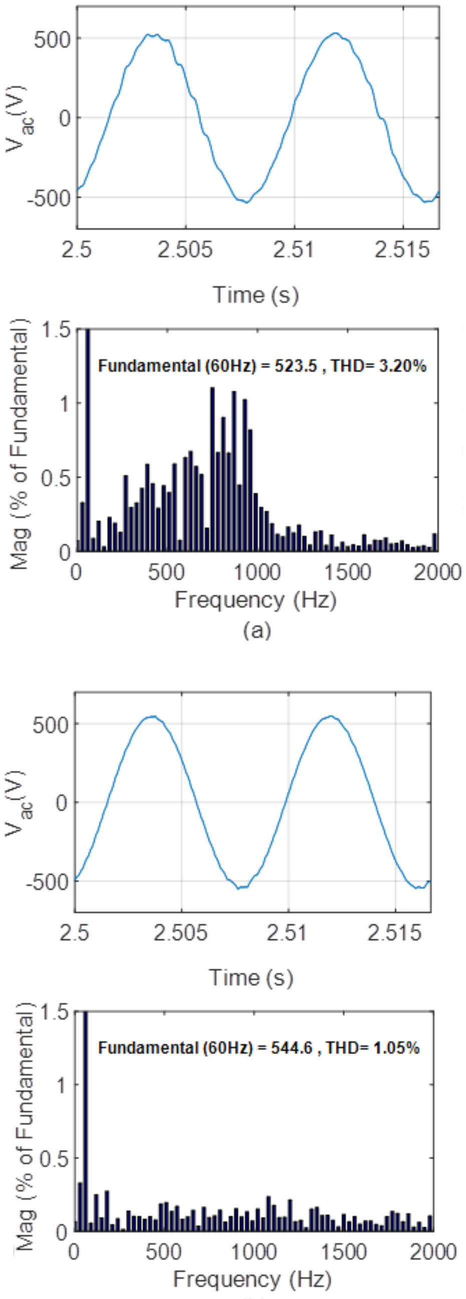

(a)

(b)

Fig.3-14 Comparison of AC-bus voltages in islanded mode. (a) traditional control scheme, (b) proposed scheme.

3.4.3 Grid Synchronization

This subsection explores the performance of grid synchronization. When an islanded MG is intended to connect the main grid, the grid synchronization is necessary where the AC terminal voltage begins to track the grid voltage. Once two-sided voltages are in phase and magnitudes are matched, the grid connection is realized. To some extent, this synchronization is an extension of islanded mode. Similarly, the DC bus is dependent on the ESS and the AC bus is maintained by the interlinking converter from the DC side.

The frequency and voltage magnitude of the main grid are continuously detected by the PLL and serve as the terminal references for the synchronization control. Before the synchronization, a voltage with the same magnitude as the grid voltage, and a slightly lower than the grid but gradually increasing frequency are set as the voltage reference for the cost function (2-13). In this process, once the phase error on both sides reaches zero, the grid connection is realized. Here, the PLL is used as a tool to test the grid synchronizing process of proposed control, its stability and parameter design are therefore not fully investigated.

It is seldom to find existing researches mention grid synchronization and connection of hybrid MGs, but which will be studied here. Fig.3-15 shows relevant detailed results by using the proposed method. Initially, the MG system operates in islanded mode. The grid synchronization starts at 0.25s then the MG system is connected to the main grid at 1s. It is observed that the AC voltage V_{ac} tracks the main grid voltage V_g in a relatively short time. Also, no major current overshoots exist.

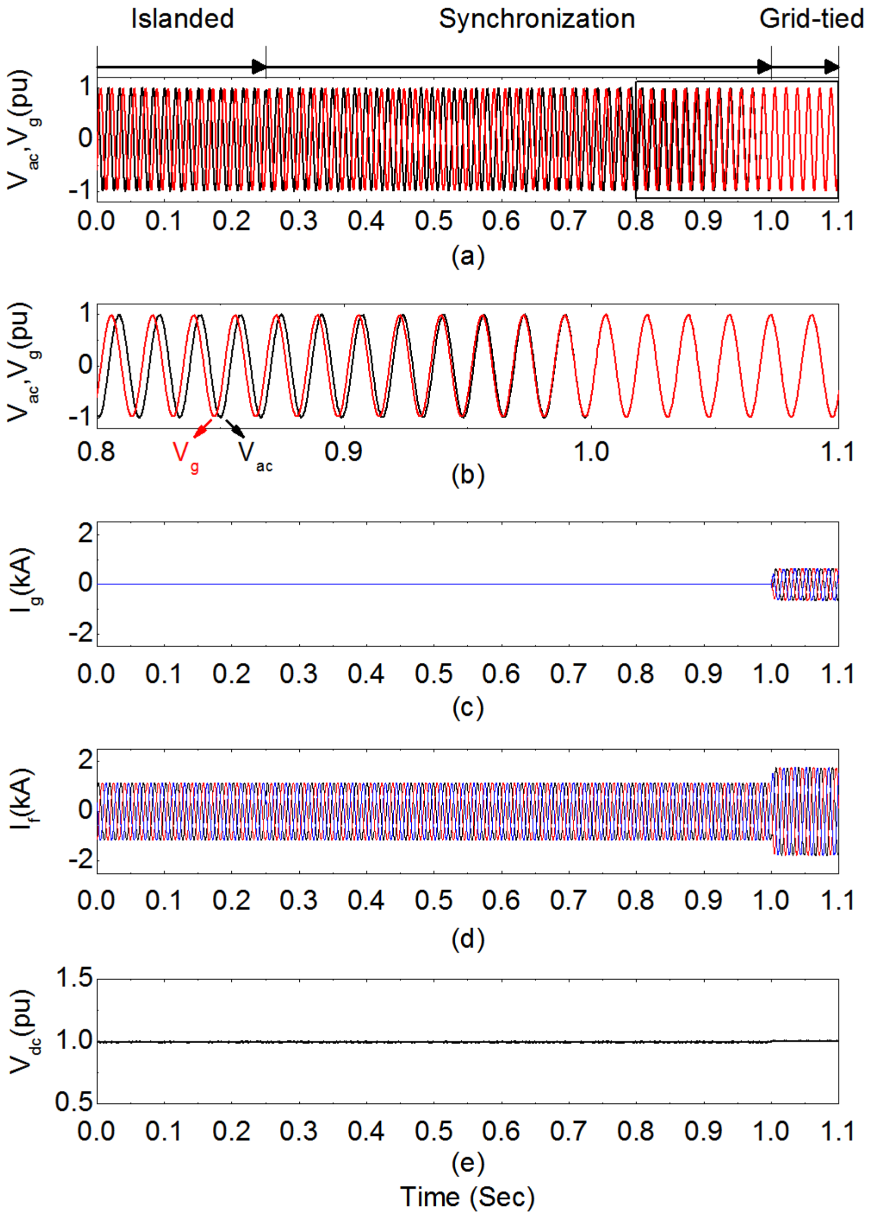

Fig.3-15 System performance of the grid synchronization and connection using the proposed scheme. (a) AC voltage and the main grid voltage, (b) enlarged view of partial (a), (c) the current flowing between the main grid and PV-ESS system, (d) inductor current, (e) DC-bus voltage.

3.4.4 Real-time Data Test

To further validate the proposed scheme from a practical viewpoint, a set of real-time data about solar irradiation and wind speed on Hong Kong Lamma Island are utilized[117]. The output powers of the PV and WT systems are plotted in Fig.3-16 (a) and (b). Applying the events listed in Table 3-3, the MG performance using the proposed scheme in the islanded mode under real-world fluctuating power generation and consumption is presented in Fig.3-16.

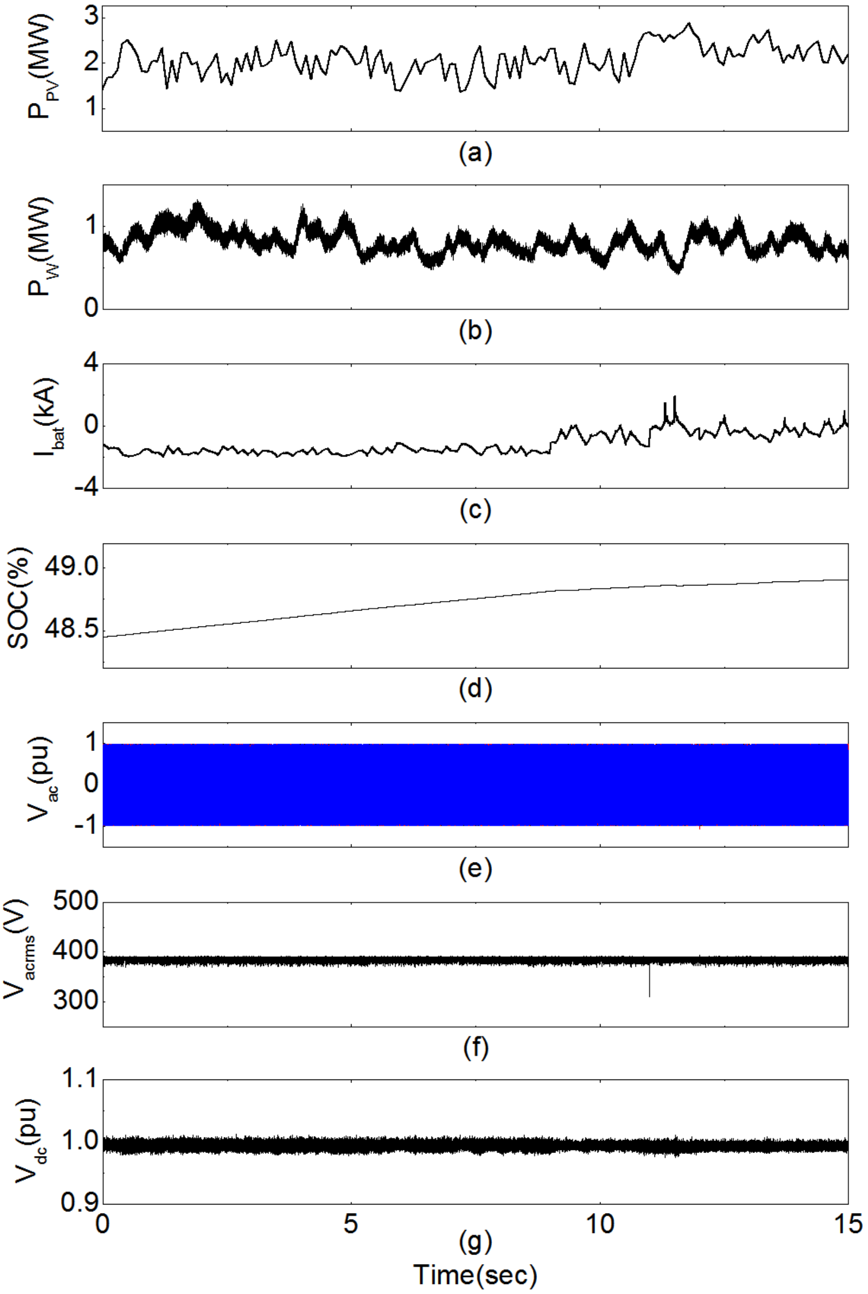

Fig.3-16 System performance under the real-world solar irradiation and wind speed using the proposed scheme. (a) PV power, (b) WT power, (c) battery current, (d) SOC, (e) AC bus voltage, (f) the RMS of V_{ac}, (g) DC-bus voltage.

As shown, during the whole process, the battery charges or discharges duly and properly to coordinate the generation and consumption, which can be seen from the battery current I_{bat} and the SOC curves. The DC bus is well maintained by the ESS using the MPCPC scheme, while a stable AC bus is fixed by the AC-DC interlinking converter using the MPVPC scheme.

3.5 Summary

In this section, the MPC-based control schemes applied to an MG system with PV-WT-ESS sources are proposed. The MPCPC scheme concerning current and power is designed to control the bidirectional DC-DC converter of the ESS, while the MPVPC scheme concerning voltage and power is developed to control the AC-DC interlinking converter. The two schemes are collectively utilized to regulate the DC-DC and AC-DC converters to smooth the RESs' outputs and support DC and AC buses. From the viewpoint of the system level, a comprehensive EMS is developed to allow the system to have a smooth running under various operation modes. The validity and effectiveness of the proposed scheme are verified by a PV-WT-ESS MG system involving real-world solar irradiation and wind profiles. Besides, the proposed schemes also present the better control effect and improved voltage quality in contrast with traditional PI control schemes based on the CLC. However, it should be stated that the proposed scheme needs more measurements in comparison with traditional schemes, which results in several additional probes and communication links scattered in the RES-ESS system and around the AC-DC interlinking converter.

Chapter 4 MPC for PV-ESS MGs with Voltage Support Capability

So far, the rapidly increasing installation and penetration of PV systems in the main-grid distribution network have caused a critical problem, i.e. the voltage rise/drop, which negatively impacts the grid supplying quality and security. Under such circumstances, a flexible power regulation with potential ancillary services is especially needful for PV inverters. In this chapter, as for a grid-connected MG which has PV and ESS systems, an MPPC scheme is proposed to collaboratively regulate the DC-DC converter and inverter (VSC based). By using this MPPC scheme to regulate the DC-bus voltage and control the active and reactive power flows, the main grid is supported to maintain a stable voltage and frequency with an improved power factor. The effectiveness of the proposed scheme has been validated through numerous simulation studies and controller-hardware-in-the-loop (CHIL) tests.

4.1 Background and System Configuration

The PV-ESS MG system studied here is shown in Fig.4-1. It is a hybrid MG, where the DC bus is formed by the connection of a PV system with a boost converter and an ESS system with a bidirectional DC-DC converter. The AC bus is formed by the inverter and the main grid. In grid-connected MG systems, as aforementioned, the power distribution control is the main focus. From this point, the DC-side power can be selected as the control objective for the bidirectional DC-DC converter. On the other hand, the AC-side active and reactive power flows can be chosen as the control objectives of the inverter. In this MG, the power flows obey the rules made and issued by the power management scheme based on the communication links as shown in Fig.4-1.

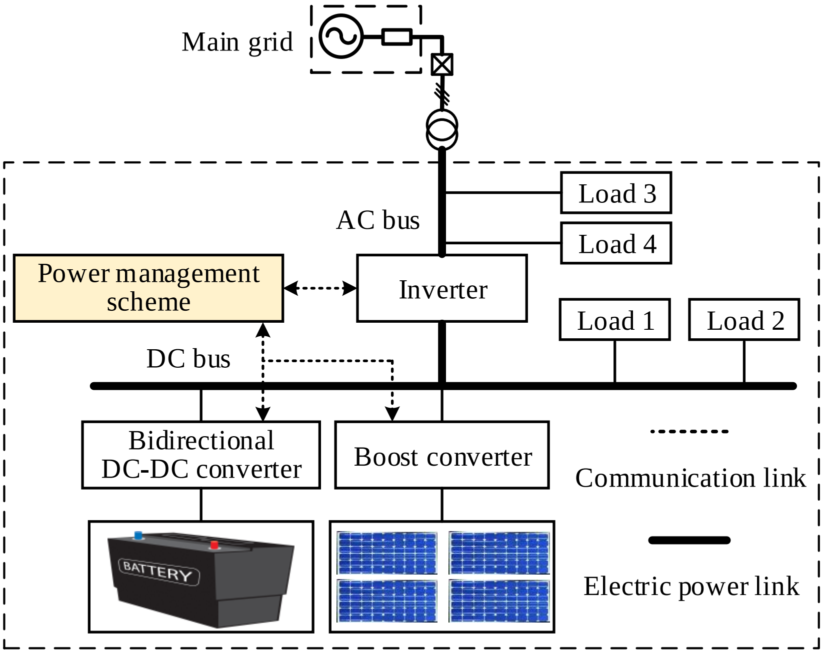

Fig.4-1 Configuration of the PV-ESS system

Conventionally, the DC-bus voltage is maintained through the inverter in a grid-connected PV system, and the bidirectional DC-DC converter in the ESS is used to control the charging/discharging current to/from the battery thus to smooth the PV output. This control structure limits the flexible power regulation capability of the PV-ESS system because the active and reactive power flows between the PV-ESS system and the main grid cannot be controlled directly and flexibly. The question has now become whether it is possible to maintain the DC-bus voltage by controlling the DC-DC bidirectional converter rather than the inverter so that the control freedom of the inverter on the bidirectional active and reactive power flows can be fully explored. In this section, a positive answer to this question is given and analysed[118].

4.2 MPPC Scheme

The proposed MPPC scheme for the ESS can smooth the fluctuating outputs from the PV and maintain the stability of DC-bus voltage, simultaneously the proposed MPPC scheme for the inverter can flexibly regulate the power exchange between the MG and the main grid. With this scheme, the PV-ESS MG can also support the grid through compensating the AC-bus voltage to a certain extent.

1) Control of Bidirectional DC-DC Converters

Fig.4-2 shows the configuration of the ESS, where a DC-DC converter interfaces a battery (connected to the LV-side port) and the DC bus (connected to the HV-side port). The equivalent circuits of boost and buck modes and their operating principles are analysed in Subsection 2.1.1. The battery is charged with absorbing the energy from the DC bus and discharged with releasing the energy to the DC bus.

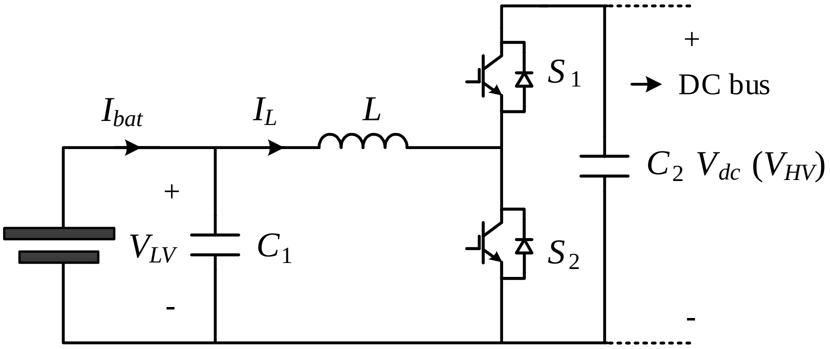

Fig.4-2 Configuration of the ESS system

The principle of MPPC applied to this ESS system is similar to the islanded-mode MPCPC in the Subsection 3.2.1, the difference is that the RES here is just a PV system, and the islanded-mode MPCPC is used to a grid-connected system here. The control diagram of the MPPC scheme applied to the DC-DC bidirectional converter is shown in Fig.4-3. Predictive model (2-

4) and (3-8) utilize the measurements from the circuit to produce a predictive target variable at the next instant, at the same time, a power reference is designed based on the measurements and calculations. Then the cost function (3-9) relied on these predictive variables and the designed reference is used to generate control signals to switch the converter.

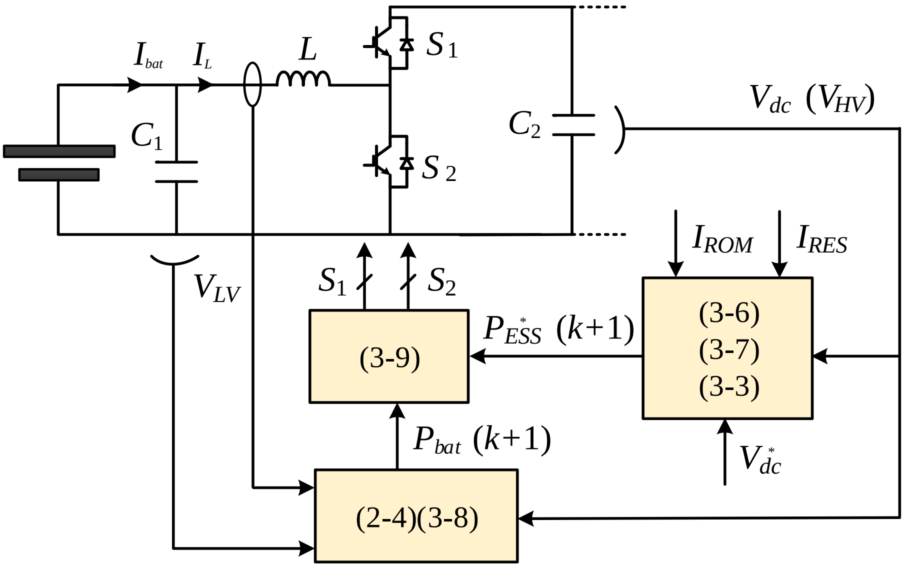

Fig.4-3 Control diagram of the MPPC scheme applied to the bidirectional DC-DC converter

2) Control of Grid-Connected Inverters

Once the DC bus is regulated by the ESS, the grid-connected inverter can now be allowed to be equipped with more control abilities with ancillary services. One of the typical services is to provide flexible bidirectional power flows and associated voltage support. The grid-connected inverter used here is based on the VSC, its connection to the grid is depicted in Fig.4-4.

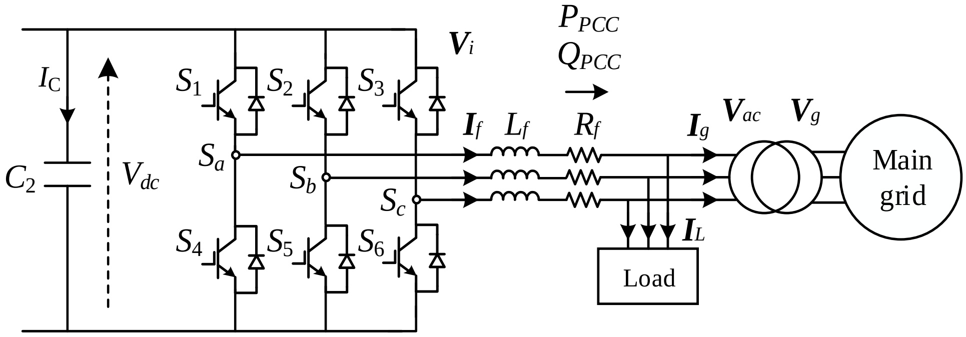

Fig.4-4 Inverter configuration

The VSC dynamics in the grid-connected system are discussed in Subsection 2.2.3. The predictive model is expressed in (2-18), while the cost function is presented in (2-19). The control diagram of the MPPC scheme applied to the inverter is shown in Fig.4-5. In this section, the power references are given by the voltage support, and through which to provide an AC-bus voltage supporting service.

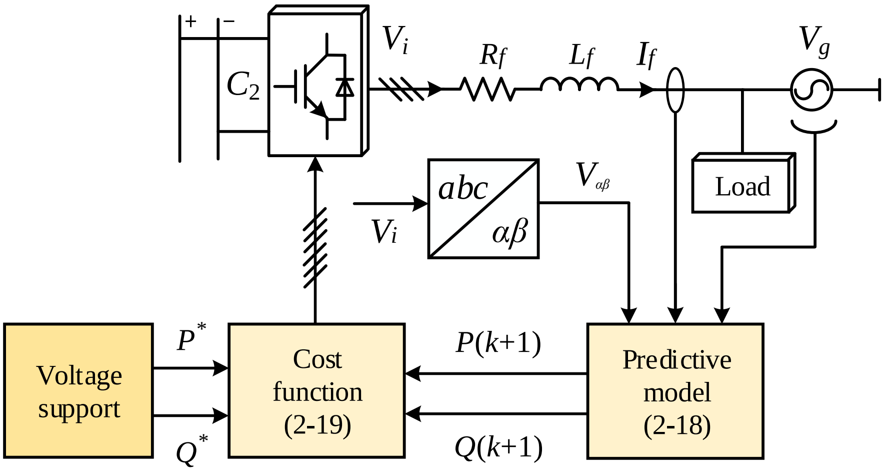

Fig.4-5 Control diagram of the MPPC scheme applied to the inverter

4.3 Voltage Support

The proposed MPPC scheme provides a flexible control for the active power P and reactive power Q. With this in mind, a further question comes to how to take advantage of this control freedom of power regulation thus to design the power references. Traditionally, the power is transmitted unidirectionally from the upstream HV to the downstream LV to supply loads in the transmission and distribution systems. Generally, in order to address the voltage deviations resulted from the load change and the reverse power inrush from the PV and ESS, the transformer with an automatic tapping action which can realize the voltage regulation is usually used[119]. However, frequently taking this tapping action will shorten the facility lifespan and increase the requirement of maintenance. An alternative simple way is to modify the PV system or operate it in a decentralized manner. That is, to utilize the PV inverter's capability of flexible *P* and *Q* regulation to address the voltage regulation issue.

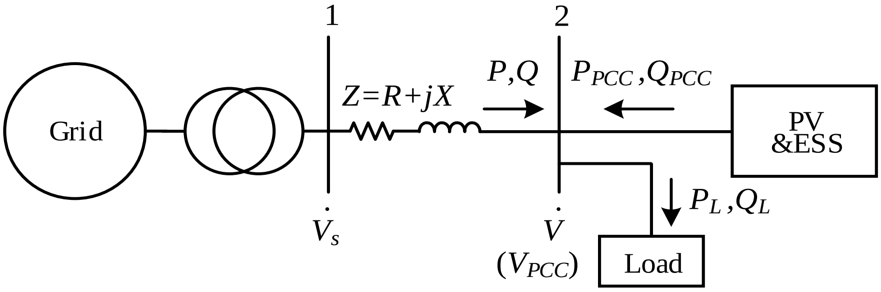

Fig.4-6 Power flows of the MG

Fig.4-6 shows the power flows inside the MG, in which Bus 1 is the front-end distribution feeder with voltage $\dot{V}_s$, Bus 2 is the AC bus (i.e. the PCC) of the MG with voltage $\dot{V}$. The feeder line impedance is $Z=R+jX$ with the resistance *R* and reactance *X*. *P* and *Q*, P_{PCC} and Q_{PCC}, and P_L and Q_L are the active and reactive powers from the main grid, the PV-ESS system, and the load, respectively. Their positive directions are denoted in Fig.4-6. When Q_{PCC} is positive, the PV-ESS system outputs inductive reactive power, while negative, it outputs capacitive reactive power. In the same way, when P_{PCC} is positive, the PV-ESS system exports active power, while negative, it imports active power.

The voltage drop across Bus 1 to Bus 2 is calculated by

$$\Delta\dot{V} = \frac{RP + XQ}{\dot{V}} + j\frac{XP - RQ}{\dot{V}} \tag{4-1}$$

where the active and reactive powers are

$$P = P_L - P_{PCC} \tag{4-2}$$

$$Q = Q_L - Q_{PCC} \tag{4-3}$$

In the case of a high *R*/*X* ratio, the voltage drop approximates to the real part of (4-1) as[120]

$$V = V_s - \frac{R(P_L - P_{PCC}) + X(Q_L - Q_{PCC})}{V_{PCC}} \tag{4-4}$$

As shown in Fig.4-6, Bus 2 voltage changes with the load varies. Particularly, when there is a significant load change, the voltage will significantly drop, once falling below the lower limit, the system security will be damaged. This results in a necessity to regulate the voltage, i.e. through controlling both the active and reactive power flows to support the voltage. This method detects the Bus 2 voltage in real time. If there is a voltage drop due to the load changes, the deviation will be captured, then the power errors (ΔP and ΔQ) are used to replace the power references (P^* and Q^*). This process is realized by

$$\Delta P = P^* = \left(V_{t+1} - V_{t-1}\right) \times 100\% \times m_W \tag{4-5}$$

$$\Delta Q = Q^* = \left(V_{t+1} - V_{t-1}\right) \times 100\% \times m_{Var} \tag{4-6}$$

where the subscripts t+1 and t-1 are the load changes at one sampling time earlier and later than the current instant, m_W and m_{Var} are the coefficients of P and Q, respectively.

In this way, the MG can provide active and reactive power compensation on the basis of the detected PCC voltage variations. Note that, (4-5) and (4-6) are the simple examples to provide potential grid support from the PV-ESS system. It is promising to see, in the future smart grid, an accurate amount of reactive power supplied by each MG in the MG clusters with high RES capacities will be determined by involving comprehensive factors like load property, feeder line *R*/*X*, and reactive capability, etc.

The ΔP and ΔQ determined by (4-5) and (4-6) are then delivered to the core processor as the references P^* and Q^*, as indicated in Fig.4-5. With a fast dynamic property of the MPPC control algorithm, once the detection of the voltage drop is completed, the quantities of the references can be determined and sent into the grid, thus to compensate the voltage. Note that the grid-connected inverter associated with the PV-ESS system is not an infinite power source or a power sink, inversely their values are bounded by the rated apparent power (see Fig.4-7).

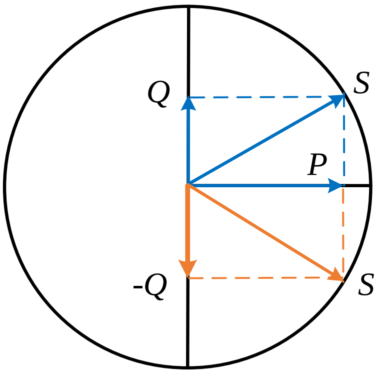

Fig.4-7 PV inverter capability model

The range of allowable active power is limited as

$$P \leq P_{ESS\_\max} + P_{PV\_mpp} \tag{4-7}$$

where P_{ESS_max} is the rated ESS power, P_{PV_mpp} is the output maximum power of the PV system. If the actual active power is obtained, the variation region of allowable reactive power can also be determined by

$$|Q| \leq \sqrt{S^2 - P^2} \tag{4-8}$$

4.4 Verification

The PV-ESS system depicted in Fig.4-1 is constructed and the MPPC scheme is investigated in the Matlab/Simulink environment. The DC-DC converter and equipped MPPT technique in the PV system are set according to Subsection 2.3.1. In this section, the validity of the proposed MPPC scheme has been proven by numerical simulation cases. The system parameters are listed in Table 4-1.

Table 4-1 System Parameters

Description	**Value**
Solar PV	SunPower Spr-305E-WHT-D, 2.5MW (STC)
ESS	Lithium-Ion battery, 300V, 2.3kAh, SOC_{max} = 90%, SOC_{min} = 10%, I_{bat_rated} = 3.5kA
DC-bus voltage	1.0kV
DC-bus capacitor	C_2 = 50mF
DC-side inductor	L = 0.17mH
AC-bus voltage	0.69kV (p-p), 60Hz
Transformer	25kV / 0.69kV (p-p), 60Hz
AC-bus LC filter	L_f = 0.6mH, R_f = 1.9mΩ
Linear loads	Critical Load 1: 0.5MW, non-critical Load 2: 1MW
Non-linear loads	Critical Load 3: 0.5MW, non-critical Load 4: 1MW
Voltage support	$m_W = -2.368\times10^5$, $m_{Var} = -1.259\times10^4$
PI gains of traditional method	
ESS	Current loop: $k_p = 1.8$, $k_i = 1.1$; Voltage loop: $k_p = 12.3$, $k_i = 37.2$ (f_{sw} = 3kHz)
Comparison MPC	$k_p = 9$, $k_i = 122$

Here, the traditional control scheme of double loops (outer voltage & inner current) based on PI regulators is set as a comparable group to the proposed MPPC scheme. For a fair reason, the two schemes are compared with the same average switching frequencies of the converters. The 20kHz sampling frequency of both schemes results in a 3kHz switching frequency of the DC-DC converter and a 3.8kHz switching frequency of the DC-AC converter, respectively. Sampling frequency indicates the acquired number of data points per time unit, while the switching frequency means the rate at which the power converter can complete an action. Their frequencies are different and usually sampling frequency is higher than switching frequency.

The discharging process of the ESS is defined as a positive direction. P_{PCC} and Q_{PCC} are the active and reactive power flows between the PV-ESS system and the main grid, the positive direction is defined as the flow from the main grid to the PV-ESS system. The battery capacity for the voltage support is decided by the system EMS. Generally speaking, smaller capacity provides smaller support.

4.4.1 Variable Loads

In this study, the efficiency of the proposed MPPC scheme to deal with variable loads is verified. Power references P^* and Q^* are fixed at 0.8MW and 0Mvar respectively. The solar irradiation and temperature are set at 600W/m^2 and 25℃ respectively, producing about a total of 1.5MW power. The system starts with Load 3 (0.5MW AC load) connected. Load 1 (0.5MW DC load) is connected at 1s. Load 2 (1MW DC load) is connected at 2s and then disconnected at 3s.

Fig.4-8 shows the system performance of the proposed MPPC under variable loads, with the PV output maintained around 1.5MW by using MPPT (see Fig.4-8(a)). The actual active and reactive power flowing through the

PCC can follow tightly at their references (see Fig.4-8 (b) and (c)). The load demand is met by the combination of the main grid and the PV system, while the surplus energy is absorbed by the ESS (see Fig.4-8(d)). When the load demand increases at 1s and 2s, the charging currents decreases accordingly (see Fig.4-8(e)). In this process, the SOC keeps increasing since the load demand is smaller than the total power generation provided by both the main grid and the PV system (see Fig.4-8(f)). The current passing through the PCC shows no more changes under an approximatively fixed active and reactive power (see Fig.4-8(g)). The DC-bus voltage is held constant around the rated setpoint (see Fig.4-8(h)).

Fig.4-9 depicts the comparison of DC-bus voltages using the proposed scheme and traditional control scheme with the same power generation and load consumption. The proposed MPPC scheme shows a stronger controllability to stabilize the DC voltage compared with the traditional PI control. Under the same condition of tracking a constant active power, traditional control scheme presents an inferior performance, this is because the PI-based scheme can not support the grid voltage via directly setting the active power reference, inversely it has to keep the DC-bus voltage stable by using the inverter in the grid-connected mode. In clear contrast to the traditional control scheme, the proposed MPPC scheme can well maintain the DC-bus voltage stable and robust through regulating the DC-DC converter, simultaneously the inverter can then be released, to a certain degree, to control the power flows.

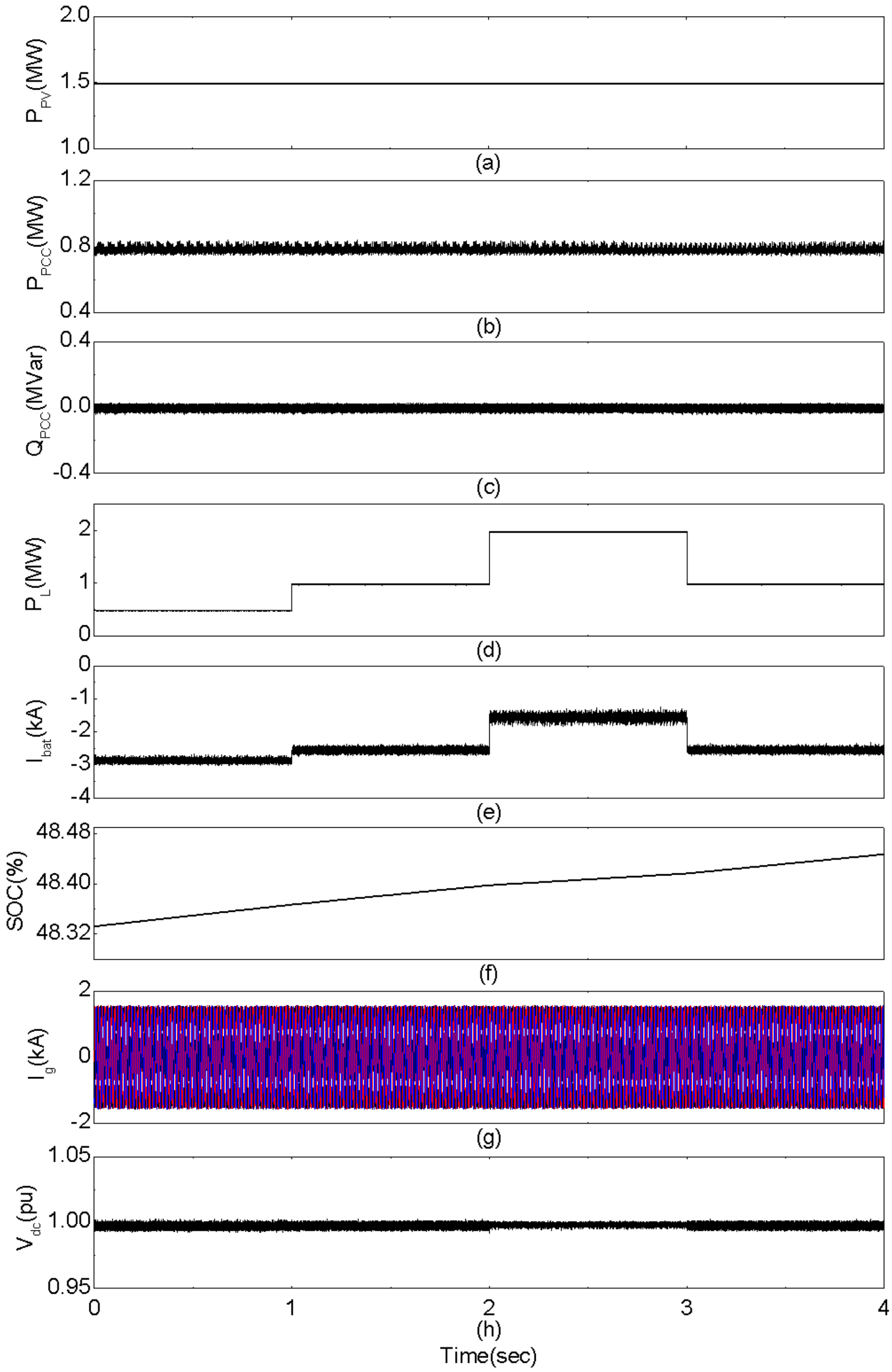

Fig.4-8 Performance of the MPPC scheme for DC-DC bidirectional converter under variable loads. (a) PV power, (b) active power at PCC, (c) reactive power at PCC, (d) load power, (e) battery current, (f) SOC, (g) the current flowing between the main grid and PV-ESS system, (h) DC-bus voltage.

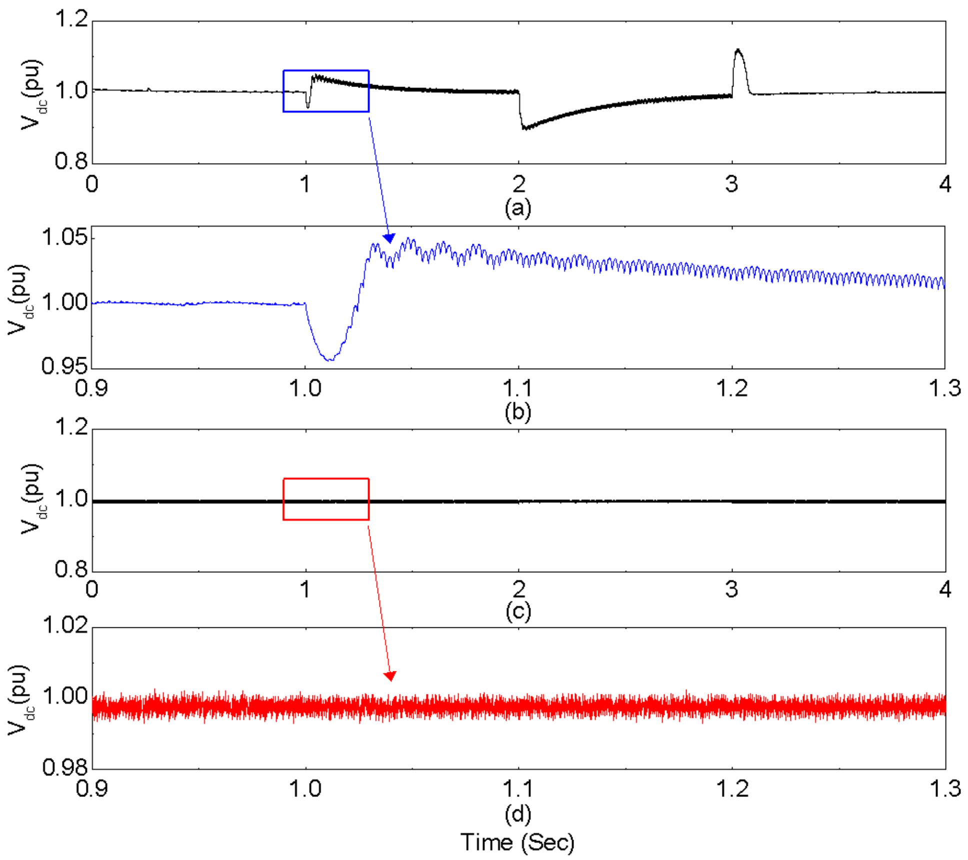

Fig.4-9 Comparison of DC-bus voltages. (a)&(b) traditional control scheme, (c)&(d) proposed scheme.

4.4.2 Fluctuant PV Input

Since the RES system is highly dependent on the weather condition, in order to test and verify the proposed MPPC scheme, real-world fluctuating solar irradiation and ambient temperature are applied. A most severe scenario of the PV output compressed into one-day time is shown in Fig.4-10(a). The power references are respectively set as P^{*}= -0.5MW and Q^{*}= 0Mvar. A series of load changes is set: Load 3 (0.5MW AC load) is initially connected to the PCC; at 1s, Load 1 (0.5MW DC load) is connected; at 3s, Load 2 (1MW DC load) is connected and then disconnected at 5s; while at 5s, Load 4 (1MW AC load) is also connected, and then disconnected at 7s.

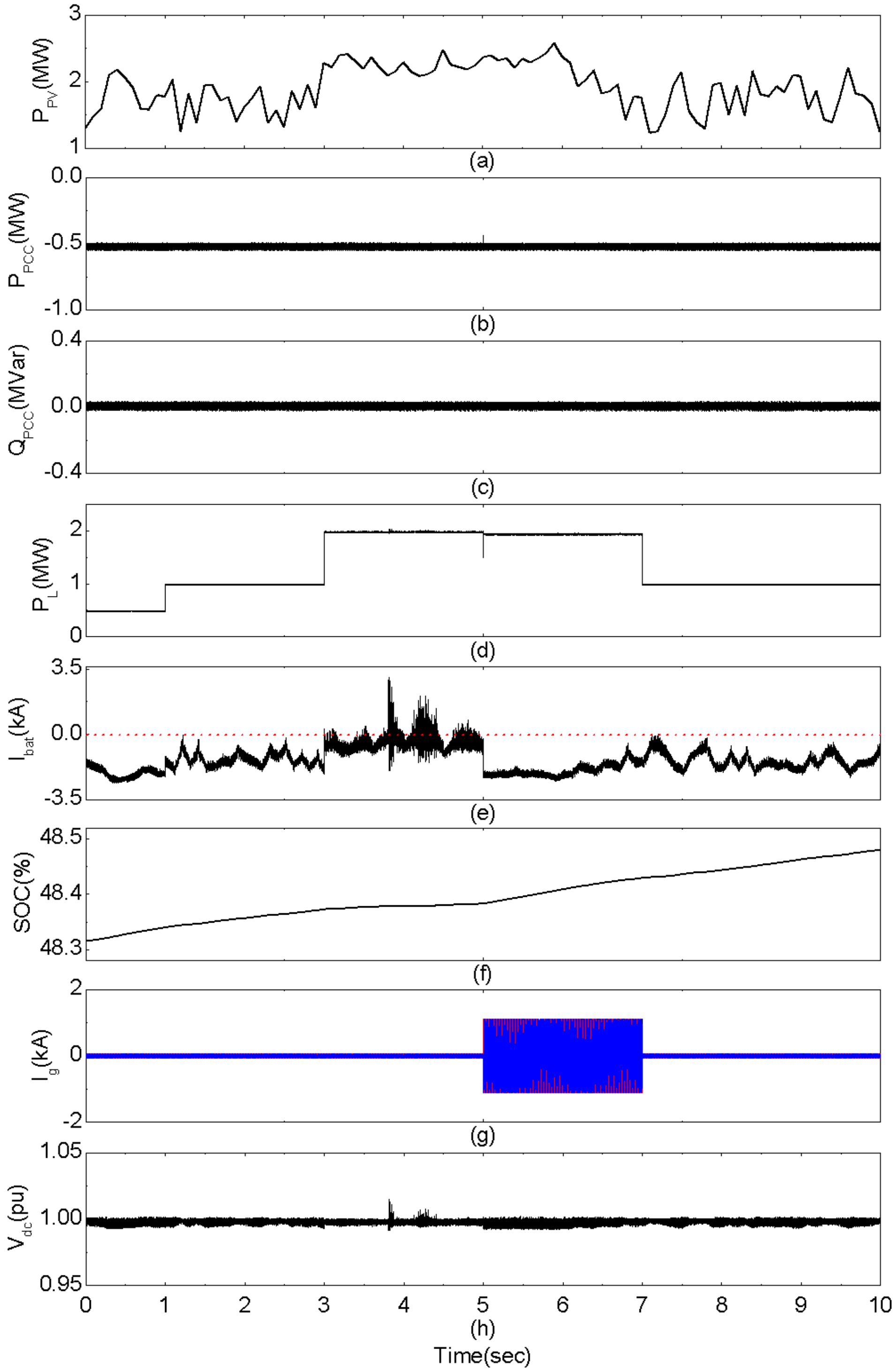

Fig.4-10 Performance under the real-world fluctuant PV output using the proposed scheme. (a) PV power, (b) active power at PCC, (c) reactive power at PCC, (d) load power, (e) battery current, (f) SOC, (g) the current flowing between the main grid and PV-ESS system, (h) DC-bus voltage.

As shown in Fig.4-10 (b) and (c), the actual tracking results at the PCC are kept consistent with the power references. The fluctuating PV outputs are mainly absorbed by the ESS in both the initial and the last 3 seconds, keeping the net power output from DC bus to the PCC continuously around 0.5MW (see Fig.4-10(b)), during these periods, the DC-bus voltage maintains stable and smooth (see Fig.4-10(h)). The load power varies as shown in Fig.4-10(d). From 3s to 5s, the DC load power is larger than PV generation, the ESS has to be discharged to maintain a stable-voltage DC bus (see Fig.4-10(e)). There exists a DC-bus voltage overshoot at about 3.8s, however, it rapidly restores its stability. From 5s to 7s, the current passing through the PCC sees a steep rise due to the connection of an AC load (see Fig.4-10(g)). Fig.4-10(f) shows the SOC information during the whole process.

4.4.3 Flexible Power Tracking

Using the proposed MPPC scheme to dynamically track the power references is depicted in Fig.4-11, where the solar irradiation and temperature are respectively set to 600W/m^2 and 25℃, resulting in about 1.5MW output power. Initially, Load 3 (0.5MW AC load) is connected to the PCC. From 0s to 5s, Q^* keeps at 0Mvar, P^* is set to 0.2MW during 0s to 1s, then, P^* varies to 0.7MW at 1s, -0.4MW at 2s, -0.7MW at 3s, 0.8MW at 4s and keeps unchanged afterward. Next, from 5s to 10s, Q^* changes to -0.02Mvar at 5s, 0.1Mvar at 6s, 0.4Mvar at 7s, -0.01Mvar at 8s, and lastly 0.3Mvar at 9s.

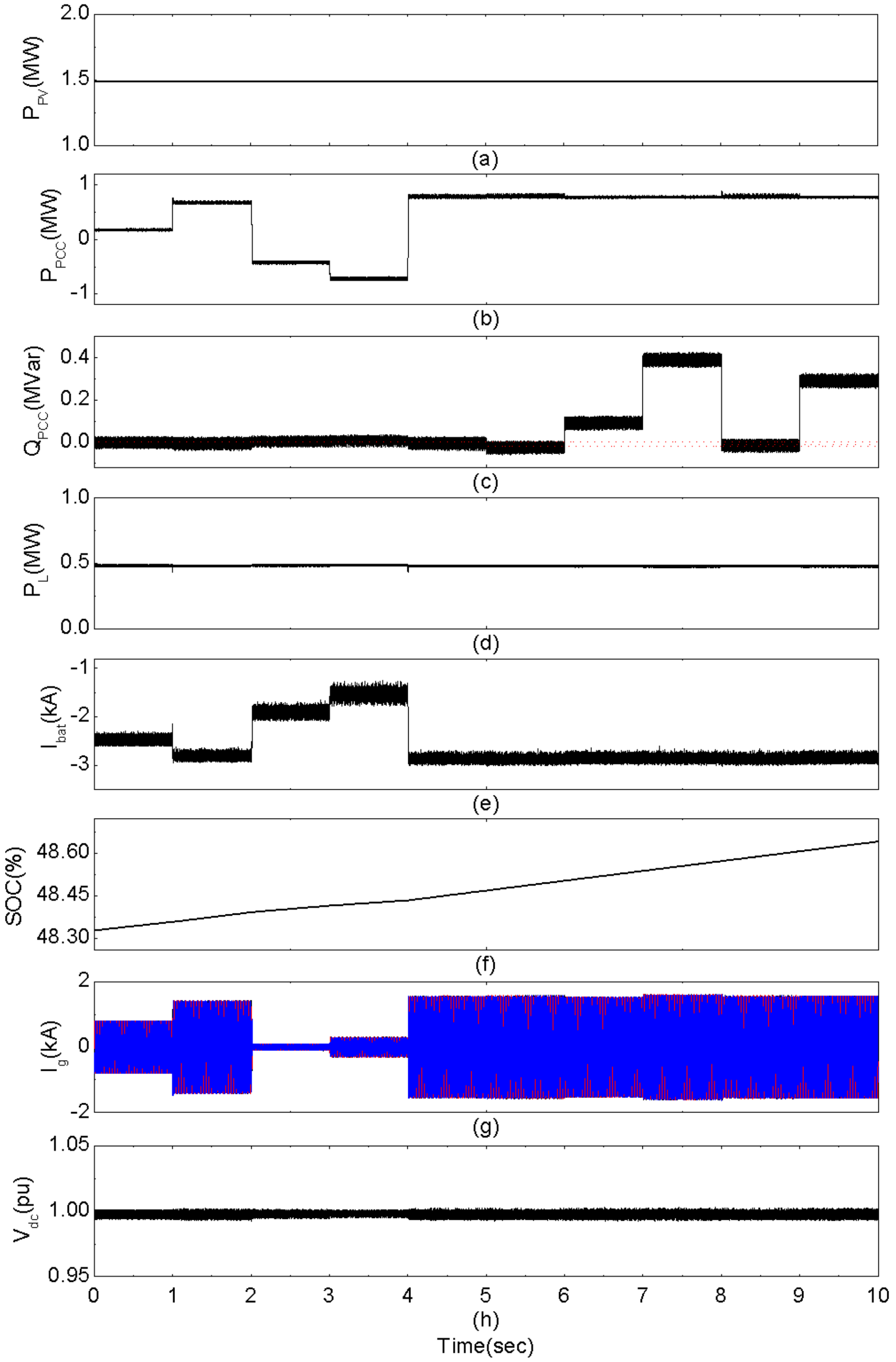

Fig.4-11 Performance of the flexible power regulation using the proposed scheme. (a) PV power, (b) active power at PCC, (c) reactive power at PCC, (d) load power, (e) battery current, (f) SOC, (g) the current flowing between the grid and PV-ESS system, (h) DC-bus voltage.

As shown in Fig.4-11 (b) and (c), the active and reactive powers at PCC track their references fast and precisely. Note that, in this PV-ESS system, it is reasonable that the power references from the grid to DC side (i.e. positive P^* and Q^*) are set to be greater than those with inverse power flows (i.e. negative P^* and Q^*), which is because the grid capacity is huger than that of the PV-ESS MG.

4.4.4 Voltage Support

As mentioned above, the voltage support capability can be performed by taking advantage of the flexibility of power regulation. Since the active power regulation is more flexible than that of reactive power, a larger adjusting range can be employed by adjusting active power to provide the voltage support. Fig.4-12 depicts the voltage support performance by adjusting the active and reactive power regulation. Initially, Load 3 (0.5MW AC load) is connected. At 1s, Load 4 (1MW AC load) is connected, causing the voltage drop at the PCC. The voltage support is activated at 1.5s based on (4-5) and (4-6).

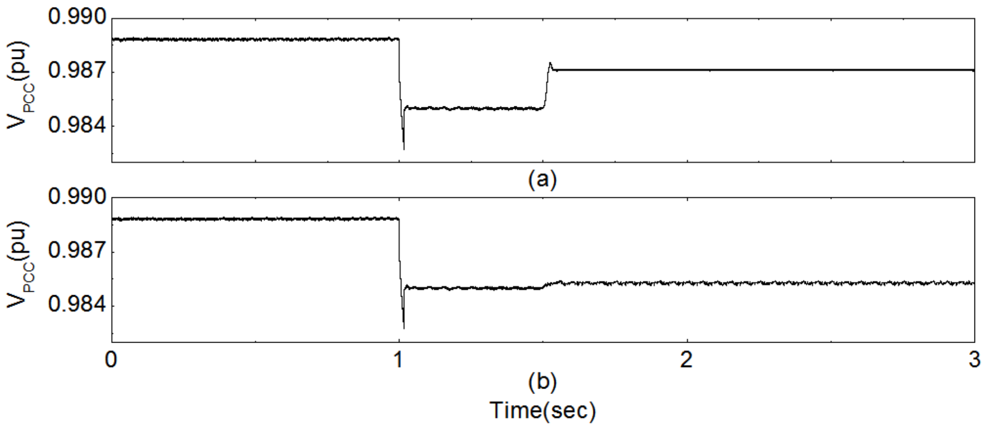

Fig.4-12 Voltage support performance of the proposed scheme. (a) using active power flow control. (b) using reactive power flow control.

As shown, the PCC voltage has been significantly boosted by around 2.20×10^{-3} pu (see Fig.4-12(a)) using active power flow control. Compared with active power, the reactive power capacity is smaller and limited, so the voltage can only be improved slightly by around 0.30×10^{-3} pu (see Fig.4-12(b)). It is promising to see that, with the high integration of MGs into the main grid, reactive power regulation can be more effectively coordinated to provide powerful voltage support.

4.4.5 Robustness and Stability

Since the MPC control principle is built on analysing the filter dynamics, in order to investigate the robustness and stability of the MPC-controlled system, so the key parameters related to both DC- and AC-side filters are considered[121]. Specifically, for the DC side, capacitor C_2 and inductor L are evaluated, while for the AC side, inductor L_f and resistor R_f are evaluated. The key parameters are changed gradually in the controller while the associated physical components are kept unchanged.

To achieve this, for DC side, C_2 and L are respectively varied from 40mF to 60mF (interval step: 1mF) and from 0.1mH to 0.3mH (interval step: 0.01mH); for AC side, L_f and R_f are respectively changed from 0.1mH to 1.1mH (interval step: 0.05mH) and from 1mΩ to 3mΩ (interval step: 0.1mΩ). The simulation runs once when any key parameter changes, leading to total 882 times for the two sides. Three kinds of data indicators, i.e. the DC-bus voltage ripple (V), the absolute error of DC-bus mean voltage to the rated (V), and the THD of AC filter current (%), are evaluated here with the results shown in Fig.4-13. Other settings are: P^* and Q^* are respectively set to 0.8MW and 0Mvar, Load 1 is connected in DC side, while the AC-side is conducted with a constant 1kV DC source.

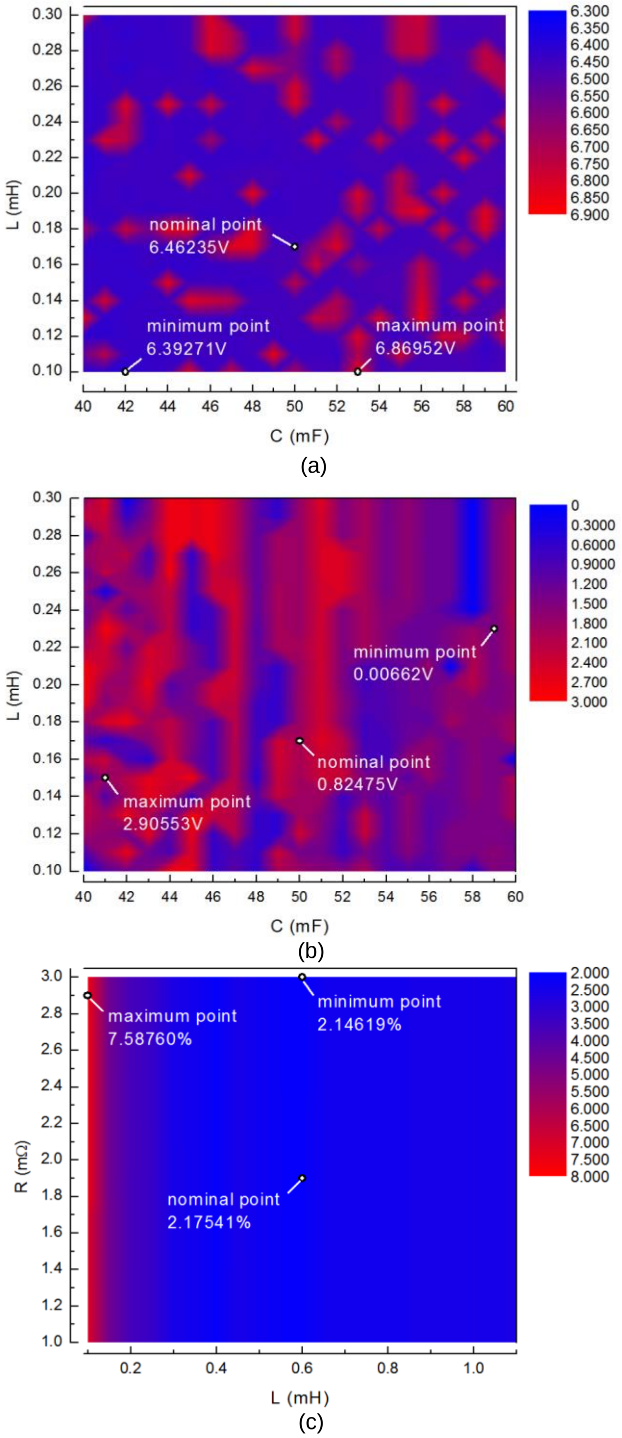

(a)

(b)

(c)

Fig.4-13 Robustness and stability of the system based on key parameter variations. (a) effect on the DC-bus voltage ripple(V), (b) effect on the absolute error of DC-bus mean voltage to the rated(V), (c) effect on the THD of AC filter current(%).

As for Fig.4-13, the performance from better to worse is colored from blue to red. The minimum and maximum points indicate the minimum and maximum values in the relevant region respectively, while the nominal point means using the parameters listed in Table 4-1. By analysing Fig.4-13, the following features can be summarized.

1) The proposed MPPC scheme shows a high stability and robustness against various key control parameter variations. Even with large mismatches, the system can also present acceptable performance. For instance, the maximal DC-side inductance mismatch is up to (0.30-0.17)/0.17=76.47%, however, which only results in around 6.9V DC-bus voltage ripple and 3V deviation from the rated value, which still presents a fine DC supply in terms of a kilovolt-level DC-bus system;

2) No apparent changing trend can be observed from Fig.4-13 (a) and (b), but the boundaries are clarified and all nominal points are included inside the boundaries. In Fig.4-13 (c), the nominal parameters indicate the AC filter current locates in a low THD band and near the optimal one. Inversely, a smaller inductance or a larger inductance will produce a higher THD;

3) Evaluating the proposed MPPC scheme with an extensive variety of key parameters, there is still a large-scale region for the system to keep stable and robust, this is suitable for practical applications regardless of the physical uncertainties and constraints;

4) The system is not necessary to be always forced to operate at the minimum points, since there is always a deviation or mismatch among different evaluation criteria, for example, the minimum points and associated control parameters in Fig.4-13 (a) and (b) are different. In addition, the minimum points may vary with variable loads. Here, as shown, since the nominal points have to be a certain distance to the maximum thresholds, it can prove the system using the proposed scheme is stable and robust. It should

also be noted that, for traditional control stability and robustness analyses, conservative thresholds are also needed to be defined in order to identify the analysis domain[121].

4.4.6 Longer Horizon Prediction

As aforementioned, Euler’s forward difference method (2-3) is mostly adopted to “discrete” the system model in MPC-controlled power converters, so one-step control horizon and prediction are common. However, the prediction horizon is extended here to further investigate the system performance.

In fact, all the predictive models at k+1 instant can be summarized as

$$\mathbf{x}(k+1) = A_m\mathbf{x}(k) + B_m\mathbf{u}(k) \tag{4-9}$$

where **x**, **u** are state variables, A_m, B_m are the coefficient matrices.

One more step prediction (also called one-step delay compensation) of (4-9) becomes[122]

$$\mathbf{x}(k+2) = A_m\mathbf{x}(k+1) + B_m\mathbf{u}(k+1) \tag{4-10}$$

Here, using the linear extrapolation method to expand the prediction horizon N (>2)[123]

$$\mathbf{x}(k+N) = \mathbf{x}(k+1) + (N-1)[\mathbf{x}(k+2) - \mathbf{x}(k+1)] \tag{4-11}$$

Based on these, a longer-horizon prediction using the proposed MPPC scheme with the same prediction horizon on both DC and AC sides is performed. Fig.4-14 plots the results with the same evaluation criteria used above in the last subsection.

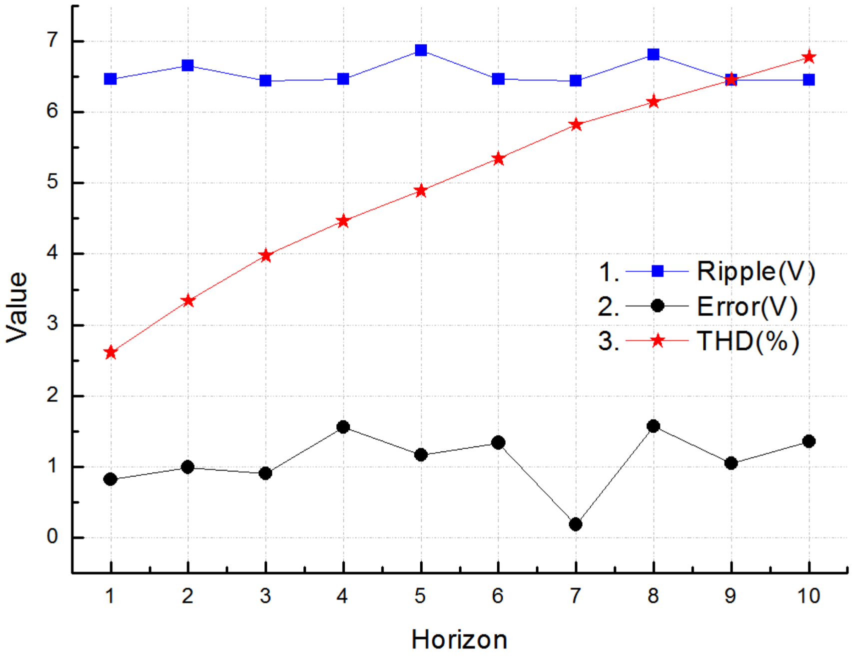

Fig.4-14 Effect of the longer-horizon prediction on system performance

As shown, curve 1 depicts the DC-bus voltage ripple(V), curve 2 plots the absolute error of DC-bus mean voltage to the rated(V), and curve 3 draws the THD of AC filter current(%). It is clear that no obvious trends can be found for curves 1 and 2, while curve 3 shows a continuous increase when the prediction horizon increases. It means that a longer-horizon prediction might bring about an inferior performance because the prediction accuracy may discount when the horizon is increased.

4.4.7 Comparison

In this subsection, the proposed MPPC scheme is compared with traditional existing MPC methods and their combination. Conventionally, in a grid-connected MG system, the DC bus is maintained by a rectifier (i.e. active-front-end (AFE) converter) using the MPC method whose active power reference is defined by an external PI controller taking DC-bus voltage errors as its inputs[124]. While at the same time, the DC-side DC-DC converter in the ESS is regulated by the MPC method with currents included in the cost function. The traditional control diagram is depicted in Fig.4-15. The PI control parameters are given in Table 4-1, which has been tuned taking into account both the response speed and steady-state error.

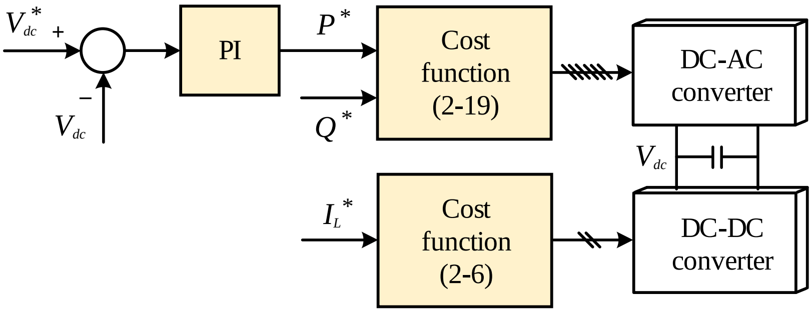

Fig.4-15 Traditional MPC methods and their combination for comparison

For a fair reason, the variable loads keep the same as Subsection 4.4.1. The battery current (mean value) also keeps the same which means the current reference changes as the same load changing statuses as shown in Fig.4-8(e), Q^* is set to 0Mvar. The comparison results are shown in Fig.4-16, and the following observations are listed.

1) Since the DC-bus voltages are maintained by different means, as shown in Fig.4-16(a), the DC-bus voltage of existing MPC is slightly higher than that of the proposed scheme, which is because the existing MPC with PI controller can eliminate steady-state errors, but it also shows an obvious overshoot during load changes;

2) From Fig.4-16(c), the battery current ripple of using existing MPC is less than that of the proposed scheme, however, this is because their current references are given to constant values, never considering the current flows inside the PV-ESS on the DC side;

3) It is noted that the flexible power regulation function of the inverter becomes powerless when using existing MPC since existing MPC has paid all attention to regulate the DC-bus voltage. Besides, existing MPC makes the current references on DC side difficult to determine;

4) In the AC side, the AC current THD of the proposed scheme with two cycles is 2.26% while that of the existing MPC is 2.81%, larger than the proposed one. This can be owed to the more stable and smooth DC-bus voltage provided by the proposed scheme.

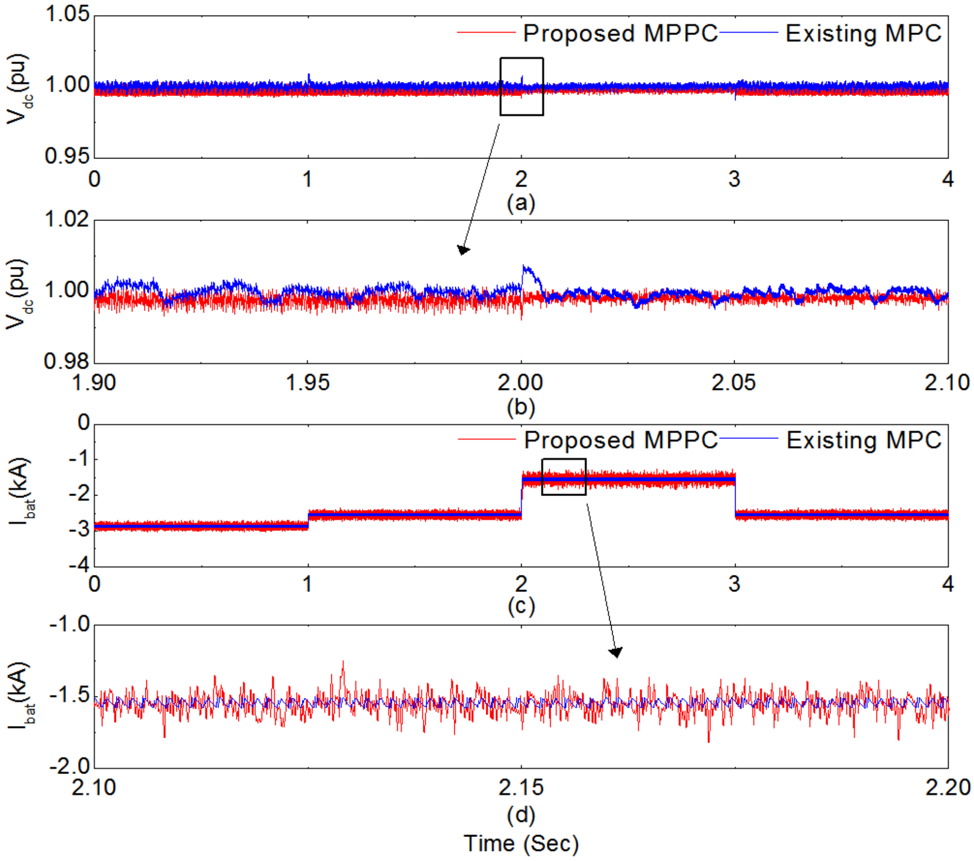

Fig.4-16 Comparison with existing MPC methods and their combination. (a)&(b) DC-bus voltage, (c)&(d) battery current.

4.4.8 CHIL Test

The proposed MPPC scheme is further verified using the CHIL tests[125]. Fig.4-17 shows the CHIL system setup. For the implementation, the proposed MPPC control algorithm is built on a digital signal processor (DSP) controller (TMS320F28335), while other physical components, like the PV system, ESS system, and power converters are constructed in the OPAL-RT real-time simulator (RT-LAB OP4510). The system variables are measured from RT-

LAB OP4510 and delivered to the DSP for optimal selection of voltage vectors according to the MPPC algorithm. Then the gate driving signals are generated from the DSP and sent back to RT-LAB OP4510 to realize the control of the DC-DC converter and the inverter. Here, P^* and Q^* are set to 0.2MW and 0Mvar, respectively. The solar irradiation and temperature are set to 600W/m^2 and 25℃, respectively. Load 3 (0.5MW AC load) is initially connected to the AC bus.

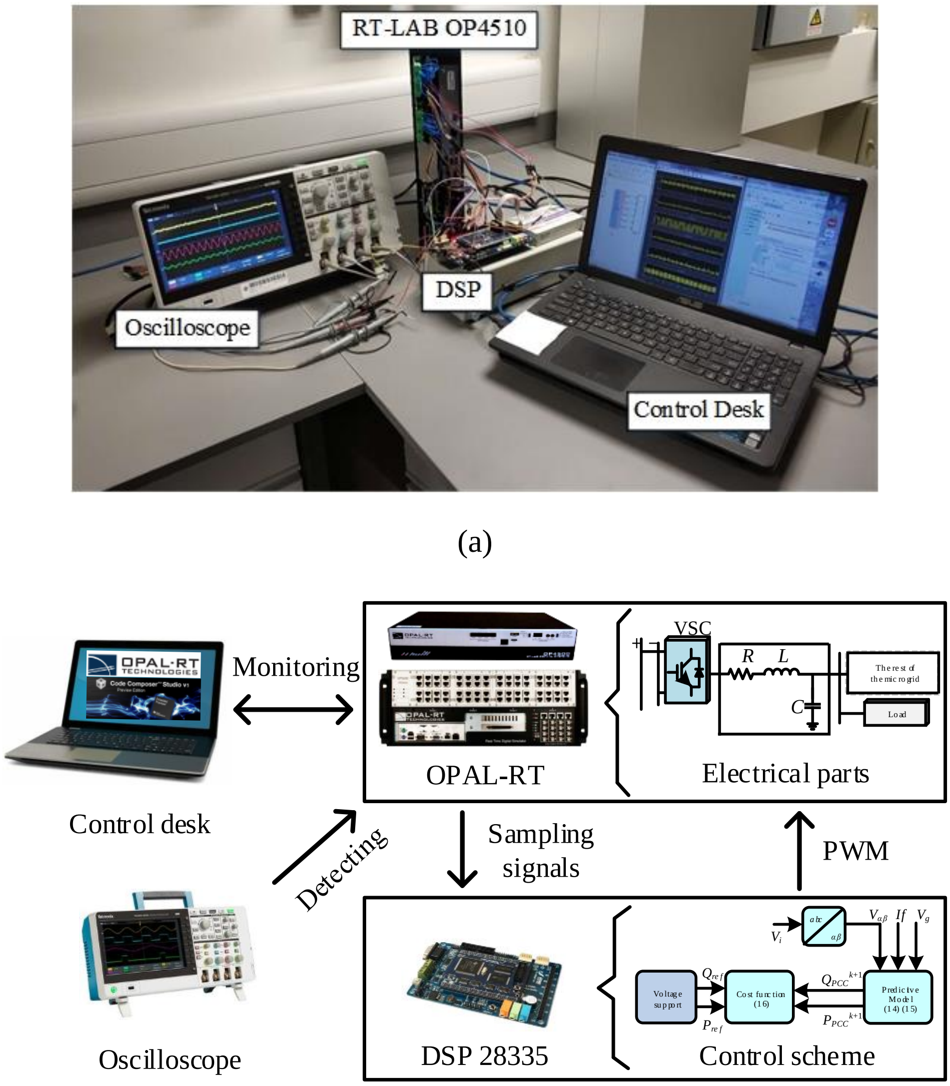

(a)

(b)

Fig.4-17 CHIL system setup. (a) laboratory setup. (b) schematic diagram.

The gate driving signals produced by the DSP controller are shown in Fig.4-18. The upper two gate driving signals are from the bidirectional DC-DC converter, while the bottom two signals are from one leg of the DC-AC converter. These signals are complementary and with deadtime bands.

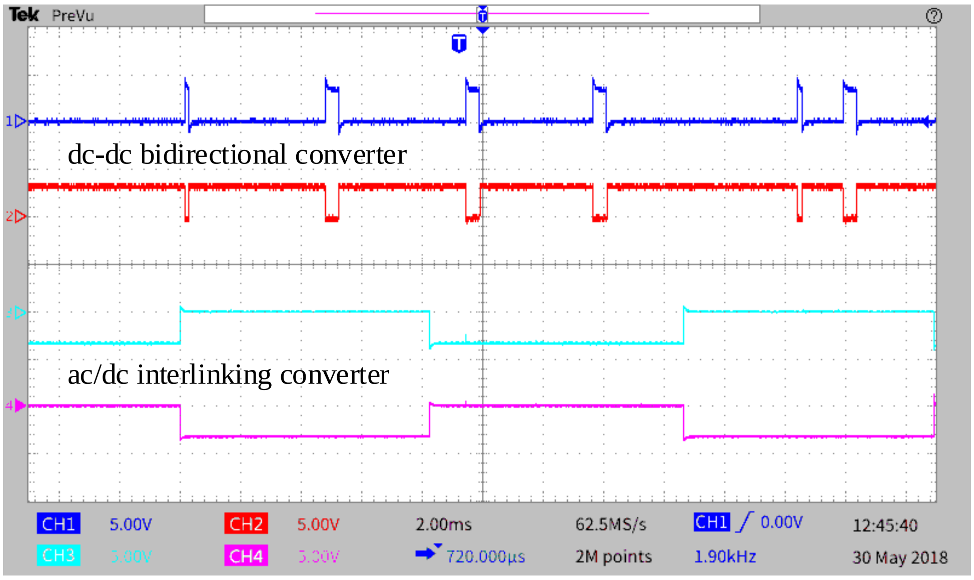

Fig.4-18 Gate driving signals

Fig.4-19 (a) and (b) show the tracking performances when P^* steps up from 0.2MW to 0.4MW and steps down from 0.4MW to 0.2MW, respectively. It can be observed that when the power reference changes, the system dynamically tracks the power references and reaches the new balance within around 40ms. During these processes, the DC-bus voltage keeps stable, and the system can also provide a stable AC voltage supply. It has verified the effectiveness of the proposed MPPC scheme in providing a flexible power regulation and maintaining the stable DC and AC voltages.

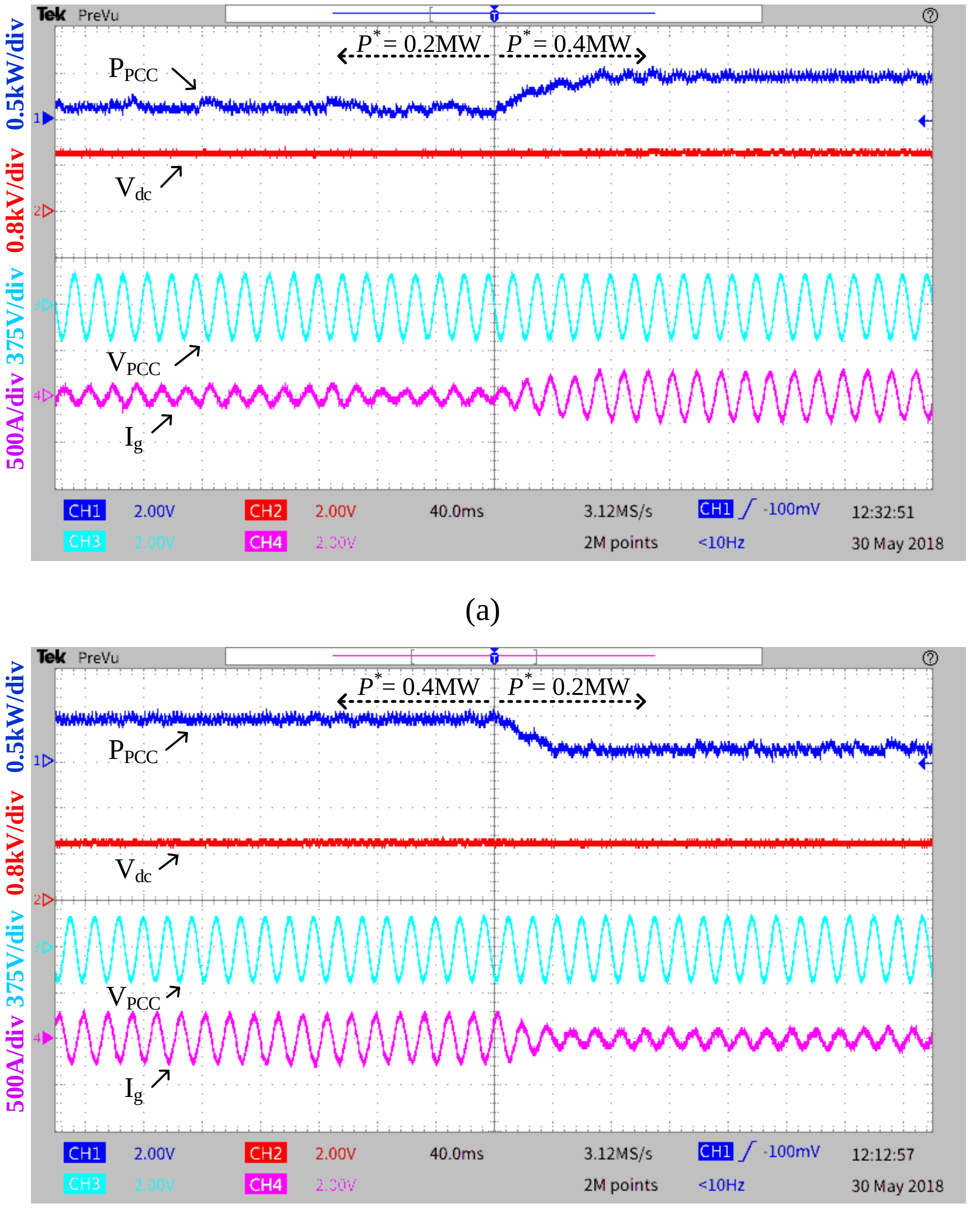

(a)

(b)

Fig.4-19 CHIL results when power reference changes. (a) active power reference steps up, (b) active power reference steps down.

4.5 Summary

This section proposes an MPPC scheme for a PV-ESS MG system. The MPPC for the DC-DC bidirectional converter aims to provide a stable and robust DC-bus voltage, by using the MPPC, the fluctuating PV output power has been smoothed, reducing the influence to the grid in grid-connected MGs.

The MPPC for the inverter allows for a flexible power regulation and a stable AC power supply. Then a voltage support service is provided to compensate the voltage dips resulted from the load changes. The proposed MPPC scheme has been validated by numerical simulation cases and CHIL tests.

Chapter 5 MPC for PV-ESS MGs with Secondary Restoration Capability

Currently, the droop control method for parallel DGs is often adopted in a decentralized manner for MGs. However, this method presents inherent frequency and voltage deviations. In addition, traditional CLC double loops expose a relatively slow dynamic response to deal with the fluctuation of RES outputs. Thus, the combination of the droop control method and CLC double loops leads to a further voltage quality deterioration.

To solve the above problems, in this section, a new MPPC scheme involving the battery constraints is proposed for bidirectional DC-DC converters to smooth the PV outputs and stabilize the DC bus. An MPVC scheme considering the voltage changing trend is adopted for inverters with an improved AC voltage output. Moreover, a washout filter based power sharing method with a further voltage compensation is used for the power sharing among DGs and to mitigate the frequency and voltage deviations. The proposed schemes are numerically studied in the Matlab/Simulink and tested by using CHIL under fluctuating PV outputs and variable loads.

5.1 Background and System Configuration

As previously mentioned, the droop control method has inherent frequency and voltage deviations. In order to eliminate the deviations, a secondary control method can be adopted. Today, distributed secondary control with reduced communication cost has been more attractive. Among them, the washout filter based method is a promising alternative to simultaneously share the power and eliminate the deviations[126]. The equivalence of the distributed secondary control to the washout filter based method is derived in [127]. However, for the washout filter based method, its incapacity of restoring the PCC voltage to the rated value and the limitation of the "equivalence" are overlooked in [126] and [127]. Hence, it is needed to further explore the washout filter based method to be applied in distributed power systems.

Still focused on PV-ESS MGs, this section proposes a new MPPC scheme for the bidirectional DC-DC converter in the ESS system in the DC subgrid, and an MPVC scheme incorporated with a washout filter based method for the parallel inverters in the AC subgrid. The major contributions and features in this section are listed as follows[128]:

1) The DC bus is formed by a PV-ESS system, the fluctuating power generation from PV systems is handled using the proposed new MPPC scheme which only needs the measurements inside the ESS.

2) The washout filter based method is used for power sharing rather than using the droop control method, the frequency and voltage deviations are compensated simultaneously. A possible solution is proposed to address the limitation of the "equivalence" in [127] and solve the incapacity of restoring the PCC voltage to the rated value.

3) The washout filter based method is combined with the improved MPVC method which takes into account the changing trend of the voltage trajectory, presenting a better tracking process and improved voltage quality.

Fig.5-1 shows the topology of the MG system with the PV-ESS system and multiple converters. There are two subgrids (DC and AC) in the MG system. Each DG system has its own DC bus and is connected to the AC bus (PCC) through the inverter, then prepared for the grid connection. More DG systems can be interconnected due to the plug-and-play feature of the proposed control schemes.

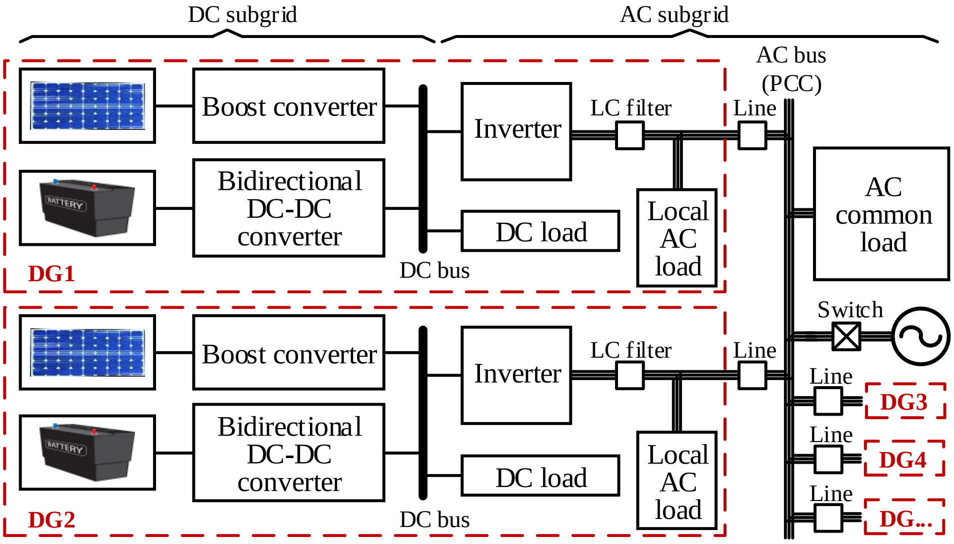

Fig.5-1 An MG system with PV-ESS system and multiple converters

5.2 New MPPC Scheme

The PV-ESS topology studied here is shown in Fig.5-2. A battery and a bidirectional buck-boost converter are equipped in each ESS unit. In islanded mode, the ESS should fill the gap between the RES power generation and the load power consumption. The switching states of the bidirectional DC-DC converter are stated in Subsection 2.1.2.

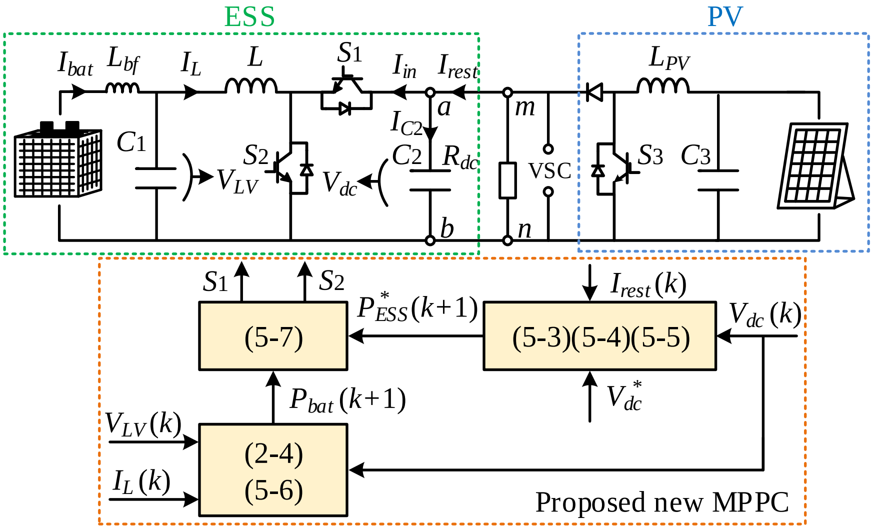

Fig.5-2 PV-ESS topology and proposed new MPPC scheme

In Fig.5-2, according to the KCL, the currents of Node *a* has the relationship

$$I_{in} = I_{rest} - I_{C2} \tag{5-1}$$

where I_{in} is the current absorbed by the ESS, I_{rest} is the current flowing to Node *a* or the current flowing from other parts of the MG, and I_{C2} is the current of capacitor C_2.

Here, the power balance is also the main focus for the DC-DC converter, so the required power for the ESS to be supplied/absorbed should be

$$P_{ESS}^{*} = \left| I_{in} \cdot V_{dc}^{*} \right| \tag{5-2}$$

where V_{dc}^{*} is DC-bus voltage reference.

Using the linear approximation of the capacitor in Subsection 3.2.1, at *k* instant, the current of C_2 can be predicted by

$$I_{C2}(k+1) = \frac{1}{N}\left(\frac{C_2}{T_s}(V_{dc}^{*} - V_{dc}(k))\right) \tag{5-3}$$

where *N* is the coefficient, T_s is the sampling time, and V_{dc} is the actual DC-bus voltage.

Rewrite (5-1), one can have the predicted I_{in} with

$$I_{in}(k+1) = I_{rest}(k) - I_{C2}(k+1) \tag{5-4}$$

And then, (5-2) can be predicted as

$$P_{ESS}^{*}(k+1) = \left| I_{in}(k+1) \cdot V_{dc}^{*} \right| \tag{5-5}$$

On the other hand, the battery output power is predicted by

$$P_{bat}(k+1) = \left| I_L(k+1) \cdot V_{LV}(k) \right| \tag{5-6}$$

where $I_L(k+1)$ is obtained from (2-4).

The cost function should involve the power balance of the two-side ports of the DC-DC converter

$$\begin{gathered} J_P = \left| P_{ESS}^{*}(k+1) - P_{bat}(k+1) \right| \\ s.t.\ \mathrm{SOC}_{\min} \le \mathrm{SOC} \le \mathrm{SOC}_{\max},\ P_{bat} \le P_{bat\_rated} \end{gathered} \tag{5-7}$$

The proposed new MPPC scheme is illustrated as shown in Fig.5-2. The rest of the current outside the ESS $I_{rest}(k)$, the actual DC-bus voltage $V_{dc}(k)$, and its reference V_{dc}^* are used to compute the ESS power $P_{ESS}^*(k+1)$ at k+1 instant as per (5-3)-(5-5). At the same time, $V_{LV}(k)$ and $I_L(k)$, as well as $V_{dc}(k)$, are all used to predict the inductor current $I_L(k+1)$ at k+1 instant. Next, according to (2-4) and (5-6), the predicted battery output power $P_{bat}(k+1)$ is obtained. Finally, the switching signals that minimize the cost function (5-7) will be selected and used for the DC-DC converter. Note that the MPPC here only detects the local ports inside the ESS system, which is more convenient than that in Section 3.

5.3 Washout Filter based Power Sharing Method

In Subsections 2.4.1 and 2.4.2, the primary droop control method and secondary centralized PI-based method are respectively presented. Here, they are recalled again as follows.

The droop control method is expressed as

$$f = f^* - mP \tag{5-8}$$

$$E = E^* - nQ \tag{5-9}$$

where f and f^* are the measured and reference values of the frequency, E and E^* are the measured and reference values of the voltage, m and n are the droop coefficients, and P and Q are the actual active and reactive powers, respectively.

The centralized PI-based secondary control method in the S domain is written as

$$f_c = k_{pf}(f^* - f) + \frac{k_{if}}{s}(f^* - f) \tag{5-10}$$

$$E_c = k_{pE}(E^* - E) + \frac{k_{iE}}{s}(E^* - E) \tag{5-11}$$

where f_c and E_c are the frequency and voltage compensations, k_{pf} and k_{if} are the P and I coefficients of the frequency control, k_{pE} and k_{iE} are the P and I coefficients of the voltage control, respectively.

The washout filter based power sharing method can be derived by combining the droop control method and the centralized PI-based secondary control method. For example, the frequency f with the secondary control can be expressed as

$$f = f^* - mP + f_c \tag{5-12}$$

With only an integral controller (i.e. $k_{pf}=0$) to realize the secondary control, (5-10) can be simplified as

$$f_c = \frac{k_{if}}{s}(f^* - f) \tag{5-13}$$

Substitute (5-12) into (5-13), we have

$$f_c = \frac{k_{if}}{s}(f^* - (f^* - mP + f_c)) = \frac{k_{if}}{s}(mP - f_c) \tag{5-14}$$

then,

$$f_c = \frac{k_{if}}{s + k_{if}} mP \tag{5-15}$$

Substitute (5-15) in (5-12), one can obtain

$$f = f^* - \frac{s}{s + k_{if}} mP \tag{5-16}$$

Compared to (5-8), there is an extra coefficient $s/(s+k_{if})$ in (5-16), which is right the washout filter's S transfer function. Via this filter, DC components can be blocked and transient components can be passed, making the power sharing more robust against parameter uncertainties[129].

Similarly, (5-9) has its corresponding washout filter's equation

$$E = E^* - \frac{s}{s + k_{iE}} nQ \tag{5-17}$$

From the derivation, the washout filter based power sharing method has the capability to restore the frequency and voltage deviations caused by the droop control method. However, this equivalence has the following limitations:

1) For the washout filter based method, the frequency and voltage are measured in the controller rather than in the PCC, which makes it different from the centralized PI-based secondary control method;

2) The frequency and voltage that can be restored to the rated values are just the controller's output frequency and voltage, that is, the f and V in (5-16) and (5-17), not the PCC's;

3) The inverter output voltage can be restored to the rated value under no-load condition. However, once a local load with a large power is connected, the restoration effect will not be obvious.

These limitations deteriorate the effect of using the washout filter based method serving as a secondary method. However, a possible solution is given below.

The steady-state frequency of the MG system is a global variable, no matter when it is changed and where it is measured. According to the droop control method, the instantaneous frequency of the system will be changed with the variation of the active power. However, the situation of the voltage will be different from that of the frequency since the voltage will drop across transmission lines and different line impedances result in different reactive power sharing. The voltage drop across the transmission line can be approximately computed by[130]

$$eE \approx \frac{XQ_e + RP_e}{E^*} \tag{5-18}$$

where X and R are the inductive and resistive impedance, Q_e and P_e are the reactive and active powers across the impedance, respectively, and E^* is the voltage reference.

In order to further compensate the voltage deviation due to the effect of line impedance. The following secondary control of the voltage can be used

$$E = E^{*} - \frac{s}{s + k_{iE}} nQ + dv \cdot eE \cdot \underset{\textit{lowpass filter}}{\frac{f_l}{s + f_l}} \tag{5-19}$$

where *dv* is the coefficient.

It is noted that, the transmission line impedance, i.e. *X* and *R*, can be obtained by both offline and online methods. The offline method evaluates the impedance using original systematic states[25]. While the online method estimates the impedance via real-time measurements[131].

The determination of *dv* can be achieved according to the EMS which also provides the information of Q_e and P_e. Note that the setting of *dv* can raise the output voltage of the inverter, so the local electric power supply rules must be met. For a voltage threshold φ, the upper approximation of *dv* can be defined as

$$dv \le \varphi \cdot E^{*} \Big/ \left(\frac{XQ_0 + RP_0}{E^{*}} \right) \tag{5-20}$$

where Q_0 and P_0 are related to the DG’s capacity, and φ is the ratio of local electric power supply rule which is set to 10% here.

5.4 Improved MPVC Scheme

As already mentioned, in an islanded MG system, the common-used MPC-controlled converter will set the predictive model as (2-12), and the cost function as (2-13). In fact, (2-13) only involves the voltage magnitudes, which is not always able to guarantee a tight tracking since the objective voltage changes with time and there exists vibrations. This phenomenon will deteriorate the tracking accuracy.

Here, an improved tracking manner taking into account the voltage changing trend is adopted to tightly track the trajectory of the objective voltage [25]. Fig.5-3 shows the analysis of the voltage tracking. To begin with, assuming both the traditional and improved tracking methods have the same magnitude error ΔE_0 at the k instant. Besides, their changing trends are also the same as the reference (i.e. the slopes of the trajectories S_{tra0} and S_{imp0} are both equal to S_{ref0}). For a simple analysis, only considering two alternative predicted values which are prepared to be selected in future instants, e.g. V_1 and V_2. At the k+1 instant, V_1 and V_2 have the same error as the reference's, noted ΔE_1. The tracking at this instant can either choose V_1 or V_2. In order for a tight tracking, only considering the magnitude is not enough, it is better to also consider the slope. In this way, the trajectory of the improved track will be $S_{imp1} = S_{ref1}$(see the red curve), otherwise, the traditional track may happen when $S_{tra1} \neq S_{ref1}$, leading to an inferior tracking result(see the blue curve).

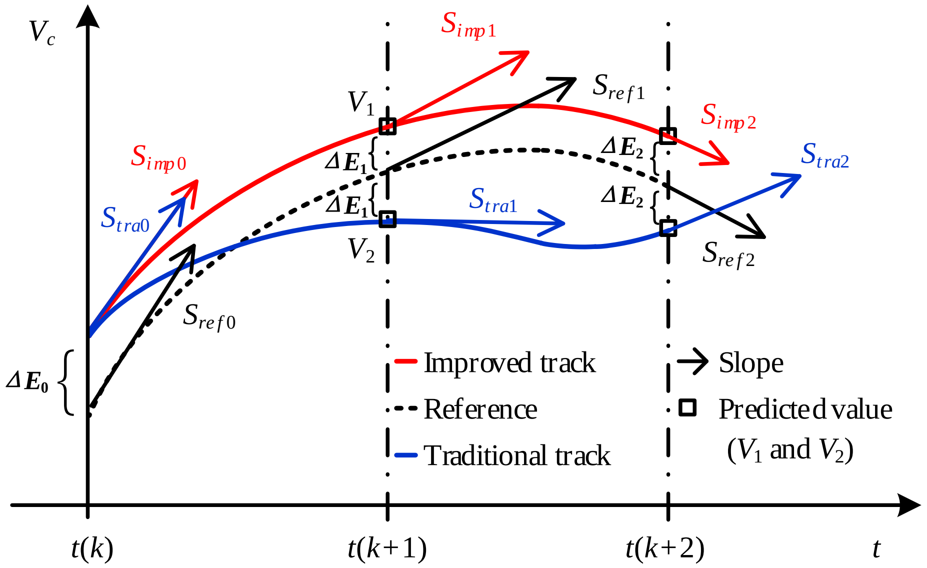

Fig.5-3 Voltage tracking analysis

When one more step is applied, this situation may deteriorate. At k+2 instant, also with the same error ΔE_2 , when the slope is considered ($S_{imp2} = S_{ref2}$), the improved tracking method can tightly track the reference (see the red curve). Otherwise, when the slope is omitted and not identical

($S_{tra2} \neq S_{ref2}$), the tracking trajectory by the traditional method will keep away from the reference, leading to a higher harmonic distortion (see the blue curve).

The slope depicted in Fig.5-3 is actually the derivative of the VSC output voltage. To include the derivative terms, the cost function should add one more part, i.e. the predicted derivative term and its reference of the VSC output voltage (V_c).

To begin with, the capacitor voltage reference can be written as

$$\begin{aligned} V_{\mathrm{c}}^{*} &= V_{c\alpha}^{*} + jV_{c\beta}^{*} \\ &= V_{\mathrm{c}} \sin(\omega t(k)) + jV_{\mathrm{c}} \cos(\omega t(k)) \end{aligned} \tag{5-21}$$

where ω is the frequency in radian.

Making a derivative of (5-21), it yields

$$\begin{aligned} \frac{dV_{\mathrm{c}}^{*}}{dt} &= \omega V_{\mathrm{c}} \cos(\omega t(k)) - j\omega V_{\mathrm{c}} \sin(\omega t(k)) \\ &= \omega V_{c\beta}^{*} - j\omega V_{c\alpha}^{*} \end{aligned} \tag{5-22}$$

The derivative of (2-9) in discrete time is

$$\begin{aligned} \frac{dV_{\mathrm{c}}(k+1)}{dt} &= \frac{I_f(k+1) - I_L(k)}{C} \\ &= \frac{I_{f\alpha}(k+1) - I_{L\alpha}(k)}{C} + j\frac{I_{f\beta}(k+1) - I_{L\beta}(k)}{C} \end{aligned} \tag{5-23}$$

where $I_{f\alpha,\beta}(k+1)$ is from (2-12).

Make a subtraction between (5-22) and (5-23), the cost function with the derivative term can be determined as

$$\begin{aligned} J_{VD} &= \left(\omega V_{c\beta}^{*} - \left(\frac{i_{f\alpha}(k+1) - i_{\mathrm{o}\alpha}(k)}{C}\right) \right)^2 \\ &\quad + \left(\omega V_{c\alpha}^{*} + \left(\frac{i_{f\beta}(k+1) - i_{\mathrm{o}\beta}(k)}{C}\right) \right)^2 \end{aligned} \tag{5-24}$$

Eventually, the complete cost function with improved tracking process is

$$J = aJ_V + bJ_{VD} \tag{5-25}$$

where a, b are the weighting factors. The first term J_V means to track the voltage magnitude, while the second term J_{VD} means to track the voltage changing trend.

5.5 Overall Control Scheme

In order for a better comparison, the traditional droop control method with CLC loops is plotted in Fig.5-4, while the proposed overall control scheme is summarized in Fig.5-5.

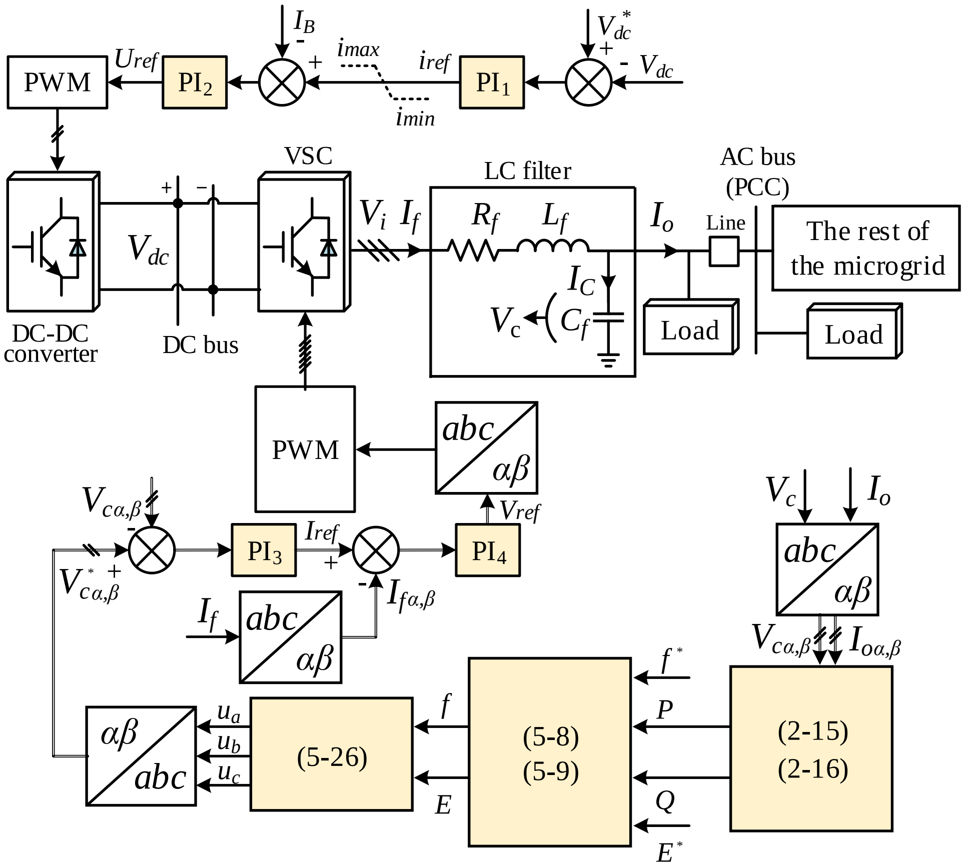

Fig.5-4 Control diagram of traditional overall control scheme

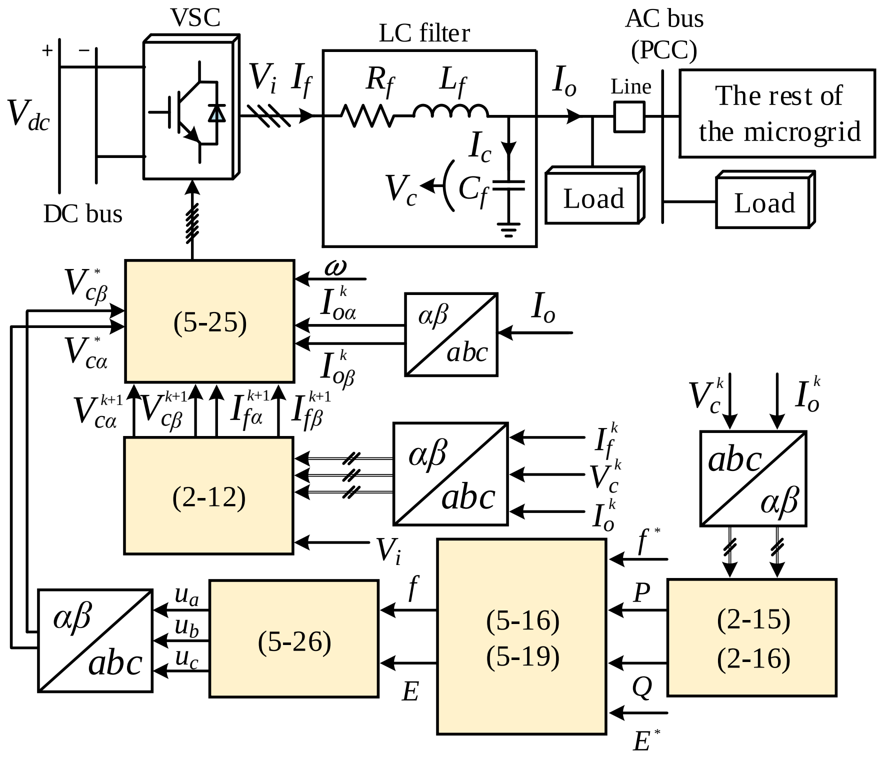

Fig.5-5 Control diagram of the proposed overall control scheme (improved MPVC & improved washout filter based power sharing method)

The frequency and voltage references are produced by the washout filter-based power sharing method, thus the voltage conversion is required

$$\begin{cases} u_a = E\sin(2\pi f + 0) \\ u_b = E\sin(2\pi f - 2\pi/3) \\ u_c = E\sin(2\pi f + 2\pi/3) \end{cases} \tag{5-26}$$

where u_a, u_b, and u_c are the three-phase voltages.

5.6 Verification

In this subsection, the MG system plotted in Fig.5-1 and the proposed control schemes shown in Fig.5-2 and Fig.5-5 are numerically simulated in the Matlab/Simulink and CHIL tests are also conducted. System parameters are listed in Table 5-1. For simplicity, DG1 and DG2 have the same setting. The nonlinear load is represented by a diode-bridge rectifier with a parallel-connected capacitor and a parallel-connected resistor. A sequence of events is described in Table 5-2.

Table 5-1 System Parameters

Description	**Value**
Solar PV	SunPower Spr-305-WHT, 200kW (STD)
Battery	Lithium-Ion, 500V, 1.6kA·h
DC rated voltage	1000V
DC-side circuit	L_{bf} = 50μH, L = 170μH, L_{PV} = 80mH, C_1 = 50mF, C_2 = 26mF, C_3=100μF
AC-bus voltage	380V (p-p, rms), 50Hz
AC-bus LC filter	R_f = 0.02Ω, L_f = 3.6mH, C_f = 200μF
Line impedance	R_{line} = 0.1Ω, L_{line} = 2.4mH
New MPPC	N = 1
Power sharing	m = 1.25e-5, n = 8.33e-5, k_{if} = 15, k_{iE} = 10, f_l = 6.25Hz
Washout filter	dv =1.84 during 1s ~ 3s, other time: 1.62
MPVC	Improved: (a = 0.8, b = 0.2), Conventional: (a = 1, b = 0)
Sampling interval	20μs
Initial DC loads	DG1: 20kW, DG2: 20kW
Initial AC loads	DG1: (50kW, 0kVar), DG2: (50kW, 0kVar)
Common AC load	(40kW, 10kVar)
Nonlinear AC load	R_{nl} = 75Ω, C_{nl} = 20mF
Double loops	PI$_1$: (k_p =10, k_i =50), PI$_2$: (k_p =1.5, k_i =1); PI$_3$: (k_p =5, k_i =0.2), PI$_4$: (k_p =0.24, k_i =0.01)

Table 5-2 Events

Event	Operations	Time(s)
1	AC common load increases from (40kW, 10kVar) to (80kW, 20kVar)	1
2	Each DG’s DC load increases from 20kW to 40kW	2
3	AC common load decreases from (80kW, 20kVar) to (40kW, 10kVar)	3

5.6.1 DC-side Control

The performance of the proposed new MPPC scheme under the situation of fluctuating solar irradiation and ambient temperature is presented in Fig.5-6. The load changes as per Table 5-2. As shown in Fig.5-6(c), a fluctuating PV output is generated based on the fluctuating solar irradiation (see Fig.5-6(a)) and ambient temperature (see Fig.5-6(b)). Fig.5-6(d) shows the battery currents, while Fig.5-6(e) depicts the battery SOC. By using the proposed new MPPC scheme, a stable and smooth DC-bus voltage is produced, as shown in Fig.5-6(f).

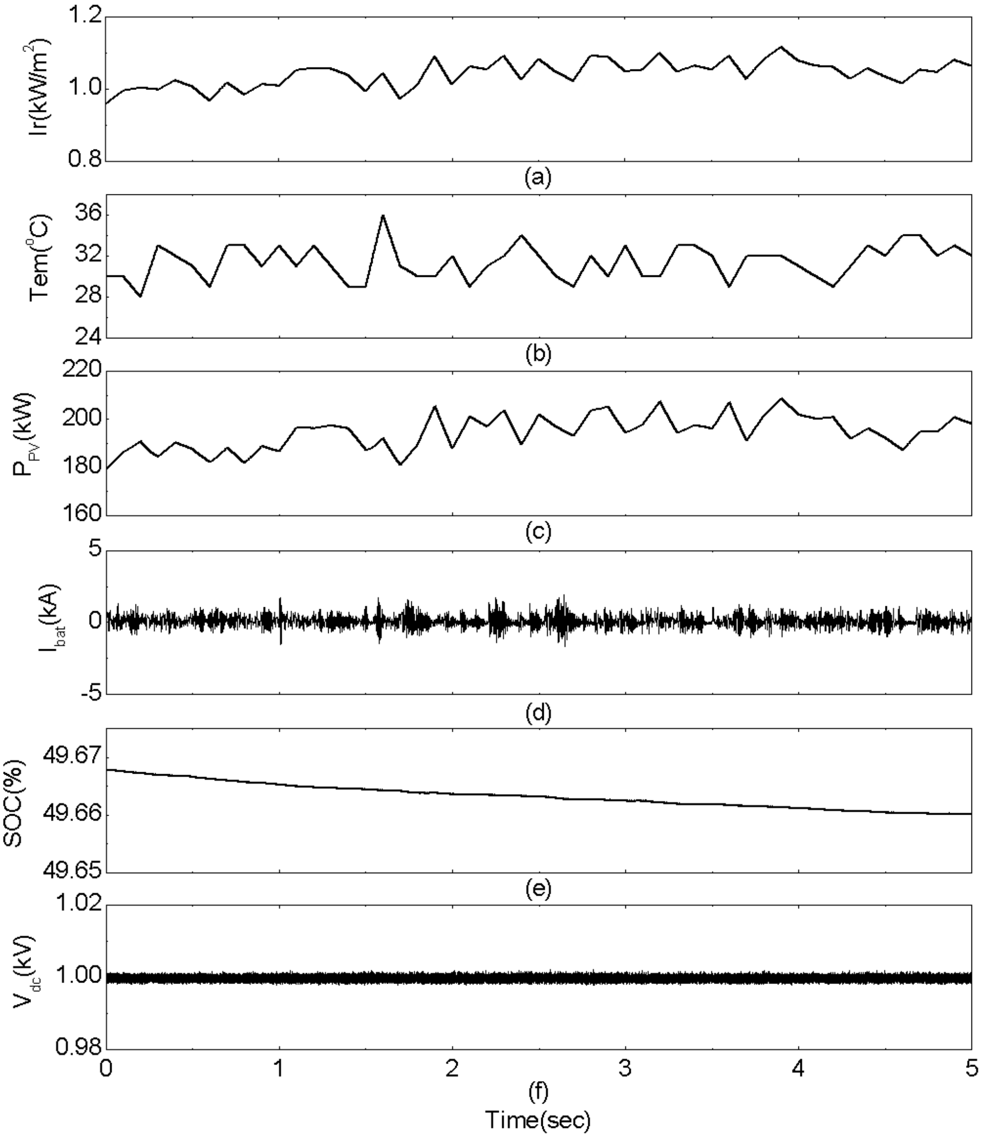

Fig.5-6 Performance of the proposed new MPPC scheme. (a) solar irradiation, (b) ambient temperature, (c) PV output power, (d) battery current, (e) battery SOC, (f) DC-bus voltage.

Fig.5-7 compares the DC-bus voltages by using the proposed new MPPC scheme and traditional CLC loops with the same situation of power generation and consumption. As shown in Fig.5-7(b), for the nominal 1 kV bus, the maximum positive deviation is 0.00485 (+0.485%), while the maximum negative deviation is -0.00685 (-0.685%). It is clear that the new MPPC scheme can provide a better controllability over the DC bus.

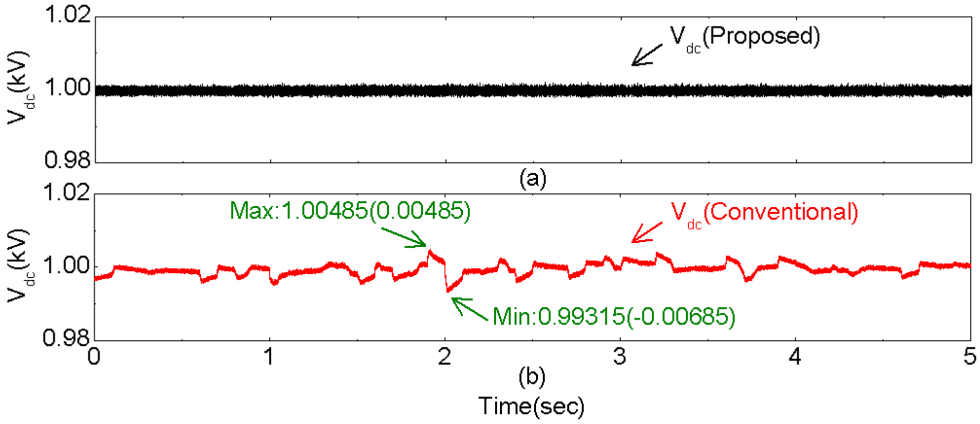

Fig.5-7 Comparison of DC-bus voltages. (a) proposed new MPPC scheme, (b) traditional CLC loops.

5.6.2 Secondary Restoration

Here, the performance of the washout filter based method and improved MPVC on AC subgrid have be investigated. An initial high-capacity local load (50 kW) is connected, as listed in Table 5-1. The load changes follow the events listed in Table 5-2. Fig.5-8 shows the results under the same condition of power generation and consumption as that in Subsection 5.6.1. As shown, Inverter #1 and #2 adjust their outputs proportionally according to the load changes. Simultaneously, the system frequency can be restored to the nominal value (see Fig.5-8(c)) and the PCC voltage can be compensated near to the nominal value (see Fig.5-8(e)). By comparison, using the traditional droop control method and CLC loops, the frequency and voltage show more apparent deviations, leading to a deteriorated power quality (see Fig.5-9 (c) and (e)).

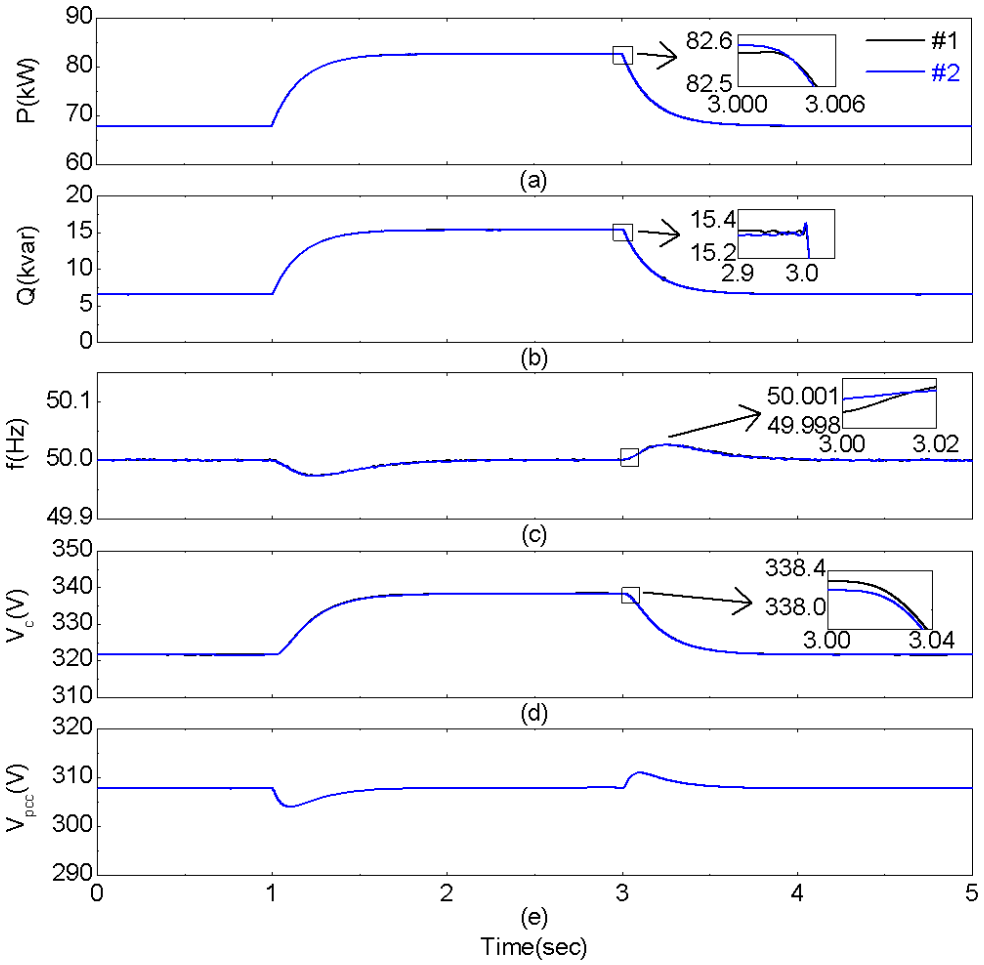

Fig.5-8 Overall performance of the proposed washout filter and improved MPVC scheme of Inverter #1 and #2. (a) active power, (b) reactive power, (c) frequency, (d) inverter output voltage, (e) PCC voltage.

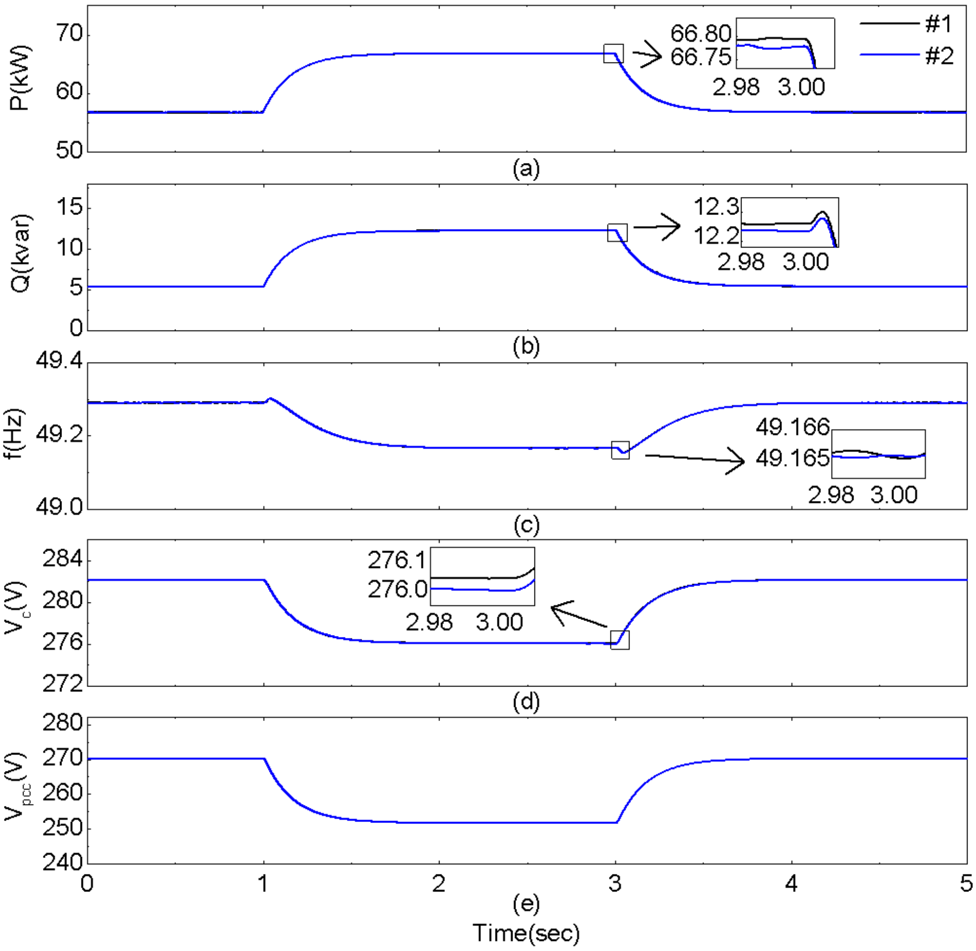

Fig.5-9 Overal performance of the traditional droop method with CLC loops of Inverter#1 and #2. (a) active power, (b) reactive power, (c) frequency, (d) inverter output voltage, (e) PCC voltage.

Fig.5-10 shows the zoom-in voltage waveforms by using the improved MPVC scheme under liner loads. It can be observed that the voltage by using the improved MPVC scheme is more sinusoidal (only 0.18% THD) than that of the conventional one (1.05% THD). When non-linear loads are supplied, the performance is shown in Fig.5-11. It is concluded that the improved MPVC presents a superior performance than that of the conventional MPVC.

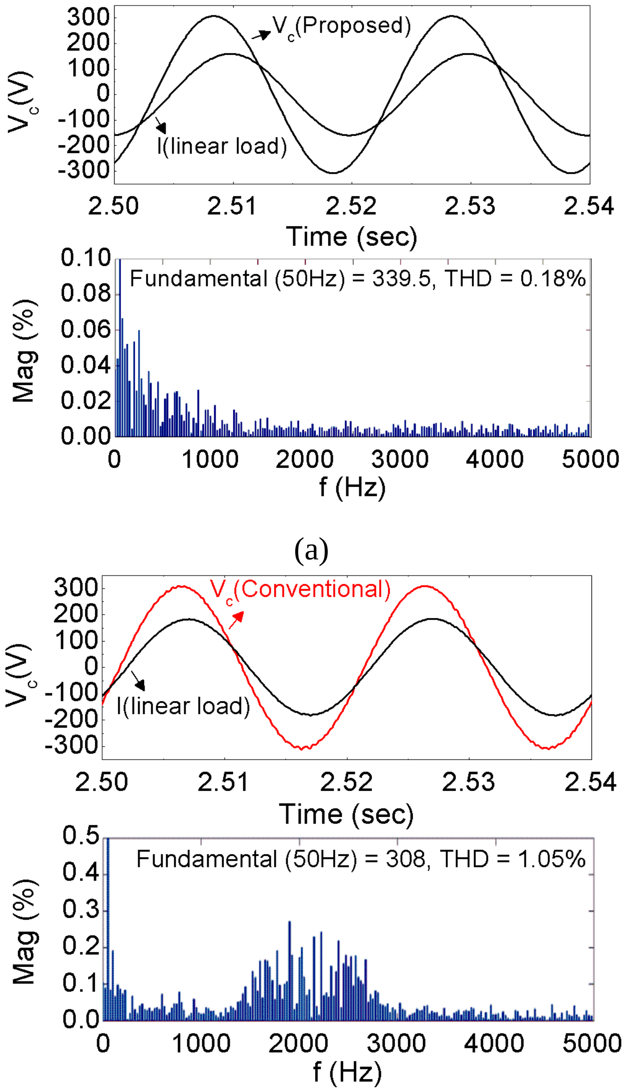

(a)

(b)

Fig.5-10 Comparison of voltage qualities under linear loads. (a) washout filter based method with the improved MPVC scheme, and (b) washout filter based method with the conventional MPVC scheme.

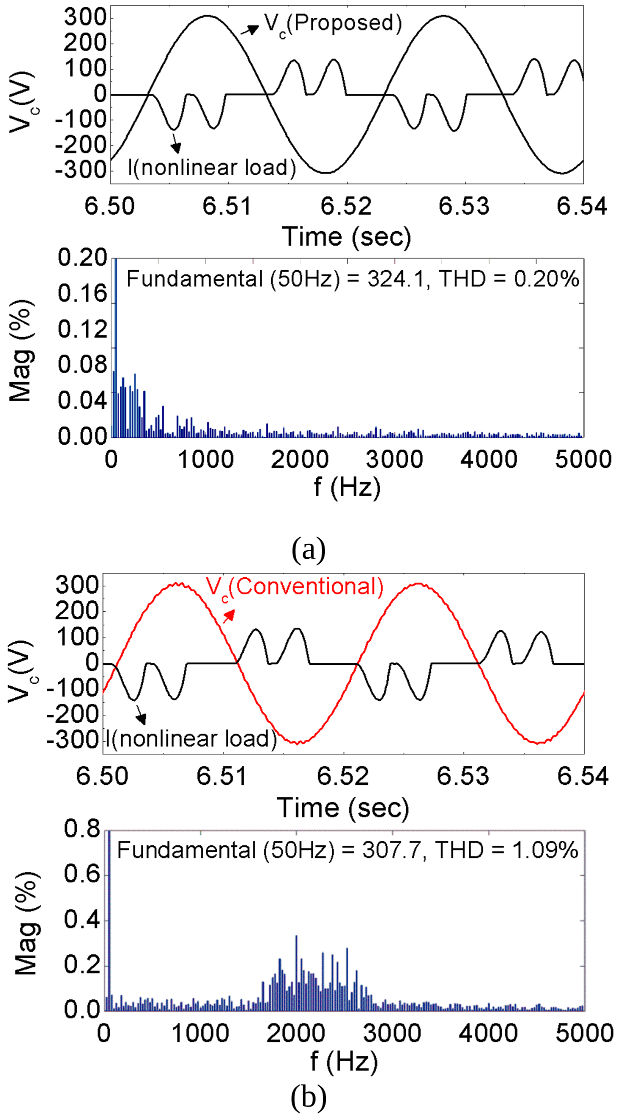

Fig.5-11 Comparison of voltage qualities under nonlinear loads. (a) washout filter based method with the improved MPVC scheme, (b) washout filter based method with the conventional MPVC scheme.

5.6.3 Comparison of Overall Controls

The values of the PCC voltage and frequency deviations at 2s as shown in Fig.5-8 and Fig.5-9 are listed in Table 5-3, which lists the improvements in a quantitative way between the proposed overall control and the traditional overall control.

Table 5-3 Voltage and frequency deviations

Overall control	PCC voltage deviation (ΔV)	Frequency deviation (ΔHz)
Traditional droop & CLC loops	-58.5080	-0.8330
Poposed washout filter & MPVC	-2.4411	-0.0033
ΔV=Actual PCC voltage – nominal voltage ΔHz=Actual frequency – nominal frequency		

As shown, using the traditional overall control (i.e. the traditional droop & CLC loops), the PCC voltage decreases by 58.5080V and the frequency decreases by 0.8330Hz. However, using the proposed overall control (i.e. the proposed washout filter & MPVC), the PCC voltage deviation and frequency deviation are mitigated dramatically to only 2.4411V and 0.0033Hz. This has proven the proposed overall control has a better voltage and frequency restoration capability.

5.6.4 Expansion with More DGs

Without loss of generality, four DGs are involved to test the effectiveness of the proposed scheme. The expansion of the MG is shown in Fig.5-1. For the DC side, four DGs are all equipped with the proposed new MPPC scheme with a 20 kW DC load supplied locally, and the fluctuating solar irradiation and ambient temperature are set the same as that in Subsection 5.6.1. For the AC side, four DGs are all connected to a local (50 kW, 0kVar) AC load and also a common (60 kW, 10 kVar) AC load using the proposed washout filter based method and MPVC scheme. The events with four DGs are given below in Table 5-4.

Table 5-4 Events with four DGs

Event	Operations	Time(s)
1	AC common load increases from (60kW, 10kVar) to (120kW, 20kVar)	1s
2	AC common load decreases from (120kW, 20kVar) to (60kW, 10kVar)	3s
3	DG4 is cut out suddenly	5s
4	DG4 is cut in suddenly	7s

Fig.5-12 provides the results with four DGs. As shown in Fig.5-12 (a) and (b), the load powers are shared equally with a plug-and-play feature. DG4 is switched out suddenly at 5s, while the remaining three DGs shoulder the loads timely and smoothly. At 7s, DG4 is again switched back into the MG, then the power sharing recovers with only small transient variations. The system frequency is shown in Fig.5-12(c), in which the frequency can be well restored to the rated values. The voltage magnitudes of the inverters are shown in Fig.5-12(d). The PCC voltage is plotted in Fig.5-12(e), in which the voltage is compensated.

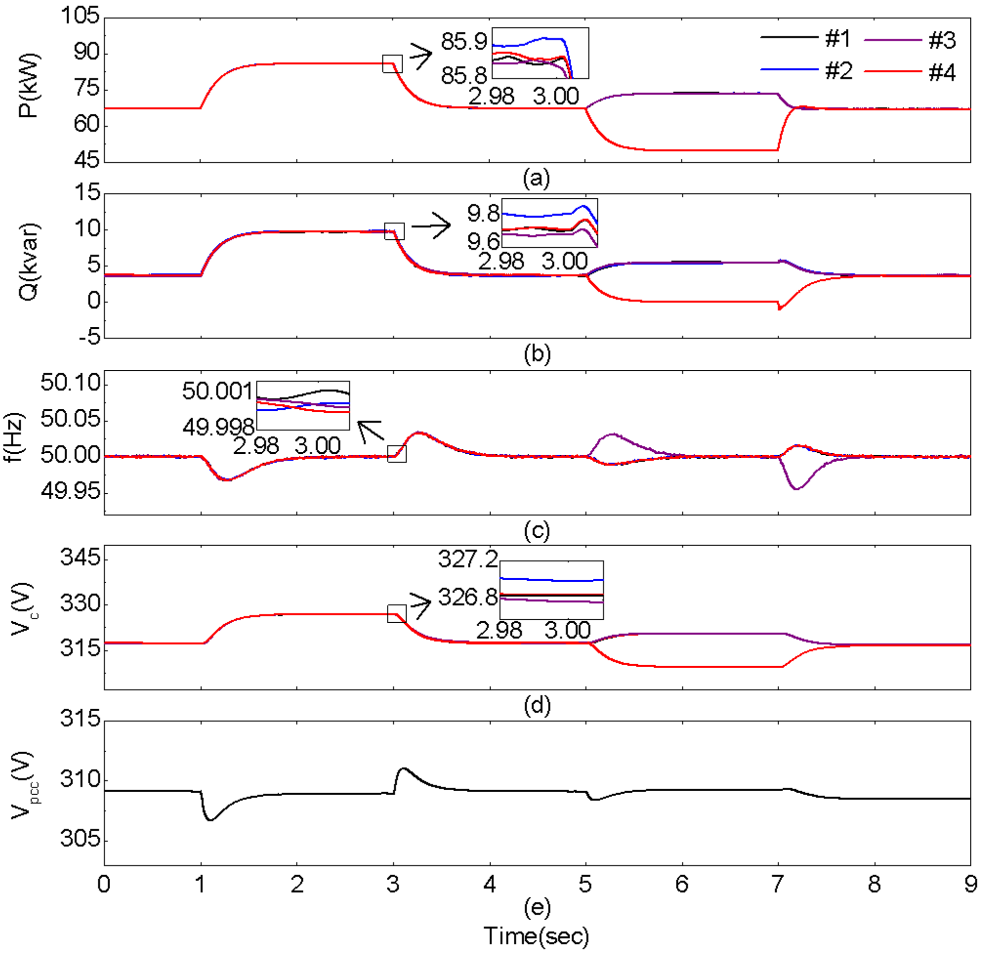

Fig.5-12 Performance of the proposed washout filter and MPVC scheme of Inverter#1, #2, #3 and #4. (a) active power, (b) reactive power, (c) frequency, (d) output voltage using washout filter method with PCC voltage compensation, (e) PCC voltage using washout filter method with PCC voltage compensation.

5.6.5 CHIL Test

The proposed washout filter based MPVC control scheme is further verified using the CHIL tests, the setup is shown in Fig.4-17. The testing principle is the same as that in Subsection 4.4.8, here it is omitted.

Fig.5-13 shows the performance of the proposed overall scheme when the AC common load increases from (40 kW, 10 kVar) to (80 kW, 20 kVar), i.e. the Event 1 in Table 5-2. It can be seen that the proportional power sharing is achieved while maintaining a stable high-quality voltage supply. In addition, Fig.5-14 shows the performance when the AC common load decreases from (80 kW, 20 kVar) to (40 kW, 10 kVar), i.e. the Event 3 in Table 5-2. For the two scenarios, the system provides a proper power sharing and a stable power supply in a safe and smooth way. Note that, since Inverter #2 presents a similar performance as Inverter #1, its results are omitted here.

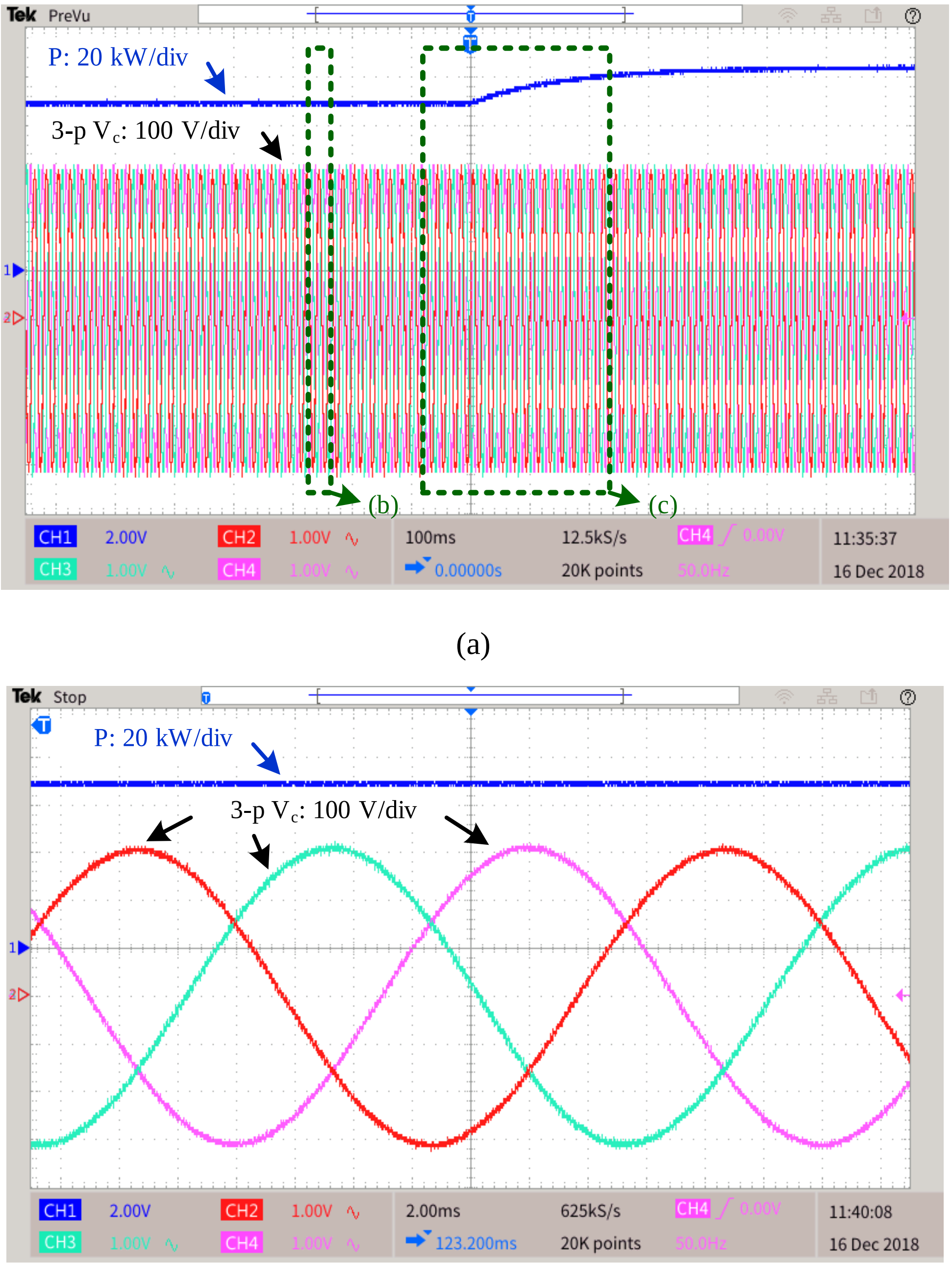

(a)

(b)

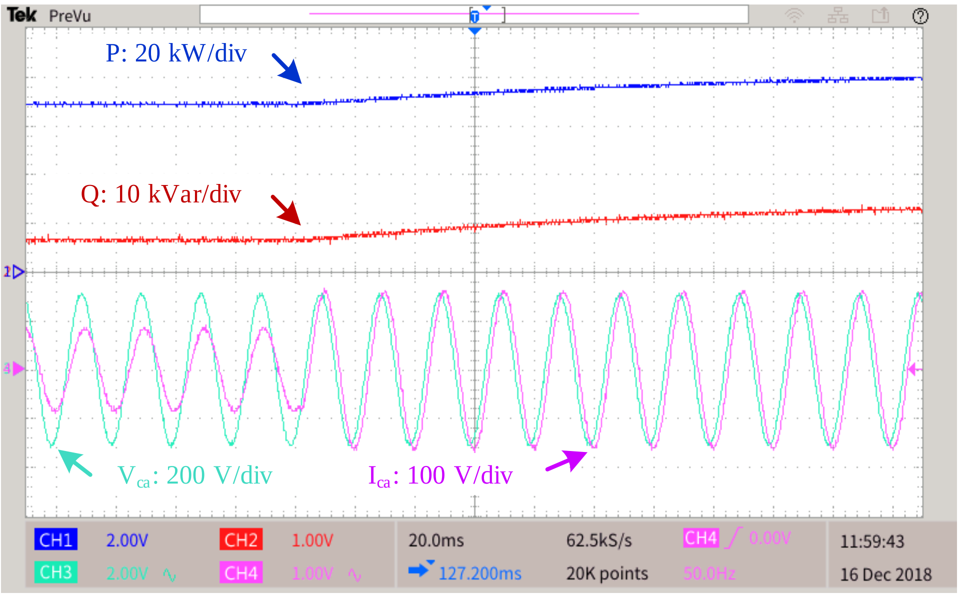

(c)

Fig.5-13 Performance of the proposed overall scheme when the common AC load is increased from (40kW, 10kVar) to (80kW, 20kVar). (a) active power and three-phase AC voltages, (b) zoom-in waveforms of active power and three-phase voltages before load changes, (c) zoom-in waveforms of active power, reactive power, phase-A voltage and phase-A current during load change transience.

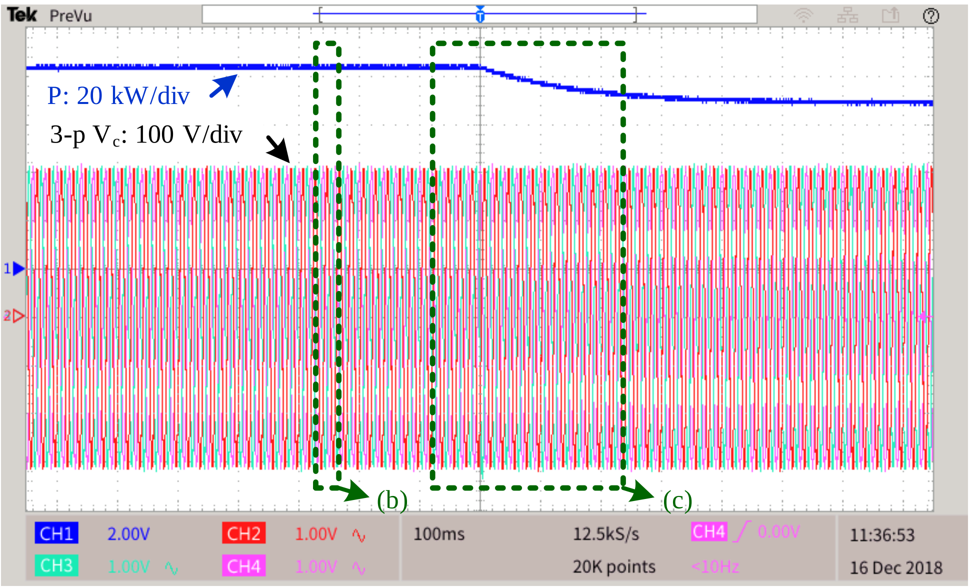

(a)

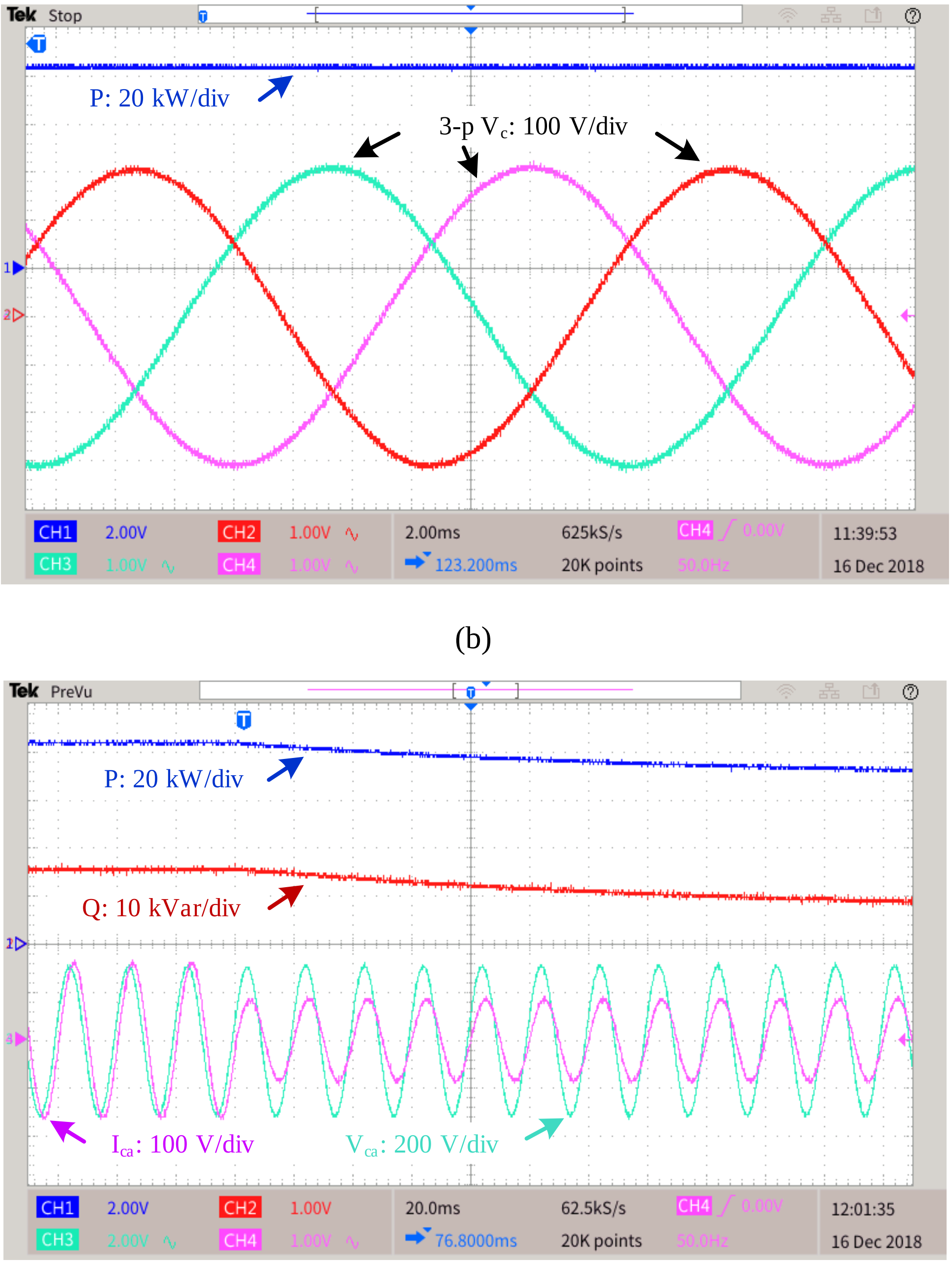

(b)

(c)

Fig.5-14 Performance of the proposed overall scheme when the common AC load is decreased from (80kW, 20kVar) to (40kW, 10kVar). (a) active power and three-phase AC voltages, (b) zoom-in waveforms of active power and three-phase voltages before load changes, (c) zoom-in waveforms of active power, reactive power, phase-A voltage and phase-A current during load change transience.

For comparison, the CHIL test by using traditional MPVC with the washout filter based power sharing method is also conducted, as shown in Fig.5-15. In contrast with Fig.5-14(b), the output voltage in Fig.5-15 presents more obvious oscillations, particularly around the voltage peaks. In another view, the results of the proposed overall scheme give out a clean and sinusoidal voltage output due to the strong voltage tracking capability taking into account the voltage changing trend.

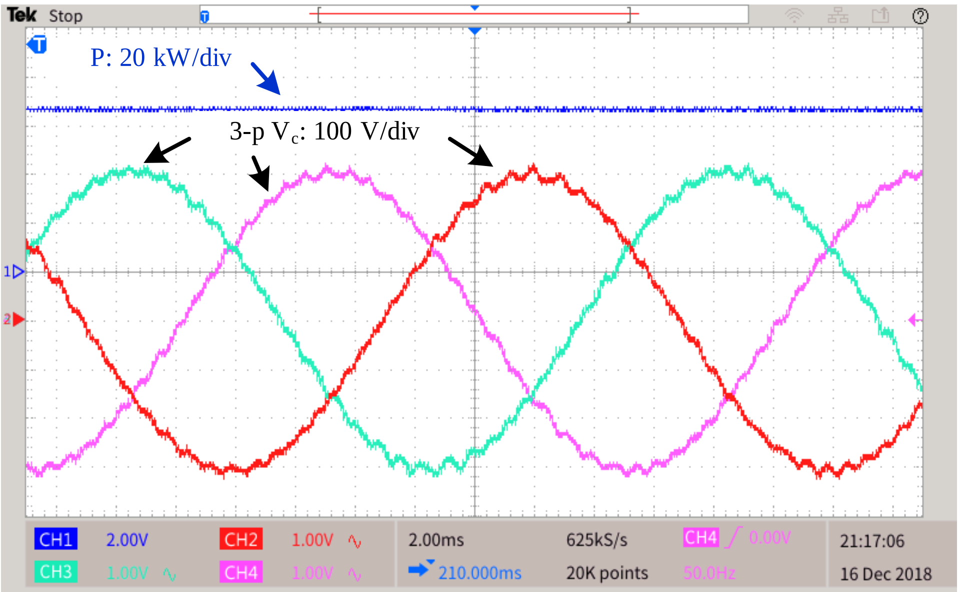

Fig.5-15 Performance of the traditional MPVC method & washout filter based power sharing method with common AC load at (40kW, 10kVar).

5.7 Summary

In this section, a new MPPC scheme for the bidirectional DC-DC converters, and an improved MPVC scheme for the inverters, as well as a washout filter based power sharing method with voltage compensation, are proposed. Specifically, on the DC side, using the new MPPC scheme to effectively smooth the PV output and maintain a stable DC-bus voltage. While on the AC side, a washout filter based power sharing method is adopted to enable properly proportional load sharing among inverters based on the power ratings, simultaneously the frequency and voltage deviations can be compensated. Moreover, the improved MPVC method considering the voltage changing trend is utilized to improve the AC voltage quality for linear or nonlinear loads. In contrast with the traditional control scheme, the proposed scheme provides an overall improvement, seeing a promising potential in MG applications with intermittent energies and variable loads.

Chapter 6 Conclusion and Future Work

6.1 Conclusion

This thesis has presented the MPC-based advanced control schemes of power converters for the MG applications with RESs and variable loads. To begin with, a brief review of the MGs with their general components, topology, and control methods has been stated. Then, CLC-based methods and MPC-based methods have been compared, together with their basic control structures and working principles. Next, the droop control method that is often adopted for the parallel operation of the DGs has been described. Objectively, the advantages and disadvantages of using MGs, CLC-based methods, MPC-based methods, and droop control methods have been discussed, respectively. In addition, the hierarchical control architecture of the MGs with three levels, i.e. primary control, secondary control, and tertiary control, has been introduced.

In this thesis, the bidirectional DC-DC converter and AC-DC interlinking converter are the pivotal components to realize the power conversion in MGs. Focused on the MPC-based methods, their general controls for the bidirectional DC-DC converters and AC-DC interlinking converters have been described. As for the various DGs which are frequently used in MGs, like the PV, WT, and ESS systems, their configurations and modelings have been described. Specifically, the hierarchical control of MGs, namely using the droop control method with CLC or MPC method for the primary control, using centralized PI-based f&V restoration for the secondary control, and using PI-based P&Q regulation for the tertiary control, has been presented.

For a PV-WT-ESS MG system, the MPC-based control schemes have been developed. That is, an MPCPC scheme involving current&power and an MPVPC scheme including voltage&power have been designed to control the bidirectional DC-DC converter of the ESS and the AC-DC interlinking converter, respectively. These schemes are utilized to smooth the RESs' outputs and support DC and AC buses. In the system level, an EMS is developed to enable smooth transitions among different operation modes. The validity of these schemes has been verified via considering real-world solar irradiation and wind profiles. Besides, the proposed schemes have also been compared with traditional CLC-based PI control schemes. It is proven that the proposed schemes present a better control effect.

For a grid-connected PV-ESS MG system, the MPPC scheme for the DC-DC bidirectional converter aiming to provide a stable and robust DC-bus voltage and also for the inverter allowing for a flexible power regulation and a stable AC power supply has been proposed. Using this scheme, the fluctuating PV output power has been smoothed, then the influence on the grid has been reduced. In addition, a voltage support service has been provided to compensate the voltage dips caused by the load changes. The effectiveness of the proposed MPPC scheme has been verified by various numerical simulation studies and CHIL tests.

A new MPPC scheme for the bidirectional DC-DC converters, and an improved MPVC scheme for the inverters, as well as a washout filter based power sharing method with voltage compensation, have been proposed for an islanded PV-ESS MG system. Specifically, on the DC side, using the proposed new MPPC scheme to effectively smooth the PV output and maintain the DC-bus voltage stable; on the AC side, a washout filter based power sharing method is incorporated to enable properly proportional load sharing among DGs, simultaneously mitigating the frequency and voltage deviations. Moreover, the MPVC scheme has been improved by considering the voltage changing trend to provide a better-quality AC voltage for both linear or nonlinear loads. Simulation cases and CHIL tests have indicated that the proposed schemes show an overall improvement compared with the traditional control schemes.

6.2 Future Work

Although the traditional CLC methods have been replaced by the MPC-based methods applied in various MG systems in existing researches, and MPC presents superior and competitive performances, the MPC algorithm also has some aspects that can be improved, no matter itself or its integration with other control methods, including (but not limited to):

1) Currently, as for the secondary and tertiary control levels of the MG system, MPC-based methods have been widely developed and reported. However, most of the existing studies in both academic and industrial domains about using MPC methods, on the one hand, merely concentrate on the control of power converters without considering the grid factors. While on the other hand, the grid factors about system-level power management have been investigated, but the converter features are neglected. Consequently, it is rare to see an MG system is totally controlled by all MPC methods on its three control levels. In the future, the potential benefits of applying MPC methods to each level of the MGs’ hierarchical control architecture will be investigated and explored.

2) Predictive model design or predictive equation formulation is essential and basic for the implementation of MPC methods. If there is no good quality and accuracy of the predictive model, control performances will be directly affected, thus designing a correct and suitable predictive model is always on the way. In this thesis, DC-DC and AC/DC converters’ predictive models are

developed, while there exist more complex converter topologies, for instance, multi-level converters[132] and matrix converter[133]. In the future, more and more complex converters will be designed for performance improvement or particular usage, so predictive model creation is necessary in order to better reflect their controllability and capability.

3) The cost function in a particular MPC-controlled system mirrors what is the control objective or which part is the control focus. For example, generally, in islanded MPC-controlled converters, the voltage is the control objective aiming to provide a constant voltage supply, while in grid-connected MPC-controlled converters, the active power and reactive power both are the control objectives aiming to provide a quantitative power flow. However, for a more specific purpose, such as harmonic minimization[134,135], computation burden optimization[136,137] and multilayer control[138,139], the cost function design will be a key issue to guarantee a superior control performance.

In addition, more than one term is usually involved in the cost function, different weights of these terms lead to different performances, which results in the necessity to carefully design weighting coefficients in MPC. Normally, experiential knowledge is needed for the setting of coefficients, which often is time-consuming and energy-consuming. In order to better assign the weighting coefficients skillfully and cleverly, intelligent algorithms can be adopted. For example, using fuzzy logic to optimize weighting coefficients[140,141], thus making the possible complex problems convenient, fast and efficient to solve.

4) Regarding the stability analysis of the MPC methods used in the field of power converters, at present, although Lyapunov method has been developed for MPC-controlled converters, the design and analysis are also insufficient[37,142]. Commonly, the most used way is to change the RLC

essential parameters in the controller settings while keeping the physical components unvaried, then to rerun the model repeatedly to evaluate the effect of these deviations on the system performance[121,124]. However, oftentimes, there is still a shortage of standard stability analysis of these MPC methods, and further about their combination of the droop control method.

5) Here, in this thesis, the hybrid MG system with both AC and DC buses has been studied. However, the research of pure DC MGs and related MPC methods are insufficient. It is known that PV systems and various ESSs are directly DC-interfaced, when they are connected with DC bus, fewer power conversion stages with possible efficiency improvement and more friendliness will be realized. Besides, DC-interfaced MGs enable plug-and-play functionality of simpler integration of DGs, i.e. the issue of controlling reactive power and frequency can also be neglected. In addition, the completion of MPC-controlled DC MGs will better facilitate the overall MPC control of the MG clusters which is more common in the future grid architecture.

6) The circulating current issue often exists in the parallel system. The large or disturbed circulating currents can make the circuit protector improperly trigger, potentially increasing the system power loss and reducing the device lifespan. Except using droop control methods or their improvements to regulate the circulating current, MPC methods can also be improved to alleviate this issue, e.g. adjusting the weighting factors of the cost function to suppress the circulating current[143]; or fixing the switching frequency to reduce the disturbed circulating currents[144], etc.

7) The following aspects also deserve deeper research, e.g. considering both the continuous current mode and discontinuous current mode of the MPC-controlled power converters, a more realistic partial-shaded PV model, a practical battery model taking into account recovery behavior and thermal

effect, system inertia investigation and the usage of virtual inertia, the possible instability issue of the coexistence of CLC and MPC, as well as the MPC application to engineers.

References

[1] J. Guerrero *et al.*, “Distributed generation: Toward a new energy paradigm,” *IEEE Ind. Electron. Mag.*, vol. 4, no. 1, pp. 52–64, 2010.

[2] H. R. Baghaee, M. Mirsalim, G. B. Gharehpetian, and H. A. Talebi, “A Decentralized Power Management and Sliding Mode Control Strategy for Hybrid AC/DC Microgrids including Renewable Energy Resources,” *IEEE Trans. Ind. Informatics*, vol. 3203, no. c, pp. 1–1, 2017.

[3] G. N. Tiwari and R. K. Mishra, *Advanced Renewable Energy Sources*. 2012.

[4] A. Castillo and D. F. Gayme, “Grid-scale energy storage applications in renewable energy integration: A survey,” *Energy Convers. Manag.*, vol. 87, pp. 885–894, 2014.

[5] J. M. Guerrero, J. C. Vasquez, J. Matas, L. G. De Vicuña, and M. Castilla, “Hierarchical control of droop-controlled AC and DC microgrids - A general approach toward standardization,” *IEEE Trans. Ind. Electron.*, vol. 58, no. 1, pp. 158–172, 2011.

[6] J. A. P. Lopes, C. L. Moreira, and A. G. Madureira, “Defining control strategies for analysing microgrids islanded operation,” *2005 IEEE Russ. Power Tech, PowerTech*, vol. 21, no. 2, pp. 916–924, 2005.

[7] N. Pogaku, M. Prodanović, and T. C. Green, “Modeling, analysis and testing of autonomous operation of an inverter-based microgrid,” *IEEE Trans. Power Electron.*, vol. 22, no. 2, pp. 613–625, 2007.

[8] P. C. Loh, D. Li, Y. K. Chai, and F. Blaabjerg, “Autonomous operation of hybrid microgrid with ac and dc subgrids,” *IEEE Trans. Power Electron.*, vol. 28, no. 5, pp. 2214–2223, 2013.

[9] A. Gupta, S. Doolla, and K. Chatterjee, “Hybrid AC-DC Microgrid: Systematic Evaluation of Control Strategies,” *IEEE Trans. Smart Grid*, vol. 9, no. 4, pp. 3830–3843, 2018.

[10] J. Rocabert, A. Luna, F. Blaabjerg, and P. Rodríguez, “Control of power converters in AC microgrids,” *IEEE Trans. Power Electron.*, vol. 27, no. 11, pp. 4734–4749, 2012.

[11] R. Zamora and A. K. Srivastava, “Controls for microgrids with storage: Review, challenges, and research needs,” *Renew. Sustain. Energy Rev.*, vol. 14, no. 7, pp. 2009–2018, 2010.

[12] K. S. Rajesh, S. S. Dash, R. Rajagopal, and R. Sridhar, “A review on control of ac microgrid,” *Renew. Sustain. Energy Rev.*, vol. 71, no. December 2016, pp. 814–819, 2017.

[13] M. C. Hatziargyriou N, Asano H, Iravani R, “Microgrids: an overview of ongoing research, development, and demonstration projects,” *IEEE Power Energ Mag*, vol. 5, no. 4, pp. 78–94, 2007.

[14] A. Hirsch, Y. Parag, and J. Guerrero, “Microgrids: A review of technologies, key drivers, and outstanding issues,” *Renew. Sustain. Energy Rev.*, vol. 90, no. April, pp. 402–411, 2018.

[15] S. A. Gorji, H. G. Sahebi, M. Ektesabi, and A. B. Rad, “Topologies and control schemes of bidirectional DC–DC power converters: An overview,” *IEEE Access*, vol. 7, pp. 117997–118019, 2019.

[16] S. Saxena and Y. V. Hote, “Decentralized PID load frequency control for perturbed multi-area power systems,” *Int. J. Electr. Power Energy Syst.*, vol. 81, pp. 405–415, 2016.

[17] D. G. H. Poh Chiang Loh, “Analysis of Multiloop Control Strategies for LC/CL/LCL-Filtered Voltage-Source and Current-Source Inverters,” *IEEE Trans. Ind. Appl.*, vol. 41, no. 2, pp. 644–654, 2005.

[18] U. B. Tayab, M. A. Bin Roslan, L. J. Hwai, and M. Kashif, “A review

of droop control techniques for microgrid," *Renew. Sustain. Energy Rev.*, vol. 76, no. March, pp. 717–727, 2017.

[19] H. Han, X. Hou, J. Yang, J. Wu, M. Su, and J. M. Guerrero, "Review of power sharing control strategies for islanding operation of AC microgrids," *IEEE Trans. Smart Grid*, vol. 7, no. 1, pp. 200–215, 2016.

[20] Y. Han, H. Li, P. Shen, E. A. A. Coelho, and J. M. Guerrero, "Review of Active and Reactive Power Sharing Strategies in Hierarchical Controlled Microgrids," *IEEE Trans. Power Electron.*, vol. 32, no. 3, pp. 2427–2451, 2017.

[21] Y.-D. Song, *Control of Nonlinear Systems via PI, PD and PID*. 2018.

[22] K. H. Ang, G. Chong, S. Member, and Y. Li, "PID control system analysis and design," *IEEE Control Syst.*, vol. 26, no. 1, pp. 32–41, 2006.

[23] Š. Kozák, "From PID to MPC: Control engineering methods development and applications," *2016 Cybern. Informatics, K I 2016 - Proc. 28th Int. Conf.*, pp. 1–7, 2016.

[24] J. M. Guerrero, L. G. de Vicuna, J. Matas, M. Castilla, and J. Miret, "A wireless controller to enhance dynamic performance of parallel inverters in distributed generation systems," *IEEE Trans. Power Electron.*, vol. 19, no. 5, pp. 1205–1213, 2004.

[25] H. Mahmood, D. Michaelson, and J. Jiang, "Accurate reactive power sharing in an islanded microgrid using adaptive virtual impedances," *IEEE Trans. Power Electron.*, vol. 30, no. 3, pp. 1605–1617, 2015.

[26] B. John, A. Ghosh, F. Zare, and S. Rajakaruna, "Improved control strategy for accurate load power sharing in an autonomous microgrid," *IET Gener. Transm. Distrib.*, vol. 11, no. 17, pp. 4384–4390, 2017.

[27] J. Zhang, J. Shu, J. Ning, L. Huang, and H. Wang, "Enhanced proportional power sharing strategy based on adaptive virtual

impedance in low-voltage networked microgrid," *IET Gener. Transm. Distrib.*, vol. 12, no. 11, pp. 2566–2576, 2018.

[28] X. Yang, H. Hu, Y. Ge, S. Aatif, Z. He, and S. Gao, "An Improved Droop Control Strategy for VSC-Based MVDC Traction Power Supply System," *IEEE Trans. Ind. Appl.*, vol. 54, no. 5, pp. 5173–5186, 2018.

[29] Y. Mi, H. Zhang, Y. Fu, C. Wang, P. C. Loh, and P. Wang, "Intelligent power sharing of dc isolated microgrid based on fuzzy sliding mode droop control," *IEEE Trans. Smart Grid*, vol. 10, no. 3, pp. 2396–2406, 2019.

[30] J. Zhou, M. J. Tsai, and P. T. Cheng, "Consensus-based Cooperative Droop Control for Accurate Reactive Power Sharing in Islanded AC Microgrid," *IEEE J. Emerg. Sel. Top. Power Electron.*, vol. 8, no. 2, pp. 1108–1116, 2020.

[31] M. Gao, M. Chen, B. Zhao, B. Li and Z. Qian, "Design of Control System for Smooth Mode-transfer of Grid-tied Mode and Islanding Mode in Microgrid," *IEEE Trans. Power Electron.*, vol. 35, no. 6, pp. 6419-6435, 2020.

[32] T. Geyer, "Model predictive direct current control for multi-level converters," *2010 IEEE Energy Convers. Congr. Expo. ECCE 2010 - Proc.*, pp. 4305–4312, 2010.

[33] J. R. D. Frejo and E. F. Camacho, "Global versus local MPC algorithms in freeway traffic control with ramp metering and variable speed limits," *IEEE Trans. Intell. Transp. Syst.*, vol. 13, no. 4, pp. 1556–1565, 2012.

[34] J. Rodríguez, R. M. Kennel, J. R. Espinoza, M. Trincado, C. A. Silva, and C. A. Rojas, "High-performance control strategies for electrical drives: An experimental assessment," *IEEE Trans. Ind. Electron.*, vol. 59, no. 2, pp. 812–820, 2012.

[35] C. E. García, D. M. Prett, and M. Morari, “Model predictive control: Theory and practice-A survey,” *Automatica*, vol. 25, no. 3, pp. 335–348, 1989.

[36] S. Kouro, P. Cortés, R. Vargas, U. Ammann, and J. Rodríguez, “Model predictive control - A simple and powerful Method to control power converters,” *IEEE Trans. Ind. Electron.*, vol. 56, no. 6, pp. 1826–1838, 2009.

[37] J. Rodriguez *et al.*, “State of the art of finite control set model predictive control in power electronics,” *IEEE Trans. Ind. Informatics*, vol. 9, no. 2, pp. 1003–1016, 2013.

[38] S. Vazquez *et al.*, “Model predictive control: A review of its applications in power electronics,” *IEEE Ind. Electron. Mag.*, vol. 8, no. 1, pp. 16–31, 2014.

[39] J. Hu, J. Zhu, and D. G. Dorrell, “In-depth study of direct power control strategies for power converters,” *IET Power Electron.*, vol. 7, no. 7, pp. 1810–1820, 2014.

[40] P. Cortés, M. P. Kazmierkowski, R. M. Kennel, D. E. Quevedo, and J. Rodriguez, “Predictive control in power electronics and drives,” *IEEE Trans. Ind. Electron.*, vol. 55, no. 12, pp. 4312–4324, 2008.

[41] S. Vazquez, J. Rodriguez, M. Rivera, L. G. Franquelo, and M. Norambuena, “Model Predictive Control for Power Converters and Drives: Advances and Trends,” *IEEE Trans. Ind. Electron.*, vol. 64, no. 2, pp. 935–947, 2017.

[42] J. Hu, J. Zhu, G. Lei, G. Platt, and D. G. Dorrell, “Multi-objective model-predictive control for high-power converters,” *IEEE Trans. Energy Convers.*, vol. 28, no. 3, pp. 652–663, 2013.

[43] M. W. Khan and J. Wang, “The research on multi-agent system for microgrid control and optimization,” *Renew. Sustain. Energy Rev.*, vol.

80, no. September 2016, pp. 1399–1411, 2017.

[44] M. Pourbehzadi, T. Niknam, J. Aghaei, G. Mokryani, M. Shafie-khah, and J. P. S. Catalão, “Optimal operation of hybrid AC/DC microgrids under uncertainty of renewable energy resources: A comprehensive review,” *Int. J. Electr. Power Energy Syst.*, vol. 109, no. January, pp. 139–159, 2019.

[45] A. Mohammed, S. S. Refaat, S. Bayhan, and H. Abu-Rub, “AC Microgrid Control and Management Strategies: Evaluation and Review,” *IEEE Power Electron. Mag.*, vol. 6, no. 2, pp. 18–31, 2019.

[46] S. Wang, Z. Liu, J. Liu, R. An, and M. Xin, “Breaking the boundary: A droop and master-slave hybrid control strategy for parallel inverters in islanded microgrids,” *2017 IEEE Energy Convers. Congr. Expo. ECCE 2017*, vol. 2017-Janua, pp. 3345–3352, 2017.

[47] L. Meng *et al.*, “Review on Control of DC Microgrids and Multiple Microgrid Clusters,” *IEEE J. Emerg. Sel. Top. Power Electron.*, vol. 5, no. 3, pp. 928–948, 2017.

[48] Y. W. Li and C. N. Kao, “An accurate power control strategy for power-electronics-interfaced distributed generation units operating in a low-voltage multibus microgrid,” *IEEE Trans. Power Electron.*, vol. 24, no. 12, pp. 2977–2988, 2009.

[49] A. Bidram and A. Davoudi, “Hierarchical structure of microgrids control system,” *IEEE Trans. Smart Grid*, vol. 3, no. 4, pp. 1963–1976, 2012.

[50] D. E. Olivares *et al.*, “Trends in microgrid control,” *IEEE Trans. Smart Grid*, vol. 5, no. 4, pp. 1905–1919, 2014.

[51] J. M. Guerrero, J. Matas, L. G. De Vicuña, N. Berbel, and J. Sosa, “Wireless-control strategy for parallel operation of distributed generation inverters,” *IEEE Int. Symp. Ind. Electron.*, vol. II, no. 5, pp.

845–850, 2005.

[52] J. Matas, M. Castilla, L. G. De Vicuña, J. Miret, and J. C. Vasquez, “Virtual impedance loop for droop-controlled single-phase parallel inverters using a second-order general-integrator scheme,” *IEEE Trans. Power Electron.*, vol. 25, no. 12, pp. 2993–3002, 2010.

[53] J. Hu, J. Zhu, D. G. Dorrell, and J. M. Guerrero, “Virtual flux droop method - A new control strategy of inverters in microgrids,” *IEEE Trans. Power Electron.*, vol. 29, no. 9, pp. 4704–4711, 2014.

[54] Y. Zhu, F. Zhuo, F. Wang, B. Liu, and Y. Zhao, “A Wireless Load Sharing Strategy for Islanded Microgrid Based on Feeder Current Sensing,” *IEEE Trans. Power Electron.*, vol. 30, no. 12, pp. 6706–6719, 2015.

[55] K. O. Oureilidis and C. S. Demoulias, “A decentralized impedance-based adaptive droop method for power loss reduction in a converter-dominated islanded microgrid,” *Sustain. Energy, Grids Networks*, vol. 5, pp. 39–49, 2016.

[56] B. Wei, J. M. Guerrero, J. C. Vásquez, and X. Guo, “A Circulating-Current Suppression Method for Parallel-Connected Voltage-Source Inverters with Common DC and AC Buses,” *IEEE Trans. Ind. Appl.*, vol. 53, no. 4, pp. 3758–3769, 2017.

[57] Y. Sun *et al.*, “An f-p/q droop control in cascaded-type microgrid,” *IEEE Trans. Power Syst.*, vol. 33, no. 1, pp. 1136–1138, 2018.

[58] M. S. Golsorkhi, Q. Shafiee, D. D. C. Lu, and J. M. Guerrero, “Distributed Control of Low-Voltage Resistive AC Microgrids,” *IEEE Trans. Energy Convers.*, vol. 34, no. 2, pp. 573–584, 2019.

[59] R. J. Wai, Q. Q. Zhang, and Y. Wang, “A Novel Voltage Stabilization and Power Sharing Control Method Based on Virtual Complex Impedance for an Off-Grid Microgrid,” *IEEE Trans. Power Electron.*,

vol. 34, no. 2, pp. 1863–1880, 2019.

[60] M. Savaghebi, A. Jalilian, J. C. Vasquez, and J. M. Guerrero, “Secondary control scheme for voltage unbalance compensation in an Islanded droop-controlled microgrid,” *IEEE Trans. Smart Grid*, vol. 3, no. 2, pp. 797–807, 2012.

[61] A. Bidram, A. Davoudi, F. L. Lewis, and J. M. Guerrero, “Distributed cooperative secondary control of microgrids using feedback linearization,” *IEEE Trans. Power Syst.*, vol. 28, no. 3, pp. 3462–3470, 2013.

[62] Q. Shafiee, J. M. Guerrero, and J. C. Vasquez, “Distributed secondary control for islanded microgrids-a novel approach,” *IEEE Trans. Power Electron.*, vol. 29, no. 2, pp. 1018–1031, 2014.

[63] J. W. Simpson-Porco, Q. Shafiee, F. Dorfler, J. C. Vasquez, J. M. Guerrero, and F. Bullo, “Secondary Frequency and Voltage Control of Islanded Microgrids via Distributed Averaging,” *IEEE Trans. Ind. Electron.*, vol. 62, no. 11, pp. 7025–7038, 2015.

[64] P. Wang, X. Lu, X. Yang, W. Wang, and D. Xu, “An Improved Distributed Secondary Control Method for DC Microgrids with Enhanced Dynamic Current Sharing Performance,” *IEEE Trans. Power Electron.*, vol. 31, no. 9, pp. 6658–6673, 2016.

[65] M. H. Andishgar, E. Gholipour, and R.-A. Hooshmand, “Improved secondary control for optimal total harmonic distortion compensation of parallel connected DGs in islanded microgrids,” *IET Smart Grid*, vol. 2, no. 1, pp. 115–122, 2019.

[66] B. Wei, Y. Gui, S. Trujillo, J. M. Guerrero, and J. C. Vasquez, “Distributed Average Integral Secondary Control for Modular UPS Systems-Based Microgrids,” *IEEE Trans. Power Electron.*, vol. 34, no. 7, pp. 6922–6936, 2019.

[67] L. Meng, F. Tang, M. Savaghebi, J. C. Vasquez, and J. M. Guerrero, “Tertiary control of voltage unbalance compensation for optimal power quality in islanded microgrids,” *IEEE Trans. Energy Convers.*, vol. 29, no. 4, pp. 802–815, 2014.

[68] L. Citores, C. Corchero, and F. J. Heredia, “A stochastic programming model for the tertiary control of microgrids,” *Int. Conf. Eur. Energy Mark. EEM*, vol. 2015-Augus, pp. 1–6, 2015.

[69] S. Moayedi and A. Davoudi, “Distributed Tertiary Control of DC Microgrid Clusters,” *IEEE Trans. Power Electron.*, vol. 31, no. 2, pp. 1717–1733, 2017.

[70] S. R. Mudaliyar, S. Mishra, and R. K. Sharma, “Tertiary load voltage control in an interconnected DC microgrid with energy hub,” *2017 7th Int. Conf. Power Syst. ICPS 2017*, pp. 765–770, 2018.

[71] F. Delfino, G. Ferro, M. Robba, and M. Rossi, “An architecture for the optimal control of tertiary and secondary levels in small-size islanded microgrids,” *Int. J. Electr. Power Energy Syst.*, vol. 103, no. April, pp. 75–88, 2018.

[72] C. Ahumada, R. Cárdenas, D. Sáez, and J. M. Guerrero, “Secondary Control Strategies for Frequency Restoration in Islanded Microgrids With Consideration of Communication Delays,” *IEEE Trans. Smart Grid*, vol. 7, no. 3, pp. 1430–1441, 2016.

[73] G. Lou, W. Gu, Y. Xu, M. Cheng, and W. Liu, “Distributed MPC-Based Secondary Voltage Control Scheme for Autonomous Droop-Controlled Microgrids,” *IEEE Trans. Sustain. Energy*, vol. 8, no. 2, pp. 792–804, 2017.

[74] X. Wang, Q. Zhao, B. He, Y. Wang, J. Yang, and X. Pan, “Load frequency control in multiple microgrids based on model predictive control with communication delay,” *J. Eng.*, vol. 2017, no. 13, pp.

1851–1856, 2017.

[75] W. C. Clarke, C. Manzie, and M. J. Brear, "An economic MPC approach to microgrid control," in *2016 Australian Control Conference, AuCC 2016*, pp. 276–281, 2017.

[76] Y. Zheng, S. Li, and R. Tan, "Distributed Model Predictive Control for On-Connected Microgrid Power Management," *IEEE Trans. Control Syst. Technol.*, vol. 26, no. 3, pp. 1028–1039, 2018.

[77] Y. Jia, Z. Y. Dong, C. Sun, and G. Chen, "Distributed Economic Model Predictive Control for a Wind-Photovoltaic-Battery Microgrid Power System," *IEEE Trans. Sustain. Energy*, vol. 11, no. 2, pp. 1089–1099, 2020.

[78] F. Garcia-Torres, C. Bordons, and M. A. Ridao, "Optimal economic schedule for a network of microgrids with hybrid energy storage system using distributed model predictive control," *IEEE Trans. Ind. Electron.*, vol. 66, no. 3, pp. 1919–1929, 2019.

[79] X. Yang, Y. Zhang, H. He, S. Ren, and G. Weng, "Real-Time Demand Side Management for a Microgrid Considering Uncertainties," *IEEE Trans. Smart Grid*, vol. 10, no. 3, pp. 3401–3414, 2019.

[80] P. Kou, D. Liang, and L. Gao, "Distributed Coordination of Multiple PMSGs in an Islanded DC Microgrid for Load Sharing," *IEEE Trans. Energy Convers.*, vol. 32, no. 2, pp. 471–485, 2017.

[81] T. Morstyn, B. Hredzak, R. P. Aguilera, and V. G. Agelidis, "Model Predictive Control for Distributed Microgrid Battery Energy Storage Systems," *IEEE Trans. Control Syst. Technol.*, vol. 26, no. 3, pp. 1107–1114, 2018.

[82] P. Vaclavek and P. Blaha, "PMSM model discretization for model predictive control algorithms," *2013 IEEE/SICE Int. Symp. Syst. Integr. SII 2013*, no. 3, pp. 13–18, 2013.

[83] G.C. Goodwin, S.F. Graebe, “Control Systems Design,” in *Control System Design*, pp. 338, 2000.

[84] J. Hu, J. Zhu, and D. G. Dorrell, “Model predictive control of grid-connected inverters for PV systems with flexible power regulation and switching frequency reduction,” *IEEE Trans. Ind. Appl.*, vol. 51, no. 1, pp. 587–594, 2015.

[85] M. E. Khodayar, M. R. Feizi, and A. Vafamehr, “Solar photovoltaic generation: Benefits and operation challenges in distribution networks,” *Electr. J.*, vol. 32, no. 4, pp. 50–57, 2019.

[86] B. Subudhi and R. Pradhan, “A comparative study on maximum power point tracking techniques for photovoltaic power systems,” *IEEE Trans. Sustain. Energy*, vol. 4, no. 1, pp. 89–98, 2013.

[87] H. Patel and V. Agarwal, “MATLAB-based modeling to study the effects of partial shading on PV array characteristics,” *IEEE Trans. Energy Convers.*, vol. 23, no. 1, pp. 302–310, 2008.

[88] T. T. Nguyen, H. W. Kim, G. H. Lee, and W. Choi, “Design and implementation of the low cost and fast solar charger with the rooftop PV array of the vehicle,” *Sol. Energy*, vol. 96, pp. 83–95, 2013.

[89] T. Esram and P. L. Chapman, “Comparison of photovoltaic array maximum power point tracking techniques,” *IEEE Trans. Energy Convers.*, vol. 22, no. 2, pp. 439–449, 2007.

[90] N. Karami, N. Moubayed, and R. Outbib, “General review and classification of different MPPT Techniques,” *Renew. Sustain. Energy Rev.*, vol. 68, no. October 2016, pp. 1–18, 2017.

[91] J. Hu, Y. Shan, Y. Xu, and J. M. Guerrero, “A coordinated control of hybrid ac/dc microgrids with PV-wind-battery under variable generation and load conditions,” *Int. J. Electr. Power Energy Syst.*, vol. 104, no. July 2018, pp. 583–592, 2019.

[92] I. V. Banu, R. Beniuga, and M. Istrate, “Comparative analysis of the perturb-and-observe and incremental conductance MPPT methods,” in *2013 - 8th International Symposium on Advanced Topics in Electrical Engineering, ATEE 2013*, 2013.

[93] U. Cali, N. Erdogan, S. Kucuksari, and M. Argin, “TECHNO-ECONOMIC analysis of high potential offshore wind farm locations in Turkey,” *Energy Strateg. Rev.*, vol. 22, pp. 325–336, 2018.

[94] Z. Yushan and R. E. N. Xiaojing, “Analysis of Current Situation and Prospect of Wind Power Energy Cooperation Between China and Jordan Under ‘ One Belt and One Road ’ Initiative,” *Can. Soc. Sci.*, vol. 15, no. 6, pp. 1–4, 2019.

[95] M. E. Haque, M. Negnevitsky, and K. M. Muttaqi, “A novel control strategy for a variable-speed wind turbine with a permanent-magnet synchronous generator,” *IEEE Trans. Ind. Appl.*, vol. 46, no. 1, pp. 331–339, 2010.

[96] T. Tafticht, K. Agbossou, A. Chériti, and M. L. Doumbia, “Output power maximization of a permanent magnet synchronous generator based stand-alone wind turbine,” *IEEE Int. Symp. Ind. Electron.*, vol. 3, no. 4, pp. 2412–2416, 2006.

[97] E. Koutroulis and K. Kalaitzakis, “Design of a maximum power tracking system for wind-energy-conversion applications,” *IEEE Trans. Ind. Electron.*, vol. 53, no. 2, pp. 486–494, 2006.

[98] X. Liu, P. Wang, and P. C. Loh, “A hybrid AC/DC microgrid and its coordination control,” *IEEE Trans. Smart Grid*, vol. 2, no. 2, pp. 278–286, 2011.

[99] A. Khaligh and Z. Li, “Battery, ultracapacitor, fuel cell, and hybrid energy storage systems for electric, hybrid electric, fuel cell, and plug-in hybrid electric vehicles: State of the art,” *IEEE Trans. Veh. Technol.*,

vol. 59, no. 6, pp. 2806–2814, 2010.

[100] M. T. Lawder *et al.*, “Battery energy storage system (BESS) and battery management system (BMS) for grid-scale applications,” *Proc. IEEE*, vol. 102, no. 6, pp. 1014–1030, 2014.

[101] A. Merabet, K. Tawfique Ahmed, H. Ibrahim, R. Beguenane, and A. M. Y. M. Ghias, “Energy Management and Control System for Laboratory Scale Microgrid Based Wind-PV-Battery,” *IEEE Trans. Sustain. Energy*, vol. 8, no. 1, pp. 145–154, 2017.

[102] “Generic battery model - Simulink - MathWorks.” [Online]. Available: https://www.mathworks.com/help/physmod/sps/powersys/ref/battery.html.

[103] O. Tremblay, “Experimental Validation of a Battery Dynamic Model for EV Applications Experimental Validation of a Battery Dynamic Model for EV Applications,” *24th Int. Batter. Hybrid Fuel Cell Electr. Veh. Symp. Exhib. 2009, EVS 24*, vol. 3, no. October, pp. 289–298, 2015.

[104] J. M. Guerrero, M. Chandorkar, T. L. Lee, and P. C. Loh, “Advanced control architectures for intelligent microgridspart i: Decentralized and hierarchical control,” *IEEE Trans. Ind. Electron.*, vol. 60, no. 4, pp. 1254–1262, 2013.

[105] R. Scattolini, “Architectures for distributed and hierarchical Model Predictive Control – A review,” *J. Process Control*, vol. 19, no. 5, pp. 723–731, May 2009.

[106] K. Schmidt and C. Breindl, “Maximally permissive hierarchical control of decentralized discrete event systems,” *IEEE Trans. Automat. Contr.*, vol. 56, no. 4, pp. 723–737, 2011.

[107] Y. W. Li, “Control and resonance damping of voltage-source and current-source converters with LC filters,” *IEEE Trans. Ind. Electron.*,

vol. 56, no. 5, pp. 1511–1521, 2009.

[108] Y. Shan, J. Hu, Z. Li, and J. M. Guerrero, “A Model Predictive Control for Renewable Energy Based AC Microgrids Without Any PID Regulators,” *IEEE Trans. Power Electron.*, vol. 33, no. 11, pp. 9122–9126, 2018.

[109] A. J. Babqi and A. H. Etemadi, “MPC-based microgrid control with supplementary fault current limitation and smooth transition mechanisms,” *IET Gener. Transm. Distrib.*, vol. 11, no. 9, pp. 2164–2172, 2017.

[110] “Supply Rules, Standards & Policies - Limited, HK Electric Investments.” [Online]. Available: https://www.hkelectric.com/zh/customer-services/rules-standards-policies.

[111] P. N. Kanna and B. Meenakshi, “Analysis and design of DC-DC/AC non isolated cuk converter using sliding mode controller,” in *IEEE International Conference on Circuit, Power and Computing Technologies, ICCPCT 2015*, 2015.

[112] D. E. Quevedo, R. P. Aguilera, M. A. Pérez, P. Cortes, and R. Lizana, “Model predictive control of an AFE rectifier with dynamic references,” *IEEE Trans. Power Electron.*, vol. 27, no. 7, pp. 3128–3136, 2012.

[113] Y. Shan, J. Hu, K. W. Chan, Q. Fu, and J. M. Guerrero, “Model Predictive Control of Bidirectional DC-DC Converters and AC/DC Interlinking Converters - A New Control Method for PV-Wind-Battery Microgrids,” *IEEE Trans. Sustain. Energy*, vol. 10, no. 4, pp. 1823–1833, 2018.

[114] A. Silani and M. J. Yazdanpanah, “Distributed Optimal Microgrid Energy Management With Considering Stochastic Load,” *IEEE Trans.*

Sustain. Energy, vol. 10, no. 2, pp. 729–737, 2019.

[115] F. Yang, X. Feng, and Z. Li, “Advanced Microgrid Energy Management System for Future Sustainable and Resilient Power Grid,” *IEEE Trans. Ind. Appl.*, vol. 55, no. 2, pp. 1–1, 2019.

[116] J. Hu, Y. Xu, K. W. Cheng, and J. M. Guerrero, “A model predictive control strategy of PV-Battery microgrid under variable power generations and load conditions,” *Appl. Energy*, vol. 221, no. February, pp. 195–203, 2018.

[117] “Lamma Wind Power Station.” [Online]. Available: https://www.hkelectric.com/en/our-operations/lamma-wind-power-station.

[118] Y. Shan, J. Hu, and J. M. Guerrero, “A Model Predictive Power Control Method for PV and Energy Storage Systems with Voltage Support Capability,” *IEEE Trans. Smart Grid*, pp. 1–1, 2019.

[119] N. Maryam Hashemi and V. Agelidis, “Evaluation of voltage regulation mitigation methods due to high penetration of PV generation in residential areas,” in *Proceedings of 2013 International Conference on Renewable Energy Research and Applications, ICRERA 2013*, pp. 1180–1189, 2013.

[120] M. Zeraati, S. Member, M. Esmail, H. Golshan, and J. M. Guerrero, “Distributed Control of Battery Energy Storage Systems for Voltage Regulation in Distribution Networks With High PV Penetration,” *IEEE Trans. Smart Grid*, vol. 9, no. 4, pp. 3582–3593, 2018.

[121] T. Dragicevic, “Model Predictive Control of Power Converters for Robust and Fast Operation of AC Microgrids,” *IEEE Trans. Power Electron.*, vol. 33, no. 7, pp. 6304–6317, 2018.

[122] P. Cortes, J. Rodriguez, C. Silva, and A. Flores, “Delay compensation in model predictive current control of a three-phase inverter,” *IEEE*

Trans. Ind. Electron., vol. 59, no. 2, pp. 1323–1325, 2012.

[123] J. Hu, J. Zhu, and D. G. Dorrell, “Model predictive control of inverters for both islanded and grid-connected operations in renewable power generations,” *IET Renew. Power Gener.*, vol. 8, no. 3, pp. 240–248, 2014.

[124] P. A. and M. K. P. CortÉs, J. RodrÍguez, “Direct Power Control of an AFE Using Predictive Control,” *IEEE Trans. Power Electron.*, vol. 23, no. 5, pp. 2516–2523, 2008.

[125] J. Wang, C. Jin, and P. Wang, “A Uniform Control Strategy for the Interlinking Converter in Hierarchical Controlled Hybrid AC/DC Microgrids,” *IEEE Trans. Ind. Electron.*, vol. 65, no. 8, pp. 6188–6197, 2018.

[126] M. Y. and A. Mehrizi-Sani, “Washout Filter-Based Power Sharing,” *IEEE Trans. Smart Grid*, vol. 7, no. 2, pp. 967–968, 2016.

[127] Y. Han, H. Li, L. Xu, X. Zhao, and J. M. Guerrero, “Analysis of Washout Filter-Based Power Sharing Strategy-An Equivalent Secondary Controller for Islanded Microgrid Without LBC Lines,” *IEEE Trans. Smart Grid*, vol. 9, no. 5, pp. 4061–4076, 2018.

[128] Y. Shan, J. Hu, M. Liu, J. Zhu, and J. M. Guerrero, “Model Predictive Voltage and Power Control of Islanded PV-Battery Microgrids with Washout Filter Based Power Sharing Strategy,” *IEEE Trans. Power Electron.*, vol. 35, no. 2, pp. 1227–1238, 2020.

[129] M. A. Hassouneh, H. C. Lee, and E. H. Abed, “Washout filters in feedback control: Benefits, limitations and extensions,” *Proc. Am. Control Conf.*, vol. 5, pp. 3950–3955, 2004.

[130] J. He and Y. W. Li, “An enhanced microgrid load demand sharing strategy,” *IEEE Trans. Power Electron.*, vol. 27, no. 9, pp. 3984–3995, 2012.

[131] D. Ritzmann, P. S. Wright, W. Holderbaum, and B. Potter, “A Method for Accurate Transmission Line Impedance Parameter Estimation,” *IEEE Trans. Instrum. Meas.*, vol. 65, no. 10, pp. 2204–2213, 2016.

[132] M. S. Manoharan, A. Ahmed, and J.-H. Park, “An Improved Model Predictive Controller for 27-level Asymmetric Cascaded Inverter Applicable in High Power PV Grid-Connected Systems,” *IEEE J. Emerg. Sel. Top. Power Electron.*, pp. 1–1, 2019.

[133] J. Lei, S. Feng, P. Wheeler, B. Zhou, and J. Zhao, “Steady-State Error Suppression and Simplified Implementation of Direct Source Current Control for Matrix Converter with Model Predictive Control,” *IEEE Trans. Power Electron.*, vol. 35, no. 3, pp. 3183–3194, 2020.

[134] C. Xue, L. Ding, Y. Li, and N. R. Zargari, “Improved Model Predictive Control for High-Power Current-Source Rectifiers Under Normal and Distorted Grid Conditions,” *IEEE Trans. Power Electron.*, vol. 35, no. 5, pp. 4588–4601, 2020.

[135] H. Gao, B. Wu, D. Xu, R. P. Aguilera, and P. Acuna, “Model Predictive Switching Pattern Control for Current-Source Converters with Space-Vector-Based Selective Harmonic Elimination,” *IEEE Trans. Power Electron.*, vol. 32, no. 8, pp. 6558–6569, 2017.

[136] A. Bahrami, M. Norambuena, M. Narimani, and J. Rodriguez, “Model Predictive Current Control of a Seven-Level Inverter with Reduced Computational Burden,” *IEEE Trans. Power Electron.*, vol. 35, no. 6, pp. 5729–5740, 2020.

[137] B. Gutierrez and S. S. Kwak, “Modular Multilevel Converters (MMCs) Controlled by Model Predictive Control with Reduced Calculation Burden,” *IEEE Trans. Power Electron.*, vol. 33, no. 11, pp. 9176–9187, 2018.

[138] S. Zhang and U. K. Madawala, “A Hybrid Model Predictive Multilayer

Control Strategy for Modular Multilevel Converters," *IEEE J. Emerg. Sel. Top. Power Electron.*, vol. 7, no. 2, pp. 1002–1014, 2019.

[139] C. Qi, X. Chen, L. Su, and Z. Lang, "Two-voltage hierarchical model predictive control for a single-phase cascaded H-bridge rectifier," *IET Power Electron.*, vol. 12, no. 7, pp. 1634–1642, 2019.

[140] X. Liu, D. Wang, and Z. Peng, "Cascade-Free Fuzzy Finite-Control-Set Model Predictive Control for Nested Neutral Point-Clamped Converters With Low Switching Frequency," *IEEE Trans. Control Syst. Technol.*, vol. 27, no. 5, pp. 2237–2244, 2019.

[141] S. Kayalvizhi and D. M. Vinod Kumar, "Load frequency control of an isolated micro grid using fuzzy adaptive model predictive control," *IEEE Access*, vol. 5, pp. 16241–16251, 2017.

[142] R. P. Aguilera and D. E. Quevedo, "Predictive control of power converters: Designs with guaranteed performance," *IEEE Trans. Ind. Informatics*, vol. 11, no. 1, pp. 53–63, 2015.

[143] Z. Zhang, A. Chen, X. Xing, and C. Zhang, "A novel model predictive control algorithm to suppress the zero-sequence circulating currents for parallel three-phase voltage source inverters," in *Conference Proceedings - IEEE Applied Power Electronics Conference and Exposition - APEC*, vol. 2016-May, pp. 3465–3470, 2016.

[144] T. T. Nguyen, H. J. Yoo, and H. M. Kim, "Model Predictive Control of Inverters in Microgrid with Constant Switching Frequency for Circulating Current Suppression," in *IEEE Region 10 Annual International Conference, Proceedings/TENCON*, vol. 2018-October, pp. 1566–1571, 2019.